A&A 612, A1 (2018)
https://doi.org/10.1051/0004-6361/201732098

Astronomy & Astrophysics

H.E.S.S. phase-I observations of the plane of the Milky Way

Special issue

The H.E.S.S. Galactic plane survey⋆

H.E.S.S. Collaboration: H. Abdalla[1], A. Abramowski[2], F. Aharonian[3,4,5], F. Ait Benkhali[3], E. O. Angüner[21], M. Arakawa[42], M. Arrieta[15], P. Aubert[24], M. Backes[8], A. Balzer[9], M. Barnard[1], Y. Becherini[10], J. Becker Tjus[11], D. Berge[12], S. Bernhard[13], K. Bernlöhr[3], R. Blackwell[14], M. Böttcher[1], C. Boisson[15], J. Bolmont[16], S. Bonnefoy[37], P. Bordas[3], J. Bregeon[17], F. Brun[26,⋆⋆], P. Brun[18], M. Bryan[9], M. Büchele[36], T. Bulik[19], M. Capasso[29], S. Carrigan[3,46], S. Caroff[30], A. Carosi[24], S. Casanova[21,3], M. Cerruti[16], N. Chakraborty[3], R. C. G. Chaves[17,22,⋆⋆], A. Chen[23], J. Chevalier[24], S. Colafrancesco[23], B. Condon[26], J. Conrad[27,28], I. D. Davids[8], J. Decock[18], C. Deil[3,⋆⋆], J. Devin[17], P. deWilt[14], L. Dirson[2], A. Djannati-Ataï[31], W. Domainko[3], A. Donath[3,⋆⋆], L. O'C. Drury[4], K. Dutson[33], J. Dyks[34], T. Edwards[3], K. Egberts[35], P. Eger[3], G. Emery[16], J.-P. Ernenwein[20], S. Eschbach[36], C. Farnier[27,10], S. Fegan[30], M. V. Fernandes[2], A. Fiasson[24], G. Fontaine[30], A. Förster[3], S. Funk[36], M. Füßling[37], S. Gabici[31], Y. A. Gallant[17], T. Garrigoux[1], H. Gast[3,47], F. Gaté[24], G. Giavitto[37], B. Giebels[30], D. Glawion[25], J. F. Glicenstein[18], D. Gottschall[29], M.-H. Grondin[26], J. Hahn[3], M. Haupt[37], J. Hawkes[14], G. Heinzelmann[2], G. Henri[32], G. Hermann[3], J. A. Hinton[3], W. Hofmann[3], C. Hoischen[35], T. L. Holch[7], M. Holler[13], D. Horns[2], A. Ivascenko[1], H. Iwasaki[42], A. Jacholkowska[16], M. Jamrozy[38], D. Jankowsky[36], F. Jankowsky[25], M. Jingo[23], L. Jouvin[31], I. Jung-Richardt[36], M. A. Kastendieck[2], K. Katarzyński[39], M. Katsuragawa[43], U. Katz[36], D. Kerszberg[16], D. Khangulyan[42], B. Khélifi[31], J. King[3], S. Klepser[37], D. Klochkov[29], W. Kluźniak[34], Nu. Komin[23], K. Kosack[18], S. Krakau[11], M. Kraus[36], P. P. Krüger[1], H. Laffon[26], G. Lamanna[24], J. Lau[14], J.-P. Lees[24], J. Lefaucheur[15], A. Lemière[31], M. Lemoine-Goumard[26], J.-P. Lenain[16], E. Leser[35], T. Lohse[7], M. Lorentz[18], R. Liu[3], R. López-Coto[3], I. Lypova[37], V. Marandon[3,⋆⋆], D. Malyshev[29], A. Marcowith[17], C. Mariaud[30], R. Marx[3], G. Maurin[24], N. Maxted[14,44], M. Mayer[7], P.J. Meintjes[40], M. Meyer[27], A. M. W. Mitchell[3], R. Moderski[34], M. Mohamed[25], L. Mohrmann[36], K. Morå[27], E. Moulin[18], T. Murach[37], S. Nakashima[43], M. de Naurois[30], H. Ndiyavala[1], F. Niederwanger[13], J. Niemiec[21], L. Oakes[7], P. O'Brien[33], H. Odaka[43], S. Ohm[37], M. Ostrowski[38], I. Oya[37], M. Padovani[17], M. Panter[3], R. D. Parsons[3], M. Paz Arribas[7], N. W. Pekeur[1], G. Pelletier[32], C. Perennes[16], P.-O. Petrucci[32], B. Peyaud[18], Q. Piel[24], S. Pita[31], V. Poireau[24], H. Poon[3], D. Prokhorov[10], H. Prokoph[12], G. Pühlhofer[29], M. Punch[31,10], A. Quirrenbach[25], S. Raab[36], R. Rauth[13], A. Reimer[13], O. Reimer[13], M. Renaud[17], R. de los Reyes[3], F. Rieger[3,41], L. Rinchiuso[18], C. Romoli[4], G. Rowell[14], B. Rudak[34], C. B. Rulten[15], S. Safi-Harb[48], V. Sahakian[6,5], S. Saito[42], D. A. Sanchez[24], A. Santangelo[29], M. Sasaki[36], M. Schandri[36], R. Schlickeiser[11], F. Schüssler[18], A. Schulz[37], U. Schwanke[7], S. Schwemmer[25], M. Seglar-Arroyo[18], M. Settimo[16], A. S. Seyffert[1], N. Shafi[23], I. Shilon[36], K. Shiningayamwe[8], R. Simoni[9], H. Sol[15], F. Spanier[1], M. Spir-Jacob[31], Ł. Stawarz[38], R. Steenkamp[8], C. Stegmann[35,37], C. Steppa[35], I. Sushch[1], T. Takahashi[43], J.-P. Tavernet[16], T. Tavernier[31], A. M. Taylor[37], R. Terrier[31], L. Tibaldo[3], D. Tiziani[36], M. Tluczykont[2], C. Trichard[20], M. Tsirou[17], N. Tsuji[42], R. Tuffs[3], Y. Uchiyama[42], D. J. van der Walt[1], C. van Eldik[36], C. van Rensburg[1], B. van Soelen[40], G. Vasileiadis[17], J. Veh[36], C. Venter[1], A. Viana[3,45], P. Vincent[16], J. Vink[9], F. Voisin[14], H. J. Völk[3], T. Vuillaume[24], Z. Wadiasingh[1], S. J. Wagner[25], P. Wagner[7], R. M. Wagner[27], R. White[3], A. Wierzcholska[21], P. Willmann[36], A. Wörnlein[36], D. Wouters[18], R. Yang[3], D. Zaborov[30], M. Zacharias[1], R. Zanin[3], A. A. Zdziarski[34], A. Zech[15], F. Zefi[30], A. Ziegler[36], J. Zorn[3], and N. Żywucka[38]

(Affiliations can be found after the references)

Received 13 October 2017 / Accepted 15 January 2018

ABSTRACT

We present the results of the most comprehensive survey of the Galactic plane in very high-energy (VHE) γ-rays, including a public release of Galactic sky maps, a catalog of VHE sources, and the discovery of 16 new sources of VHE γ-rays. The High Energy Spectroscopic System (H.E.S.S.) Galactic plane survey (HGPS) was a decade-long observation program carried out by the H.E.S.S. I array of Cherenkov telescopes in Namibia from 2004 to 2013. The observations amount to nearly 2700 h of quality-selected data, covering the Galactic plane at longitudes from $\ell = 250°$ to 65° and latitudes $|b| \leqslant 3°$. In addition to the unprecedented spatial coverage, the HGPS also features a relatively high angular resolution ($0.08° \approx 5$ arcmin mean point spread function 68% containment radius), sensitivity ($\lesssim$1.5% Crab flux for point-like sources), and energy range (0.2–100 TeV). We constructed a catalog of VHE γ-ray sources from the HGPS data set with a systematic procedure for both source detection and characterization of morphology and spectrum. We present this likelihood-based method in detail, including the introduction of a model component to account for unresolved, large-scale emission along the Galactic plane. In total, the resulting HGPS catalog contains 78 VHE sources, of which 14 are not reanalyzed here, for example, due to their complex morphology, namely shell-like sources and the Galactic center region. Where possible, we provide a firm identification of the VHE source or plausible associations with sources in other astronomical catalogs. We also studied the characteristics of the VHE sources with source parameter distributions. 16 new sources were previously unknown or unpublished, and we individually discuss their identifications or possible associations. We firmly identified 31 sources as pulsar wind nebulae (PWNe), supernova remnants (SNRs), composite SNRs, or gamma-ray binaries. Among the 47 sources not yet identified, most of them (36) have possible associations with cataloged objects, notably PWNe and energetic pulsars that could power VHE PWNe.

Key words. gamma rays: general – surveys – Galaxy: general

⋆ The source catalog is available at the CDS via anonymous ftp to cdsarc.u-strasbg.fr (130.79.128.5) or via http://cdsarc.u-strasbg.fr/viz-bin/qcat?J/A+A/612/A1

⋆⋆ Corresponding authors: H.E.S.S. Collaboration, e-mail: contact.hess@hess-experiment.eu

1. Introduction

In this paper, we present the results from the High Energy Spectroscopic System (H.E.S.S.) Galactic plane survey (HGPS), the deepest and most comprehensive survey of the inner Milky Way Galaxy undertaken so far in very high-energy (VHE; $0.1 \lesssim E \lesssim 100$ TeV) γ-rays. Results include numerous sky images (maps) and a new source catalog that is the successor of two previous HGPS releases. The first release (Aharonian et al. 2005a) was based on ∼140 h of observations with the imaging atmospheric Cherenkov telescope (IACT) array H.E.S.S. and contained eight previously unknown sources of VHE γ-rays. In the second release (Aharonian et al. 2006a), we used 230 h of data, covering $\ell = 330°$ to 30° in Galactic longitude and $|b| \leq 3°$ in latitude. In total, we detected 22 sources of γ-rays in that data set. Since then, the HGPS data set enlarged by more than one order of magnitude in observation time, now comprising roughly 2700 h of high-quality data recorded in the years 2004–2013. The spatial coverage is also significantly larger, now encompassing the region from $\ell = 250°$ to 65° in longitude. H.E.S.S. provided periodic updates on this progress by publishing new unidentified sources (Aharonian et al. 2008a) and through conference proceedings (Chaves et al. 2008a; Hoppe 2008b; Chaves 2009; Gast et al. 2011; Deil 2012; Carrigan et al. 2013a,b).

Compared to the first HGPS releases over a decade ago, the deeper exposure over a much larger sky area of the Galaxy, combined with improved γ-ray reconstruction, analysis, and modeling techniques, now results in a new catalog containing 78 VHE γ-ray sources. Figure 1 illustrates the HGPS region and compares this region to the structure of the Galaxy, represented by an all-sky *Planck* CO(1-0) map, and the smaller regions of previous surveys performed by the IACT arrays High-Energy-Gamma-Ray Astronomy (HEGRA; Aharonian et al. 2002) and Very Energetic Radiation Imaging Telescope Array System (VERITAS; Weinstein 2009). Even though the HGPS covers only a few percent of the entire sky, this region contains the vast majority of the known Galactic *Fermi*-LAT 2FHL γ-ray sources (Ackermann et al. 2016)[1]. The figure also shows the measured integral VHE γ-ray flux and the HGPS observation times. As can be seen from the map of observation times (Fig. 1, lower panel), the HGPS data set is not homogeneous. Nonetheless, the HGPS features on average a point-source sensitivity better than 1.5% Crab[2] in the core survey region within 60° in longitude of the Galactic center (see Fig. 4, lower panel).

In this paper, we aim to present the entire data set of the HGPS in a way that is accessible and useful for the whole astronomical community. We have made the maps of VHE γ-ray significance, flux, upper limits, and sensitivity available online[3] for the first time in FITS format (Pence et al. 2010). We developed a semi-automatic analysis pipeline to construct a catalog by detecting and modeling discrete sources of VHE γ-ray emission present in these survey maps. We applied a standardized methodology to the characterization of the γ-ray sources to measure their morphological and spectral properties. The goal was to perform a robust analysis of sources in the survey region with as little manual intervention as possible. With such a generic approach, the catalog pipeline is not optimal for the few very bright and extended sources with complex (non-Gaussian) morphology. For these sources, dedicated analyses are more appropriate, and in all cases, they have already been performed and published elsewhere. We therefore exclude these sources, which are listed in Table 1 below, from the pipeline analysis but include the results from the dedicated analysis in the HGPS catalog for completeness.

We have structured the present paper as follows: we describe the H.E.S.S. telescope array, the data set, and the analysis techniques in Sect. 2. We provide the maps of the VHE γ-ray sky in various representations and details of their production in Sect. 3. Section 4 explains how the HGPS catalog of γ-ray sources was constructed, then Sect. 5 presents and discusses the results, including source associations and identifications with other astronomical objects. Section 6 concludes the main paper with a summary of the HGPS and its results. In Appendix A, we describe the supplementary material (maps and catalog available at the CDS), including caveats concerning measurements derived from the maps and catalog.

2. Data set

2.1. The High Energy Stereoscopic System (H.E.S.S.)

H.E.S.S. is an array of five IACTs located at an altitude of 1800 m above sea level in the Khomas highland of Namibia. It detects Cherenkov light emitted by charged particles in an electromagnetic extensive air shower (EAS) initiated when a primary photon (γ-ray) of sufficient energy enters Earth's atmosphere. This array consists of four smaller telescopes, built and operated in the first phase of the experiment (H.E.S.S. Phase I) and a fifth much larger telescope, which was added to the center of the array in 2012 to launch the second phase (H.E.S.S. Phase II) of the experiment.

H.E.S.S. accumulated the data presented here exclusively with the H.E.S.S. array during its first phase. These four H.E.S.S. Phase I telescopes have tessellated mirrors with a total area of 107 m^2 and cameras consisting of 960 photomultipliers. The energy threshold of the four-telescope array is roughly 200 GeV at zenith and increases with increasing zenith angle. We can reconstruct the arrival direction and energy of the primary photon with accuracies of ∼0.08° and ∼15%, respectively. Because of its comparatively large field of view (FoV), 5° in diameter, the H.E.S.S. Phase I array is well suited for survey operations. The relative acceptance for γ-rays is roughly uniform for the innermost 2° of the FoV and gradually drops toward the edges to 40% of the peak value at 4° diameter (Aharonian et al. 2006b).

2.2. Observations, quality selection, and survey region

The HGPS data set covers the period from January 2004 to January 2013. H.E.S.S. acquired this data set by pointing the IACT array to a given position in the sky for a nominal duration of 28 min (referred to as an observation run hereafter). We considered all runs with zenith angles up to 65° and observation positions centered in the Galactic coordinate range $\ell = 244.5°$ to 77.5° and $|b| < 7.0°$. To reduce systematic effects arising from imperfect instrument or atmospheric conditions, we carefully selected good-quality runs as close as possible to the nominal description of the instrument used in the Monte Carlo (MC) simulations (see Aharonian et al. 2006b). For example, the IACT

[1] In this paper, we compare the HGPS with the *Fermi*-LAT 2FHL catalog, but not with 3FHL (The Fermi-LAT Collaboration 2017) or the HAWC 2HWC catalog (Abeysekara et al. 2017), which were not published at the time this paper was written and which already contain comparisons with Galactic H.E.S.S. sources.

[2] Throughout this paper, and as is generally the case in VHE γ-ray astronomy, we use the Crab Nebula flux as a standard candle reference: 1 Crab unit is defined here as $\Phi(>1\,\mathrm{TeV}) = 2.26 \times 10^{-11}$ cm^{-2} s^{-1} (Aharonian et al. 2006b).

[3] https://www.mpi-hd.mpg.de/hfm/HESS/hgps

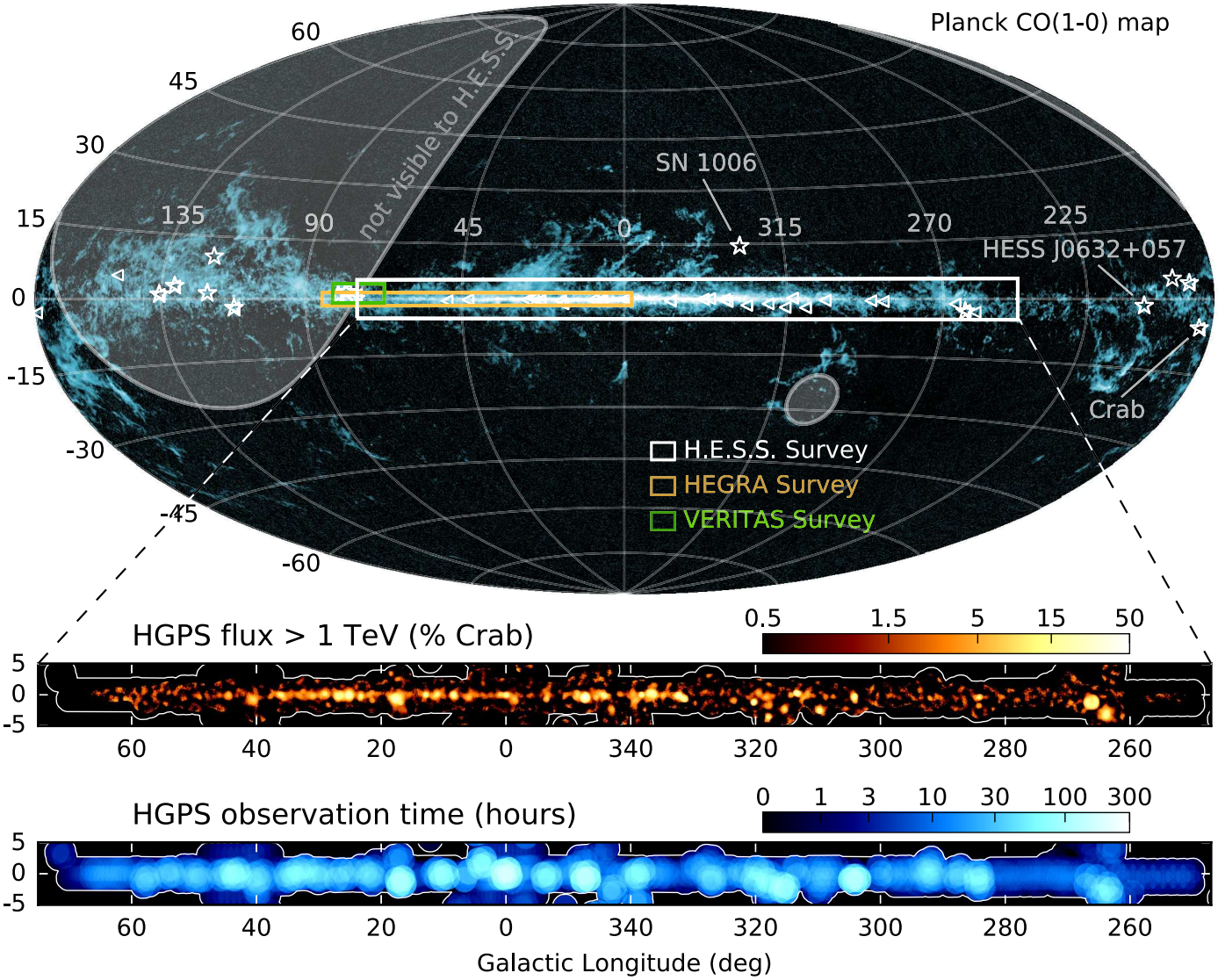

Fig. 1. Illustration of HGPS region superimposed an all-sky image of *Planck* CO(1-0) data (Planck Collaboration X 2016) in Galactic coordinates and Hammer-Aitoff projection. For comparison, we overlay the HEGRA Galactic plane survey (Aharonian et al. 2002) and VERITAS Cygnus survey (Weinstein 2009) footprints. Triangles denote the *Fermi*-LAT 2FHL γ-ray sources (Ackermann et al. 2016) identified as Galactic, and stars indicate the 15 Galactic VHE γ-ray sources outside the HGPS region. H.E.S.S. has detected three of these, which are labeled SN 1006 (Acero et al. 2010a), the Crab Nebula (Aharonian et al. 2006b; H.E.S.S. Collaboration 2014a), and HESS J0632+057 (Aharonian et al. 2007; Aliu et al. 2014a). The gray shaded regions denote the part of the sky that cannot be observed from the H.E.S.S. site at reasonable zenith angles (less than 60°). The lower panels show the HGPS γ-ray flux above 1 TeV for regions where the sensitivity is better than 10% Crab (correlation radius $R_c = 0.4°$; see Sect. 3) and observation time, both also in Galactic coordinates. The white contours in the lower panels delineate the boundaries of the survey region; the HGPS has little or no exposure beyond Galactic latitudes of $|b| \leq 3°$ at most locations along the Galactic plane.

cameras suffer from occasional hardware problems affecting individual or groups of camera pixels, so we did not use observation runs with significant pixel problems. In addition, we only used those runs with at least three operational telescopes.

Furthermore, despite the very good weather conditions at the H.E.S.S. site, both nightly and seasonal variations of the atmospheric transparency occur and require monitoring. Layers of dust or haze in the atmosphere effectively act as a filter of the Cherenkov light created in an EAS, thereby raising the energy threshold for triggering the IACTs. Since we calculated the instrument response tables describing the performance of the instrument (e.g., the effective areas) with MC simulations, deviations from the atmospheric conditions assumed in the simulations lead to systematic uncertainties in the determination of energy thresholds, reconstructed energies, and γ-ray fluxes. To account for this, we applied a further quality cut using only observations where the Cherenkov transparency coefficient T (Hahn et al. 2014), which characterizes the atmospheric conditions, falls within the range $0.8 < T < 1.2$ (for clear skies, $T = 1$).

After applying the aforementioned data quality selection cuts, 6239 observation runs remain, ~77% of which are runs with four telescopes operational. The total observation time is 2864 h, corresponding to a total livetime of 2673 h (6.7% average dead time). The third panel of Fig. 1 is a map of the observation time over the survey region, clearly showing a non-uniform exposure. This is a result of the HGPS observation strategy, summarized as follows:

– Dedicated survey observations, taken with a typical spacing between pointings of 0.7° in longitude and in different latitude bands located between $b = -1.8°$ and $b = 1°$.

In addition, for the longitude bands $\ell = 355°$ to $5°$ and $\ell = 38°$ to $48°$, we extended the survey observations in latitude, adding observation pointings from $b = -3.5°$ to $3.5°$ to explore the possibility of high-latitude emission.
– Deeper follow-up observations of source candidates ("hot spots") seen in previous survey observations.
– Exploratory and follow-up observations of astrophysical objects located inside the survey region that were promising candidates for emitting VHE γ-rays.
– Observations to extend the HGPS spatial coverage and fill-up observations to achieve a more uniform sensitivity across the Galactic plane.

Combining all of these observations, we achieved a more uniform, minimum 2% Crab flux sensitivity in the region between $\ell = 283°$ to $58°$ and $b = -0.3° \pm 0.7°$ (see the sensitivity map in Fig. 4).

2.3. Event reconstruction and selection

We first converted the camera pixel data to amplitudes measured in units of photoelectrons (p.e.), identifying the non-operational pixels for a given observation following the procedures described by Aharonian et al. (2004a). We then applied standard H.E.S.S. techniques for the analysis of the camera images: image cleaning, Hillas moment analysis, and the stereo reconstruction of the direction of the primary photon, described by Aharonian et al. (2006b). To suppress the hadronic background and select photon candidate events, we used a multivariate machine learning technique using boosted decision trees based on EAS and image shape parameters (Ohm et al. 2009). For the generation of the survey maps (Sect. 3), we applied the hard cuts configuration whereas for the extraction of source spectra (Sect. 5) we used the standard cuts. The most important distinguishing cut is a minimum of 160 p.e. for hard cuts and 60 p.e. for standard cuts. But there are other differences; the cuts used here are given as the ζ analysis cuts in Table 2(a) in Ohm et al. (2009).

We cross-checked the results presented in this paper with an alternative calibration, reconstruction, and gamma-hadron separation method based on a semi-analytical description of the EAS development (de Naurois & Rolland 2009) with hard cuts of 120 p.e. for maps and standard cuts of 60 p.e. for spectra.

For the energy reconstruction of the primary photons, we compared the image amplitudes in the cameras to the mean amplitudes found in MC simulations of the array (Bernlöhr 2008). Those simulations, which were analyzed with the same chain as the real data for the sake of consistency, include the detailed optical and electronic response of the instrument. The range of optical efficiencies encountered in the HGPS data set is large; efficiencies start at 100% of the nominal value and drop to almost 50% for some telescopes prior to the mirror refurbishments conducted in 2009–2011. Therefore, we produced several sets of MC simulations, each with optical efficiencies of the four telescopes corresponding to their states at suitably chosen times: at the start of H.E.S.S. operations; at the point when efficiencies had dropped to ~70%, before the first mirror refurbishment campaign; and after the mirror refurbishment of each telescope. We then chose the set of simulations most closely matching the state of the system at a given time. Finally, we corrected the remaining difference between simulated and actual optical efficiencies using a calibration technique based on the intensity of ring-shaped images from individual muons producing Cherenkov radiation above a telescope (Bolz 2004; Leroy 2004).

3. HGPS sky maps

In this section, we describe the methods used to produce the HGPS sky maps. We used the sky maps as the basis for subsequent construction of the HGPS source catalog; this catalog is also a data product that we release to the community along with this work.

We first computed sky maps for each individual observation run. We then summed these maps over all observations. We chose to use a Cartesian projection in Galactic coordinates, covering the region from $\ell = 70°$ to $250°$ and $b = \pm 5°$, and we set the pixel size to $0.02°$ pixel^{-1}.

In Sect. 3.1, we describe the production of the map containing the detected events (events map). In Sect. 3.2, we describe the map of expected background events (acceptance map, Sect. 3.2.1), the estimation of a refined background map by introducing exclusion regions (Sect. 3.2.2), and the usage of the adaptive ring background method (Sect. 3.2.3). We then continue in Sect. 3.3 by describing the computation of the significance map, and, in Sect. 3.4, the exposure map (Sect. 3.4.1), which is used to derive quantities such as flux (Sect. 3.4.2), flux error and upper limits (Sect. 3.4.3), and sensitivities (Sect. 3.4.4).

3.1. Events map

The events map consists of the reconstructed positions of the primary γ-ray photons from all events in the sky. To avoid systematic effects near the edge of the FoV in each observation run, we only include events for which the direction of the primary photon is reconstructed within $2°$ of the center of the FoV. This choice results in an effective analysis FoV of $4°$ diameter.

At the lowest energies, the energy reconstruction is biased by EASs with upward fluctuations in the amount of detected Cherenkov light; downward fluctuations do not trigger the cameras. In order to derive reliable flux maps (see Sect. 3.4.2), we only kept events with an energy reconstructed above a defined safe energy threshold. We chose the level of this safe threshold such that, for each run, the energy bias as determined by MC simulations is below 10% across the entire FoV. This conservative approach (together with the use of hard analysis cuts defined in Sect. 2.3) leads to energy threshold values ranging from ~400 GeV, where the array observed close to zenith, up to 2 TeV at $65°$ from zenith. Figure 2 plots the variation of the safe energy threshold with Galactic longitude, showing the energy threshold for each observation together with the minimum value for each longitude. The variations observed are mainly due to the zenith angle dependency, and regions of different Galactic longitude generally are observable at different zenith angles.

3.2. Background estimation

Events passing the event reconstruction and selection procedure are considered γ-ray candidate events. Since these events are still dominantly from EASs induced by γ-ray-like cosmic rays and electrons or positrons, we estimated the amount of remaining background events on a statistical basis using a ring model (Berge et al. 2007) as detailed further below. For each test position, we counted the photon candidates found in a suitable ring-shaped region around that position in the same FoV. This yields an estimate of the background level after proper normalization and after excluding regions with actual γ-ray emission from the background estimate.

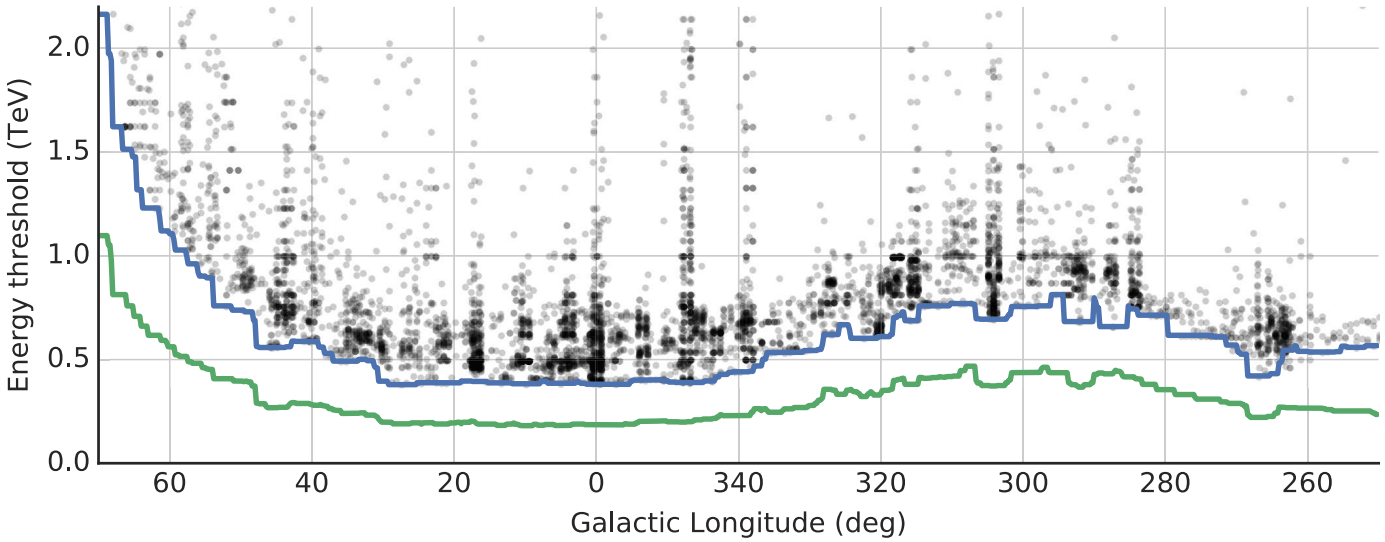

Fig. 2. HGPS minimum safe energy threshold as a function of Galactic longitude for a latitude of $b = 0°$. The blue curve shows the minimum threshold for hard cuts (used for maps), and the green curve indicates standard cuts (used for spectra). The black dots represent the safe threshold for each observation run obtained for the hard cuts configuration. The few black dots below the blue line correspond to runs at Galactic latitude $|b| > 2°$.

3.2.1. Acceptance map

The acceptance map represents the number of expected events from cosmic-ray backgrounds estimated from runs of sky regions at similar zenith angles but without VHE γ-ray sources. As for the events map (see Sect. 3.1), we computed the acceptance map for energies above the safe energy threshold. To account for the differences in optical efficiency and observation time between these runs and those under analysis, we normalized the acceptance map such that, outside the exclusion regions (see Sect. 3.2.2), the number of expected counts matches the number of measured counts. The acceptance maps are used to derive the normalization coefficient between the region of interest and the background region (see Sect. 3.3).

3.2.2. Exclusion regions

The background estimation method described above only works if regions with VHE γ-ray emission are excluded from the background estimation region. We defined exclusion regions automatically using an iterative algorithm to avoid potential observer bias and to treat the entire data set in a uniform way. The procedure starts with the significance maps (see Sect. 3.3) produced for the two standard correlation radii $R_c = 0.1°$ and $0.2°$. These radii define the circular region over which a quantity (e.g., γ-ray excess) is integrated. The procedure identifies regions above 5σ and expands them by excluding an additional $0.3°$ beyond the 5σ contour. This procedure is conservative; it minimizes the amount of surrounding signal that could potentially contaminate the background estimation. A first estimation of the exclusion regions is then included in the significance map production and a new set of exclusion regions is derived. We iterated this procedure until stable regions are obtained, which typically occurs after three iterations. The resulting regions are shown in Fig. A.6 below.

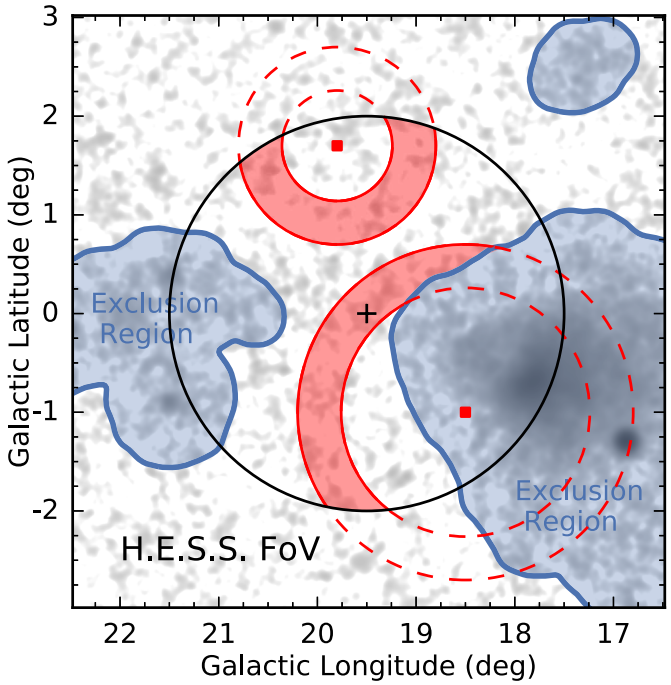

Fig. 3. Illustration of the adaptive ring method for background estimation for a single observation (see Sect. 3.2.3). The HGPS significance image is shown in inverse grayscale and exclusion regions as blue contours. The analysis FoV for one observation is shown as a black circle with $2°$ radius and a black cross at the observation pointing position. The red rings illustrate the regions in which the background is estimated for two positions in the FoV (illustrated as red squares). Only regions in the ring inside the FoV and outside exclusion regions are used for background estimation. For the position in the lower right, the ring was adaptively enlarged to ensure an adequate background estimate (see text).

3.2.3. Adaptive ring method

In the HGPS, often exclusion regions cover a significant fraction of the FoV; therefore, we could not use the standard ring background method (Berge et al. 2007). For example, using a typical outer ring radius of $\sim 0.8°$ would lead to numerous holes in the sky maps at positions where the entire ring would be contained inside an exclusion region (i.e., where no background estimation was possible). A much larger outer radius (e.g., $\sim 1.5°$) would be

necessary to prevent these holes but would lead to unnecessarily large uncertainties in the background estimation in regions without, or with small, exclusion regions where smaller ring radii are feasible.

To address the limitations of the standard method, we do not use a static ring geometry but rather adaptively change the inner and outer ring radii, as illustrated in Fig. 3, depending on the exclusion regions present in a given FoV. For a given test position within a FoV, we begin with a minimum inner ring radius of 0.7° and constant ring thickness 0.44° and enlarge the inner radius if a large portion of the ring area overlaps with exclusion regions. We do this until the acceptance integrated in the ring (but outside exclusion regions) is more than four times the acceptance integrated at the test position. A maximum outer radius of 1.7° avoids large uncertainties in the acceptance toward the edge of the FoV.

3.3. Significance maps

We produced significance maps to determine the exclusion regions (see Sect. 3.2.2). For each grid position (ℓ, b) in a significance map, we counted the number of photon candidates $N_{\rm ON}$ in the circular ON region, defined a priori by the correlation radius $R_{\rm c}$. We determined the background level by counting the number of photon candidates $N_{\rm OFF}$ in the ring centered at (ℓ, b). The background normalization factor is $\alpha \equiv \xi_{\rm ON}/\xi_{\rm OFF}$, where $\xi_{\rm ON}$ is the integral of the acceptance map within $R_{\rm c}$ and $\xi_{\rm OFF}$ is the integral of the acceptance map within the ring. The number of excess events N_γ within $R_{\rm c}$ is then

$$N_\gamma = N_{\rm ON} - \alpha N_{\rm OFF}. \tag{1}$$

We computed the significance of this γ-ray excess according to Eq. (17) of Li & Ma (1983) without correcting further for trials.

3.4. High-level maps

We can derive additional high-level maps based on the measurement of N_γ within a given $R_{\rm c}$ and the instrument response functions. In this work, we computed flux, flux error, sensitivity, and upper limit maps, starting from the formula

$$F = \frac{N_\gamma}{N_{\rm exp}} \int_{E_1}^{E_2} \phi_{\rm ref}(E)\,{\rm d}E, \tag{2}$$

where F is the integral flux computed between the energies E_1 and E_2, N_γ is the measured excess, and $N_{\rm exp}$ is the total predicted number of excess events, also called exposure (see Sect. 3.4.1).

3.4.1. Exposure maps

The exposure $N_{\rm exp}$ in Eq. (2) is given by

$$N_{\rm exp} \equiv \mathcal{E} = \sum_{\rm R\in runs} T_{\rm R} \int_{E_{\rm min}}^{\infty} \phi_{\rm ref}(E_{\rm r})\, A_{\rm eff}(E_{\rm r}, q_{\rm R})\,{\rm d}E_{\rm r}. \tag{3}$$

Here, $E_{\rm r}$ is the reconstructed energy, $T_{\rm R}$ is the observation livetime, $q_{\rm R}$ symbolizes the observation parameters for a specific run (zenith, off-axis, and azimuth angle; pattern of telescopes participating in the run; and optical efficiencies); $A_{\rm eff}$ is the effective area obtained from MC simulations, which is assumed constant during a 28 min run; and $E_{\rm min}$ is the safe threshold energy appropriate for the observation (as described in Sect. 3.1). We computed the quantity $N_{\rm exp}$ for each position in the sky to create the expected γ-ray count map, also referred to as the exposure map $\mathcal{E}$ in the following. The function $\phi_{\rm ref}(E)$ is the reference differential photon number γ-ray source flux, assumed to be following a power law (PL) with a predefined spectral index, i.e.,

$$\phi_{\rm ref}(E) = \phi_0\,(E/E_0)^{-\Gamma}. \tag{4}$$

3.4.2. Flux maps

In Eq. (2), the flux value F is completely determined by the scaling factor $N_\gamma/N_{\rm exp}$ once the spectral shape is fixed. We chose to use $E_1 = 1$ TeV and $E_2 = \infty$. We stress that E_1 is not the threshold energy used in the analysis, but the energy above which the integral flux is given. In Eq. (4), one can choose the flux normalization ϕ_0 arbitrarily, since it cancels out in the computation of the flux. We also chose the spectral index $\Gamma = 2.3$ in the released maps to be compatible with the average index of known Galactic VHE γ-ray sources. To test the impact of this latter assumption, we performed tests that show that, on average, flux variations are less than 5% if the assumed spectral index is varied by ±0.2 (our systematic uncertainty of the spectral index).

The released flux maps contain values of integral flux above 1 TeV, calculated according to Eq. (2), in units of cm^{-2} s^{-1}. This should be interpreted as the flux of a potential source, assuming a spectrum $\phi_{\rm ref}(E)$, that is centered on a given pixel position in the map and fully enclosed within $R_{\rm c}$.

Figures 1 and A.1 show two example flux maps computed with $R_{\rm c} = 0.4°$ and 0.1°, respectively. The maps contain nonzero values only in regions in which the sensitivity is better than 2.5% Crab to prevent very large (positive and negative) values due to statistical fluctuations in low-exposure regions.

3.4.3. Flux error and upper limit maps

Statistical uncertainties on the flux were computed by replacing N_γ in Eq. (2) by $N_\gamma^{\pm 1\sigma}$, which are the upper and lower boundaries of the measured excess for a 68% confidence level. Those errors were computed with a Poisson likelihood method described in Rolke et al. (2005), using the same $N_{\rm ON}$ and $N_{\rm OFF}$ integrated within the circle of radius $R_{\rm c}$ used when computing the excess maps. The values reported in the flux-error maps are the average of the upper and lower error bars.

Similarly, an upper-limit map can be calculated by replacing N_γ in Eq. (2) by $N_\gamma^{\rm UL}$, that is, the upper limit on the excess found for a predefined confidence level of 95%; we used the same profile likelihood method as for the error bar.

3.4.4. Sensitivity maps

The sensitivity is defined as the minimal flux needed for a source with the assumed spectrum and fully contained within the correlation circle $R_{\rm c}$ to be detected above the background at 5σ statistical significance. Alternatively this can be thought of as a measure of $\hat{N}_\gamma$, the number of photons needed to reach such a significance level above the background determined by $N_{\rm OFF}$ and α. To compute the sensitivity map, N_γ in Eq. (2) is replaced by $\hat{N}_\gamma$, which is determined by numerically solving Eq. (17) of Li & Ma (1983) for $N_{\rm ON}$ (related to $\hat{N}_\gamma$ by Eq. (1) above). We note that possible background systematics are not taken into account in this computation.

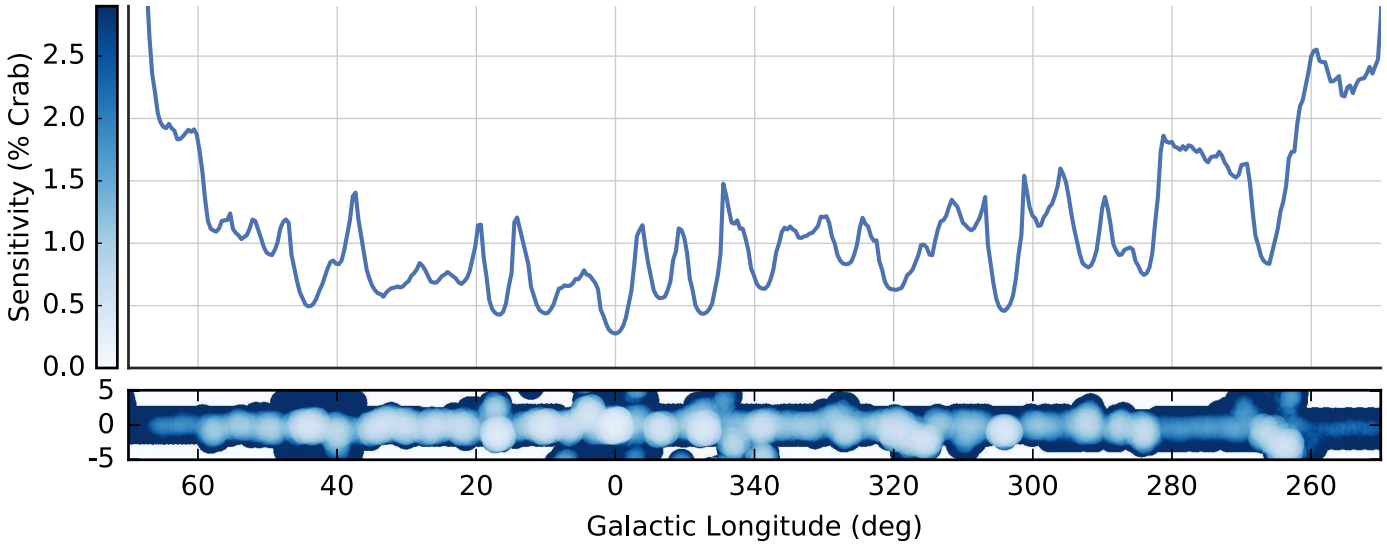

Fig. 4. HGPS point-source sensitivity map and profile along the Galactic plane at a Galactic latitude $b = 0°$. The sensitivity is given in % Crab, for a correlation radius $R_c = 0.1°$, assuming a spectral index $\Gamma = 2.3$. This sensitivity is computed under the isolated point source assumption and is thus better than the actual sensitivity achieved for the HGPS source catalog (see Sect. 4.12).

The point-source sensitivity level reached by H.E.S.S. at all points in the HGPS data set is depicted in Fig. 4, where a projection of the sensitivity map along Galactic longitude at a Galactic latitude of $b = 0°$ is also shown. It is typically at the level of 1 to 2% Crab. The deepest observations were obtained around interesting objects for which additional pointed observations were performed. Examples include the Galactic center region (around $\ell = 0°$, where the best sensitivity of ∼0.3% Crab is reached), the Vela region ($\ell = 266°$), the regions around HESS J1825−137 and LS 5039 ($\ell = 17°$), or around HESS J1303−631 and PSR B1259−63 ($\ell = 304°$).

Similarly, the sensitivity values along Galactic latitude for two values of longitude are shown in Fig. 11. For most of the surveyed region, the sensitivity decreases rapidly above $|b| > 2°$ due to the finite FoV of the H.E.S.S. array and the observation pattern taken, except for a few regions, such as at $\ell = 0°$ where high latitude observations were performed (see Sect. 2). The best sensitivity is obtained around $b = -0.3°$, reflecting the H.E.S.S. observation strategy; the latitude distribution of the sources peaks in this region.

We note that the sensitivity shown in Fig. 4 does not correspond to the completeness of the HGPS source catalog. One major effect is that the HGPS sensitivity is dependent on source size; it is less sensitive for larger sources, as shown in Fig. 13 and discussed at the end of Sect. 5.3. Other effects that reduce the effective sensitivity or completeness limit of HGPS are the detection threshold, which corresponds to $\sim 5.5\sigma$; the large-scale emission model; and source confusion, as discussed in the following Sect. 4.

4. HGPS source catalog

4.1. Introduction and overview

The HGPS source catalog construction procedure intends to improve upon previous H.E.S.S. survey publications both in sensitivity and homogeneity of the analysis performed. The previous iteration, the second H.E.S.S. survey paper of 2006 (Aharonian et al. 2006a), used a 230 h data set with inhomogeneous exposure that was limited to the innermost region of the Galaxy. This survey detected a total of 14 sources by locating peaks in significance maps on three different spatial scales: 0.1°, 0.22°, and 0.4°. It then modeled the sources by fitting two-dimensional symmetric Gaussian morphological models to determine the position, size and flux of each source, using a Poissonian maximum-likelihood method.

Since 2006, H.E.S.S. has increased its exposure tenfold and enlarged the survey region more than twofold, while also improving the homogeneity of the exposure. As illustrated in the upper panel of Fig. 5, the data now show many regions of complex emission, for example, overlapping emission of varying sizes and multiple sources with clearly non-Gaussian morphologies. Apart from discrete emission, the Galactic plane also exhibits significant emission on large spatial scales (Abramowski et al. 2014a). For these reasons, we needed to develop a more complex analysis procedure to construct a more realistic model of the γ-ray emission in the entire survey region. Based on this model, we compiled the HGPS source catalog.

We first introduce the maximum-likelihood method used for fitting the emission properties (Sect. 4.2). Next, we describe the H.E.S.S. point spread function (PSF; Sect. 4.3) and the TS maps (Sect. 4.4), which are two important elements in the analysis and catalog construction. The procedure is then as follows:

1. Cut out the Galactic center (GC) region and shell-type supernova remnants from the data set because of their complex morphologies (Sect. 4.5).
2. Model the large-scale emission in the Galactic plane globally (Sect. 4.6).
3. Split the HGPS region into manageable regions of interest (ROIs) (Sect. 4.7).
4. Model the emission in each ROI as a superposition of components with Gaussian morphologies (Sect. 4.8).
5. Merge Gaussian components into astrophysical VHE γ-ray sources (Sect. 4.9).
6. Determine the total flux, position, and size of each γ-ray source (Sect. 4.10).

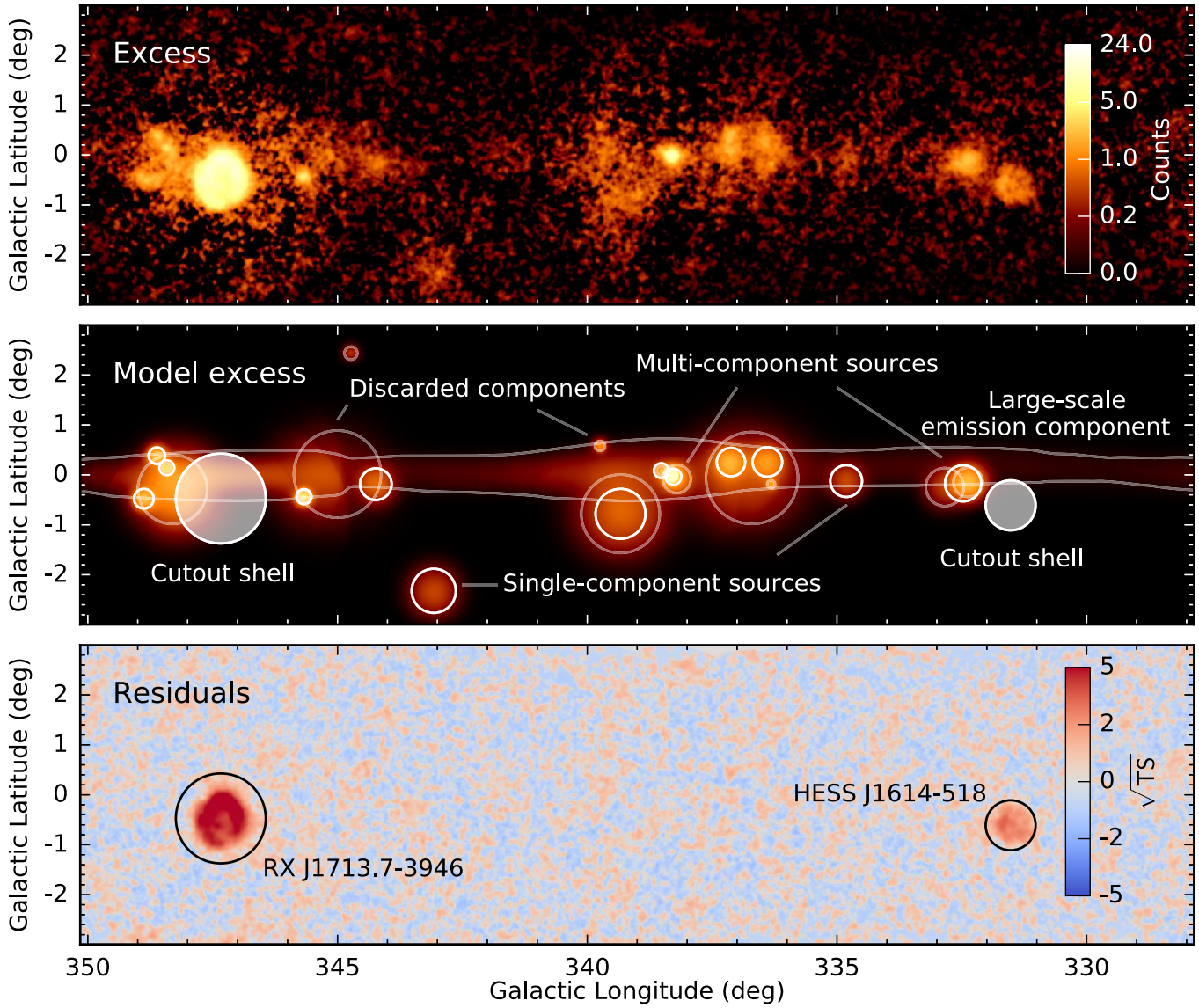

Fig. 5. Illustration of the catalog model construction in the region of 350° to 328° in Galactic longitude. The *upper panel* shows the γ-ray excess counts smoothed by the PSF, the *middle panel* the PSF-convolved and smoothed excess model, and the *lower panel* the significance map of the residuals for a point-like source hypothesis (given in sign(Flux) $\sqrt{\mathrm{TS}}$). The *middle panel* shows examples of the steps taken in the excess map modeling part of the source catalog procedure (see Sect. 4 for details). It starts by cutting out shell-type supernova remnants (SNRs; RX J1713.7−3946 and the SNR candidate HESS J1614−518 in this region) and by assuming a fixed large-scale emission component. Then a multi-Gaussian model was fitted with the significant components shown in the *middle panel* as thin transparent circles. Some of these were discarded and are not part of the emission attributed to HGPS catalog sources. White circles show examples of single-component as well as multicomponent sources. For a complete overview of all analysis regions (ROIs) and excluded sources, see Fig. A.6.

7. Measure the spectrum of each source (Sect. 4.11).
8. Associate the HGPS sources with previously published H.E.S.S. sources and multiwavelength (MWL) catalogs of possible counterparts (Sect. 5.1).

4.2. Poisson maximum-likelihood morphology fitting

To detect and characterize sources and to model the large-scale emission in the Galactic plane, we used a spatially-binned likelihood analysis based on the following generic model:

$$N_{\mathrm{Pred}} = N_{\mathrm{Bkg}} + \mathrm{PSF} * (\mathcal{E} \cdot S)\,, \tag{5}$$

where N_{Pred} represents the predicted number of counts, N_{Bkg} the background model created with the adaptive ring method (described in Sect. 3.2.3), $\mathcal{E}$ the exposure map (see Eq. (3) in Sect. 3.4.2), and S a two-dimensional parametric morphology model that we fit to the data. Additionally, we took into account the angular resolution of H.E.S.S. by convolving the flux model with a model of the PSF of the instrument.

Assuming Poisson statistics per bin, the maximum-likelihood fit then minimizes the *Cash* statistic (Cash 1979),

$$C = 2 \sum_i (M_i - D_i \log M_i)\,, \tag{6}$$

where the sum is taken over all bins i, and M_i (model) represents the expected number of counts according to Eq. (5) and D_i (data) the actual measured counts per bin.

To determine the statistical significance of a best-fit source model compared to the background-only model, we use a

likelihood ratio test with test statistic TS. This is defined by the likelihood ratio or equivalently as the difference in C between both hypotheses,

$$\mathrm{TS} = C_0 - C_S, \tag{7}$$

where C_0 corresponds to the value of the *Cash* statistic of the background-only hypothesis and C_S the best-fit model that includes the source emission.

For a large number of counts, according to Wilks' theorem (Wilks 1938), TS is asymptotically distributed as χ^2_N, where N is the number of free parameters defining the flux model. In this limit, the statistical significance corresponds approximately to $\mathrm{sign(Flux)} \cdot \sqrt{|\mathrm{TS}|}$, where the sign of the best-fit flux is needed to allow for negative significance values in regions where the number of counts is smaller than the background estimate (e.g., due to a statistical downward fluctuation).

We performed the modeling and fitting described above in Eqs. (5)–(7) in pixel coordinates using the HGPS maps in Cartesian projection. Spatial distortion of flux models are negligible as a result of the projection from the celestial sphere because the HGPS observations only cover a latitude range of $|b| \leqslant 3°$. We implemented the analysis in Python using Astropy version 1.3 (Astropy Collaboration et al. 2013), Sherpa version 4.8 (Freeman et al. 2001), and Gammapy version 0.6 (Donath et al. 2015; Deil et al. 2017).

4.3. Point spread function

For HGPS, the PSF was computed for a given sky position assuming a power-law point source with a spectral index of 2.3 (average index of known VHE γ-ray sources) and assuming rotational symmetry of the PSF. Since the H.E.S.S. PSF varies with γ-ray energy and observing parameters such as the number of participating telescopes, zenith angle, and offset angle in the field of view, an effective PSF corresponding to the HGPS survey counts maps was computed by applying the same cuts (especially safe energy threshold) and exposure weighting the PSF of contributing runs (i.e., within the FoV of 2°). The per-run PSF was computed by interpolating PSFs with similar observation parameters, using precomputed lookups from MC EAS simulations. All computations were carried out using two-dimensional histograms with axes θ^2, where θ is the offset between the MC source position and the reconstructed event position, and $\log(E_r)$, where E_r is the reconstructed event energy; at the very end, the integration over energy was performed, resulting in a one-dimensional histogram with axis θ^2, which was fitted by a triple-exponential analytical function to obtain a smooth distribution,

$$\frac{\mathrm{d}P}{\mathrm{d}\theta^2}(\theta^2) = \sum_{i=1}^{3} A_i \exp\left(-\frac{\theta^2}{2\sigma_i^2}\right), \tag{8}$$

where P is the event probability, and A_i and σ_i are the weights and widths of the corresponding components, respectively. This ad hoc model corresponds to a triple-Gaussian, two-dimensional, PSF model when projected onto a sky map.

For the HGPS catalog, the 68% containment radius of the PSF model adopted is typically $\theta \sim 0.08°$ and varies by approximately ±20% at the locations of the HGPS sources. For observations with large FoV offsets, the 68% containment increases by almost a factor of two to $\theta \sim 0.15°$, which is mostly relevant for high Galactic latitude sources at the edge of the HGPS survey region. The HGPS PSF has a 95% containment radius of $\theta \sim 0.2°$and approximately varies by ±20% at the locations of the HGPS sources. The PSF at large FoV offsets (corresponding to high-GLAT regions in the survey map) is more tail heavy; there the 95% to 68% containment radius ratio increases from ∼2.5 up to 4. Section 4.10.2 discusses systematic uncertainties related to the PSF model in connection with upper limits on source sizes.

4.4. Test statistics maps

In addition to the standard Li & Ma significance maps described in Sect. 3.3, we also used TS maps in the analysis. The TS denotes the likelihood ratio of the assumed source hypothesis vs. the null hypothesis (i.e., background only) for every position (pixel) in the map. We computed these maps assuming various spatial templates: a point-like source morphology (i.e., PSF only), and PSF-convolved Gaussian morphologies with widths 0.05°, 0.10°, and 0.20°. During the computation of each map, at the center of each map pixel, we performed a single-parameter likelihood fit of the amplitude of the template, according to Eq. (5). We then filled the map with the TS value defined in Eq. (7).

We used the resulting TS maps primarily to compute residual maps and residual distributions. The main advantage over standard Li & Ma significance maps is that source morphology and PSF information can be taken into account. Additionally, this paper uses TS maps when presenting sky maps because they contain uniform statistical noise everywhere in the map. In contrast, flux or excess maps that are smoothed with the same spatial templates still show increased noise in regions of low exposure. We implemented the TS map algorithm available in Gammapy; see also Stewart (2009) for a more detailed description of TS maps.

4.5. Sources not reanalyzed

H.E.S.S. observations have revealed many sources with complex morphology, e.g., RX J0852.0−4622 (also known as Vela Junior), which has a very pronounced shell-like structure (H.E.S.S. Collaboration 2018b), or the Galactic center region, which has multiple point-sources embedded in a very elongated ridge-like emission (H.E.S.S. Collaboration 2018h). Dedicated studies model such regions of emission using complex parametric models, for example, model templates based on molecular data, shell-like models, asymmetric Gaussian models, and combinations thereof. It is challenging to systematically model the emission across the entire Galactic plane using these more complex models, which tend to yield unstable or non-converging fit results because of the large number of free and often poorly constrained parameters. This can be especially problematic in ROIs with multiple, complex overlapping sources.

Given the difficulties with modeling complex source morphologies, we decided to restrict the HGPS analyses to a symmetrical Gaussian model assumption and exclude all firmly identified shell-like sources and the very complex GC region from reanalysis. A complete list of the ten excluded (or cut-out) sources in the HGPS region is given in Table 1. The table also contains four sources that were not significant in the current HGPS analysis but were found to be significant in other dedicated, published analyses; these cases are discussed in detail in Sect. 5.4.3. We refer to these 14 sources in total listed in Table 1 as "EXTERN" HGPS sources and have included these sources in the HGPS source catalog because we wanted to give a complete list of sources in the HGPS region. We also have these sources included in the various distributions, histograms, and other plots

Table 1. Fourteen EXTERN sources in the HGPS catalog, i.e., VHE sources in the HGPS region previously detected by H.E.S.S. that were not reanalyzed in this paper.

Source name	Common name	Reason for not reanalyzing	Reference
HESS J0852−463	Vela Junior	Shell morphology	H.E.S.S. Collaboration (2018b)
HESS J1442−624	RCW 86	Shell morphology	H.E.S.S. Collaboration (2018i)
HESS J1534−571	G323.7−1.0	Shell morphology	H.E.S.S. Collaboration (2018j)
HESS J1614−518	–	Shell morphology	H.E.S.S. Collaboration (2018j)
HESS J1713−397	RX J1713.7−3946	Shell morphology	H.E.S.S. Collaboration (2018f)
HESS J1731−347	G353.6−0.7	Shell morphology	H.E.S.S. Collaboration (2011a)
HESS J1912+101	–	Shell morphology	H.E.S.S. Collaboration (2018j)
HESS J1745−290	Galactic center	Galactic center region	H.E.S.S. Collaboration (2016)
HESS J1746−285	Arc source	Galactic center region	H.E.S.S. Collaboration (2018h)
HESS J1747−281	G0.9+0.1	Galactic center region	Aharonian et al. (2005b)
HESS J1718−374	G349.7+0.2	Not significant in HGPS	H.E.S.S. Collaboration (2015a)
HESS J1741−302	–	Not significant in HGPS	H.E.S.S. Collaboration (2018k)
HESS J1801−233	W 28	Not significant in HGPS	Aharonian et al. (2008d)
HESS J1911+090	W 49B	Not significant in HGPS	H.E.S.S. Collaboration (2018d)

Notes. For each source, we list the reason why it was not reanalyzed and give the reference that was used to fill the parameters in the HGPS source catalog. See Sect. 4.5 and for sources not significant in the HGPS analysis also Sect. 5.4.3.

exploring the global properties of the HGPS sources in Sect. 5.3. The morphological and spectral parameters for those sources were adapted from the most recent H.E.S.S. publication (listed in Table 1)[4].

4.6. Large-scale emission model

We previously demonstrated that there exists VHE γ-ray emission that is large scale and diffuse along the Galactic plane (Abramowski et al. 2014a). In that paper, we constructed a mask to exclude the regions of the plane where significant emission was detected. The latitude profile of excess γ-rays outside this mask clearly showed the presence of significant large-scale γ-ray emission. We do not extend the analysis of this diffuse emission any further here. Whether the emission originates from interactions of diffuse cosmic rays in the interstellar medium or from faint, unresolved γ-ray sources (or a combination thereof) is not investigated. Instead, we take a pragmatic approach and model the large-scale emission present in the HGPS empirically as described in the following.

The presence of a large-scale component of γ-ray emission along the Galactic plane complicates the extraction of the Gaussian γ-ray source components. This large-scale emission can mimic the presence of spurious degree-scale sources in some regions of the plane and it also tends to broaden the Gaussian components that describe otherwise well-defined sources. It is therefore necessary to model the large-scale γ-ray emission to measure the flux and morphology of the HGPS sources more accurately.

To do so, we built an empirical surface brightness model of the large-scale emission (see Fig. 6), where the latitude profile is Gaussian and defined by three parameters: the peak position in latitude, the width, and amplitude of the Gaussian. We estimated the parameters using a maximum-likelihood fit in regions where no significant emission is measurable on small scales, i.e., outside the exclusion regions defined for the ring background model, taking exposure into account. Regardless of the physical origin of the large-scale emission, it is likely to be structured along the plane and not constant.

To estimate the variable parameters of the model, we fit the Gaussian parameters in rectangular regions of width 20° in longitude and height 6° in latitude. We excluded all pixels inside the standard exclusion regions used to produce the background maps (see Sect. 3.2). The Gaussian parameters were dependent on the size of both the exclusion regions and rectangular regions. We found that the typical variations were ∼25%. To obtain a smooth sampling of the variations, we followed a sliding-window approach, distributing the centers of the rectangular regions every 2.5° in longitude and interpolating between these points.

The maximum-likelihood fit compares the description of the data between the cosmic-ray (CR) background only and the CR background plus the model. We used the likelihood ratio test to estimate the significance of adding the large-scale component in each 20-deg-wide window, finding it to be larger than 3σ (TS difference of 9) over most of the HGPS region. Figure 6 shows the resulting best-fit Gaussian parameters together with the associated uncertainty intervals estimated from the likelihood error function. After this fit, we froze the parameters of the model for use in the γ-ray source detection and morphology fitting procedure.

While the approach presented here provides an estimate of the large-scale emission present in the HGPS maps, it does not comprise a measurement of the total Galactic diffuse emission (see discussion in Sect. 5.2).

4.7. Regions of interest

To search for sources, we divided the whole HGPS region into smaller overlapping ROIs. This was necessary to limit both the number of simultaneously fit parameters and the number of pixels involved in the fit.

[4] We note that the values in the HGPS catalog for EXTERN sources do not fully reflect the results of the original publication. Specifically, in some cases the information is incomplete (e.g., when certain measurements were not given in the paper) or not fully accurate (e.g., when the published measurements do not fully agree with the definition of measurements in this paper, or when parameter errors are different due to error inaccuracies in the error propagation when converting to HGPS measures).

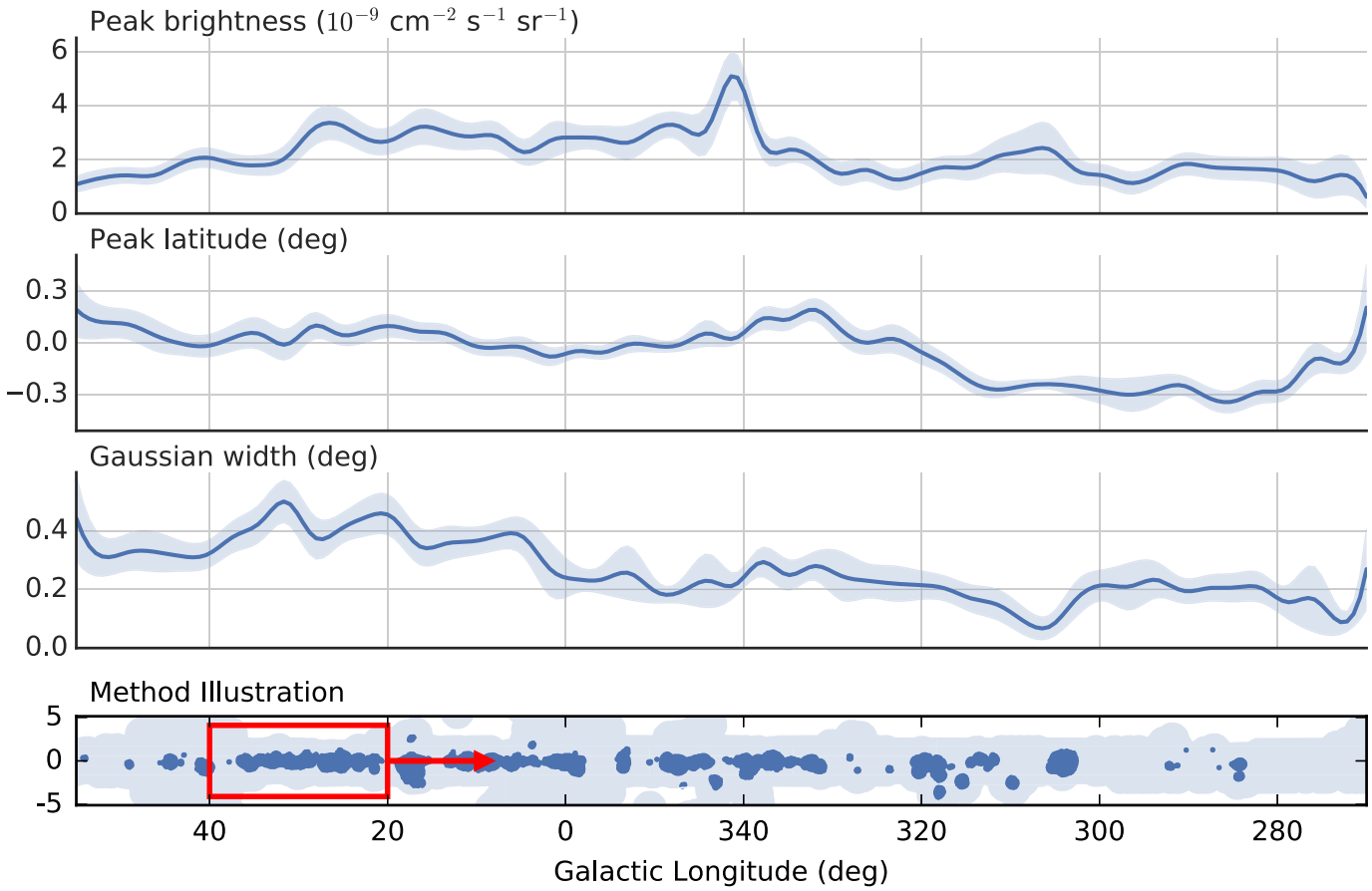

Fig. 6. Distribution of the fit large-scale emission model parameters with Galactic longitude. The *first panel* gives the peak brightness of the large-scale emission model in units of 10^{-9} cm^{-2} s^{-1} sr^{-1} (≈1.3% Crab deg^{-2}). The *second panel* shows the peak position of the Gaussian along the Galactic latitude axis in degrees and the *third panel* shows the width (σ) of the Gaussian in degrees. The solid lines are the result of fitting each set of parameters every 2.5° in longitude and interpolating. The light blue bands show the 1σ error region obtained from the covariance matrix of the likelihood function. The *lower panel* illustrates the 20° wide sliding-window method (red rectangle) that was used to determine the large-scale emission model in areas (shown in light blue) where the HGPS sensitivity is better than 2.5% Crab but outside exclusion regions (shown in dark blue); this is explained in further detail in the main text.

We manually applied the following criteria to define the ROIs:

(a) All significant emission (above 5σ) in the HGPS region should be contained in at least one ROI.
(b) No significant emission should be present close to the edges of an ROI.
(c) The width of each ROI should not exceed ∼10° in longitude to limit the number of sources involved in the fit.
(d) ROIs should cover the full HGPS latitude range from −5° to 5°.

In cases in which criterion (b) could not be fulfilled, we excluded the corresponding emission from the ROI and assigned it to a different, overlapping ROI. Figure A.6 illustrates the boundaries of the 18 ROIs defined with these criteria. Some of the ROIs show regions without any exposure; these regions were masked out and ignored in the subsequent likelihood fit.

4.8. Multi-Gaussian source emission model

After excluding shell-type supernova remnants (SNRs) and the GC region from reanalysis and adding a model for large-scale emission to the background, we modeled all remaining emission as a superposition of Gaussian components. We took the following model as a basis:

$$N_{\mathrm{Pred}} = N_{\mathrm{Bkg}} + \mathrm{PSF} * \left(\mathcal{E} \cdot \sum_i S_{\mathrm{Gauss},i} \right) + \mathcal{E} \cdot S_{\mathrm{LS}}, \tag{9}$$

where N_{Pred} corresponds to the predicted number of counts, N_{Bkg} to the number of counts from the background model, S_{LS} the contribution of the large-scale emission model, $\sum_i S_{\mathrm{Gauss},i}$ the sum of the Gaussian components, and $\mathcal{E}$ the exposure as defined in Eq. (3).

For a given set of model parameters, we integrated the surface brightness distribution S over each spatial bin, multiplied it by the exposure $\mathcal{E}$, and convolved it with the PSF to obtain the predicted number of counts per pixel. For every ROI, we took the PSF at the position of the brightest emission and assumed it to be constant within the ROI.

For the Gaussian components, we chose the following parametrization:

$$S_{\mathrm{Gauss}}(r|\phi,\sigma) = \phi \frac{1}{2\pi\sigma^2} \exp\left(-\frac{r^2}{2\sigma^2}\right), \tag{10}$$

where S_{Gauss} is the surface brightness, ϕ the total spatially integrated flux, and σ the width of the Gaussian component. The offset $r = \sqrt{(\ell-\ell_0)^2 + (b-b_0)^2}$ is defined with respect to the position (ℓ_0, b_0) of the component measured in Galactic coordinates.

We conducted the manual fitting process following a step-by-step procedure. Starting with one Gaussian component per ROI, we added Gaussian components successively and refit all of the parameters simultaneously until no significant residuals were left. In each step, we varied the starting parameters of the fit to avoid convergence toward a local minimum. The significance of the tested component was estimated from

$$\mathrm{TS} = C(\text{with component}) - C(\text{best solution without component}). \quad (11)$$

We considered the component to be statistically significant and kept it in the model when the TS value exceeded a threshold of TS = 30. The probability of having one false detection in the HGPS survey from statistical background fluctuations is small (p = 0.03). This number was determined by simulating 100 HGPS survey counts maps as Poisson-fluctuated background model maps, followed by a multi-Gaussian peak finding method, resulting in three peaks with TS ≥ 30. However, we note that this assessment of expected false detections lies on the assumption that the hadronic background as well as the large-scale and source gamma-ray emission model are perfect. In HGPS, as in any other Galactic plane survey with complex emission features, this is not the case. Several components with TS ≥ 30 are not confirmed by the cross-check analysis (see Sect. 4.9).

The definition of TS above differs slightly from the definition given in Eq. (7). For a single, isolated component, both values are identical. However, if a second, overlapping component exists, some of the emission of the first source is modeled by the second source, reducing the significance of the first. We therefore estimated the significance of a component from the TS difference in the total model of the ROI and not from the TS difference compared to the background-only model.

Applied to real data, we found a total of 98 significant Gaussian components using this procedure and TS threshold. Figure 7 depicts the residual $\sqrt{\mathrm{TS}}$ distributions over the entire HGPS region. These distributions demonstrate that there is approximate agreement with a normal Gaussian distribution; in particular, we find no features above the $\sqrt{\mathrm{TS}} = \sqrt{30}$ detection threshold. Inherent imperfections in the background, large-scale emission models and source emission models lead to a slight broadening of the distributions with respect to a normal distribution, as expected.

For reference, the 98 Gaussian components have been assigned identifiers in the format `HGPSC NNN`, where `NNN` is a three-digit number (counting starts at 1), sorted by right ascension (which is right to left in the survey maps). The complete list of components is provided in the electronic catalog table (see Table A.3).

4.9. Component selection, merging, and classification

We repeated the entire modeling procedure described in the previous section with a second set of maps produced with an independent analysis framework (see Sect. 2.3). Five of the 98 HGPS components were not significant in the cross-check analysis and were therefore discarded (see Fig. 5 and Table A.3). Those components we labeled with `Discarded Small` in the column `Component_Class` of the FITS table.

We observed two other side effects of the modeling procedure. Firstly, very bright VHE sources, even some with center-filled morphologies such as Vela X, decomposed into several Gaussian components, modeling various morphological details

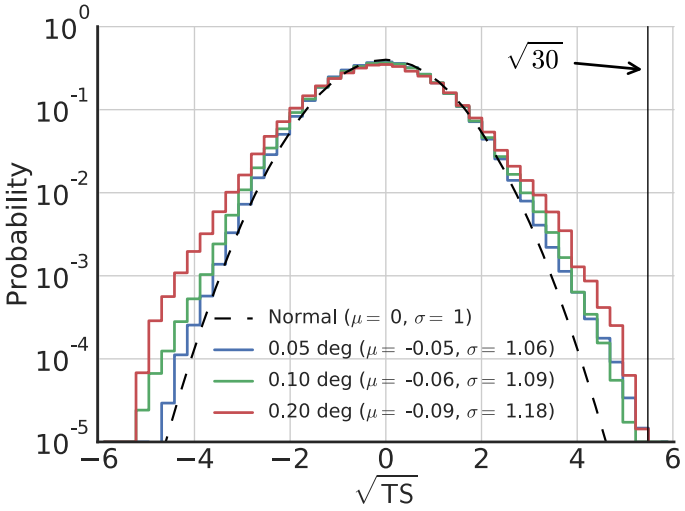

Fig. 7. Residual significance distribution after taking the HGPS emission model into account (see Fig. 5, *middle panel*). The significance was computed using a Gaussian source morphology of size σ = 0.05°, 0.10°, and 0.20°. A vertical line at $\sqrt{\mathrm{TS}} = \sqrt{30}$ is shown, corresponding to the detection threshold for the HGPS multi-Gaussian modeling. The sky region corresponding to this distribution includes pixels inside exclusion regions, except for the Galactic center and shell-type SNRs, which were not modeled for the HGPS (see Table 1, lower panel of Fig. 5 and Fig. A.6).

of the source. Figure 5 illustrates this effect: there are two multi-component sources shown. Therefore in cases where overlapping components were not clearly resolved into separate emission peaks, we merged them into a single source in the HGPS catalog. In total, we found 15 such multicomponent sources: ten consisting of two Gaussian components and five consisting of three Gaussian components. It would be intriguing to analyze the complex morphology of these multicomponent sources in greater detail, but this kind of analysis is beyond the scope of this survey paper. We labeled components that are part of a multicomponent source as `Source Multi`. We used the label `Source Single`, respectively, if there is only one component modeling the source.

The second side effect was that some of the Gaussian components appeared to have very large sizes coupled with very low surface brightness. We interpret these components as artifacts of the modeling procedure, which picks up additional diffuse γ-ray emission that is not covered by our simple large-scale emission model (Sect. 4.6). For example, as shown in Fig. 5, the emission around $\ell \sim 345°$ initially comprised three model components: two components that clearly converged on the two discrete emission peaks visible in the excess map and one very large and faint component that appeared to be modeling large-scale emission along the Galactic plane in between the two and not clearly related to either of the two peaks. In total, we found ten such large-scale components (see Table A.3), which we discarded and did not include in the final HGPS source catalog as they are likely low-brightness diffuse emission. We labeled this class of components as `Discarded Large` in the component list.

4.10. Source characterization

4.10.1. Position, size, and flux

For HGPS sources that consist of several components, we determined the final catalog parameters of the sources as follows.

Flux. The total flux is the sum of the fluxes of the individual components

$$F_{\rm Source} = \sum_i F_i. \quad (12)$$

Position. We calculated the position by weighting the individual component positions with the respective fluxes. The final $\ell_{\rm Source}$ and $b_{\rm Source}$ coordinates of the source are written as

$$\ell_{\rm Source} = \frac{1}{F_{\rm Source}} \sum_i \ell_i F_i \quad \text{and} \quad b_{\rm Source} = \frac{1}{F_{\rm Source}} \sum_i b_i F_i. \quad (13)$$

Size. We obtained the size in ℓ and b directions from the second moment of the sum of the components as follows:

$$\sigma^2_{\ell,\rm Source} = \frac{1}{F_{\rm Source}} \sum_i F_i \cdot (\sigma_i^2 + \ell_i^2) - \ell^2_{\rm Source} \quad (14)$$

$$\sigma^2_{b,\rm Source} = \frac{1}{F_{\rm Source}} \sum_i F_i \cdot (\sigma_i^2 + b_i^2) - b^2_{\rm Source,} \quad (15)$$

where additionally we defined the average circular size as

$$\sigma_{\rm Source} = \sqrt{\sigma_{\ell,\rm Source}\, \sigma_{b,\rm Source}}. \quad (16)$$

We computed the uncertainties of the parameters using Gaussian error propagation, taking the full covariance matrix estimate from the fit into account.

4.10.2. Size upper limits

In the morphology fit, we did not take into account uncertainties in the PSF model. However, studies using H.E.S.S. data (e.g., Stycz 2016) have revealed a systematic bias on the size of point-like extragalactic sources on the order of $\sigma_{\rm syst} = 0.03°$, so we have adopted this number as the systematic uncertainty of the PSF.

Given a measured source extension $\sigma_{\rm Source}$ and corresponding uncertainty $\Delta\sigma_{\rm Source}$, we used the following criterion to claim a significant extension beyond the PSF:

$$\sigma_{\rm Source} - 2\Delta\sigma_{\rm Source} > \sigma_{\rm syst}, \quad (17)$$

i.e., if the extension of a source is $2\Delta\sigma_{\rm Source}$ beyond the systematic minimum $\sigma_{\rm syst}$. If this criterion is not met, we consider the source to be compatible with being point-like and define an upper limit on the source size as follows:

$$\sigma_{\rm UL} = \max(\sigma_{\rm syst}, \sigma_{\rm Source} + 2\Delta\sigma_{\rm Source}). \quad (18)$$

4.10.3. Localization

The HGPS source location error is characterized by error circles with radius R_α at confidence levels $\alpha = 0.68$ and $\alpha = 0.95$, computed as

$$R_\alpha = f_\alpha \times \sqrt{\Delta\ell^2_{\rm stat} + \Delta\ell^2_{\rm syst} + \Delta b^2_{\rm stat} + \Delta b^2_{\rm syst}}. \quad (19)$$

The values $\Delta\ell_{\rm stat}$ and $\Delta b_{\rm stat}$ are the statistical errors on Galactic longitude ℓ and latitude b, respectively, from the morphology fit. For the H.E.S.S. systematic position error, a value of $\Delta\ell_{\rm syst} = \Delta b_{\rm syst} = 20'' = 0.0056°$ per axis was assumed, following the method and value in (Acero et al. 2010b).

Assuming a Gaussian probability distribution, the factor f_α is chosen as $f_\alpha = \sqrt{-2\log(1-\alpha)}$ for a given confidence level α (see Eq. (1) in Abdo et al. 2009b).

4.10.4. Source naming

The 78 HGPS catalog sources have been assigned source names in the format `HESS JHHMM±DDd`, where `HHMM` and `±DDd` are the source coordinates in right ascension and declination, respectively. For new sources, the source name is based on the source location reported in this paper. For sources that had been assigned names in previous H.E.S.S. publications or conference presentations, the existing name was kept for the HGPS catalog, even if the position in the HGPS analysis would have led to a different name. Similarly, the source candidates (or hotspots, see Sect. 5.6.17) have been assigned names in the format `HOTS JHHMM±DDd`.

4.11. Source spectra

After detection and subsequent morphological analysis of the sources, we measured a spectrum for each of the sources using an aperture photometry method. In this method we sum the ON counts within an aperture defined as a circular region centered on the best-fit position of each source. We fit a spectral model within that aperture using an ON-OFF likelihood method (Piron et al. 2001), where the OFF background is estimated using reflected regions defined on a run-by-run basis (Fomin et al. 1994; Berge et al. 2007). Based on the morphology model, we then corrected the measured flux for containment and contamination from other nearby sources. For the spectral analysis, we applied standard cuts, resulting in energy thresholds in the range 0.2–0.5 TeV, lower than the thresholds achieved using hard cuts in the detection and morphology steps. Figure 2 shows the variation of the threshold with longitude. In the following sections, we describe the spectral analysis process in more detail.

4.11.1. Aperture photometry and background estimate

The optimal choice for the size for the spectral extraction region is a balance between including a large percentage of flux from the source and limiting the contamination of the measurement by hadronic background events, large-scale emission, and other nearby sources. Following these requirements, we chose the aperture radius $R_{\rm spec}$ as follows:

- $R_{\rm spec} = R_{70}$ for 34 medium-size sources, where R_{70} is the 70% containment radius measured on the PSF-convolved excess model image (`R70` in the catalog),
- minimum $R_{\rm spec} = 0.15°$ for 21 small (`R70` $< 0.15°$) sources,
- maximum $R_{\rm spec} = 0.5°$ for 9 very large (`R70` $> 0.5°$) sources.

A minimal aperture radius of 0.15° was imposed to make the measurement of the source spectrum more robust against systematic uncertainties of the PSF and the source morphology assumption.

The aperture radius was limited to a maximum radius of $R_{\rm spec} = 0.50°$ to limit the fraction of observations that cannot be used for the spectrum measurement because no background estimate could be obtained.

As illustrated in Fig. 8, the background is estimated using the reflected region method (Fomin et al. 1994; Berge et al. 2007). For every spectral extraction region (ON region), corresponding OFF regions with the same shape and offset to the pointing position are chosen outside exclusion regions.

The method works well for small, isolated γ-ray sources such as active galactic nuclei (AGNs) or the Crab Nebula, where typically ∼10 OFF regions are found in every observation. This results in a well-constrained background, and all the exposure can be used for the spectral measurement. Because of the high

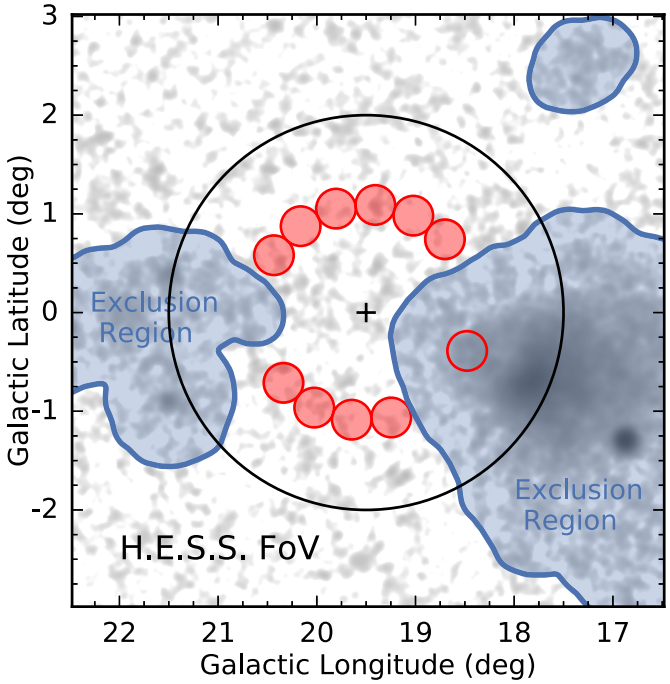

Fig. 8. Illustration of reflected region background estimation for spectra (Sect. 4.11.1). The HGPS significance image is shown in inverse grayscale and exclusion regions as blue contours. The analysis FoV for one observation is shown as a black circle with 2° radius and a black cross at the observation pointing position. The non-filled red circle illustrates the ON region for spectral analysis; the filled red circles indicate the OFF regions.

density of sources in the Galactic plane, large areas of emission are excluded and only few reflected regions can be found. This effectively results in a loss of exposure for the spectrum measurement compared to the map measurement. For the HGPS analysis this is a large problem because of the very extensive exclusion regions used: 64% of the livetime is lost for spectral analysis compared to the total available livetime that is used in the map-based analysis. For each source, see the `Livetime_Spec` and `Livetime` information in the source catalog. In cases where the loss of exposure is very high, the background cannot be well constrained, which consequently results in spectral parameters that are not well constrained. The following sources are affected by this issue:

- Sources located in or near large exclusion regions (see Fig. A.6). An area of width ~2° is often excluded along the Galactic plane, and this covers a significant portion of the analysis FoV, which has a diameter of 4°.
- Sources with large ON regions.
- Sources observed with too small or too large offsets because they are located close to other sources that were covered with dedicated observations.

4.11.2. Flux containment and contamination correction

By construction and because of additional effects such as PSF leakage or source morphologies featuring tails, the spectral extraction region does not contain the full flux of the source. Additionally, the large-scale emission model and other nearby Gaussian components bias the flux measurement within the spectral region. Based on this emission model, we separate the contributions from the different components and derive a correction factor for the spectral flux measurement.

The total flux in the spectral measurement region is

$$F^{\mathrm{ON}}_{\mathrm{Total}} = F^{\mathrm{ON}}_{\mathrm{Source}} + F^{\mathrm{ON}}_{\mathrm{LS}} + F^{\mathrm{ON}}_{\mathrm{Other}}, \tag{20}$$

where $F^{\mathrm{ON}}_{\mathrm{Source}}$ is the contribution from the source itself, $F^{\mathrm{ON}}_{\mathrm{LS}}$ is the contribution from the large-scale emission model, and $F^{\mathrm{ON}}_{\mathrm{Other}}$ is the contribution from nearby sources and other, discarded Gaussian emission components.

Assuming F_{Source} is the flux measurement from the morphology fit, we define the correction factor as

$$C_{\mathrm{Correction}} = F_{\mathrm{Source}}/F^{\mathrm{ON}}_{\mathrm{Total}}. \tag{21}$$

To summarize the contributions from the large-scale emission model and other sources in close (angular) proximity, we define a quantity called contamination. This quantity measures the fraction of flux within the spectral region that does not originate from the source itself and is written as

$$C_{\mathrm{Contamination}} = \frac{F^{\mathrm{ON}}_{\mathrm{LS}} + F^{\mathrm{ON}}_{\mathrm{Other}}}{F^{\mathrm{ON}}_{\mathrm{Total}}}. \tag{22}$$

Additionally, we define the containment of a source as the ratio between the flux of the source within the spectral measurement region $F^{\mathrm{ON}}_{\mathrm{Source}}$ (taking the morphology model into account) and the total flux obtained from the morphology fit F_{Source} as follows:

$$C_{\mathrm{Containment}} = F^{\mathrm{ON}}_{\mathrm{Source}}/F_{\mathrm{Source}}. \tag{23}$$

The HGPS catalog provides all the quantities mentioned in this section, and all aperture-photometry based flux measurements in the HGPS catalog (see Table A.2) are corrected by the factor given in Eq. (21) (see Sects. 4.11.3 and 4.11.4).

We note that this region-based spectral analysis method with a single integral flux correction factor assumes energy-independent source morphology. The spectra obtained for sources with energy-dependent morphology does not correspond to the correct total emission spectra of the sources. Currently energy-dependent morphology has been clearly established for two sources (HESS J1303−631 and HESS J1825−137), and there are hints of energy-dependent morphology for a few more. Furthermore, using an integral flux correction factor is not fully correct because the HGPS PSF is somewhat dependent on energy (smaller PSF at higher energies). The resulting inaccuracy on HGPS spectral results is small, because we have chosen a minimal spectral aperture radius of 0.15°, which contains most of the emission for point sources at all energies. Generally, spectra for sources with large correction factors are likely to be less accurate, because the morphology models used to compute the correction are only approximations.

4.11.3. Spectral model fit

We performed the spectral fits on the stacked[5] observations, using the ON-OFF Poisson likelihood function, referred to as the W statistic (WSTAT) in XSPEC[6]. For each observation, we applied a safe energy threshold (see Sect. 3.1) cut at low energies, and the maximum energy was chosen at the highest event

[5] Observation stacking was performed as described here: http://cxc.harvard.edu/ciao/download/doc/combine.pdf

[6] See https://heasarc.gsfc.nasa.gov/xanadu/xspec/manual/XSappendixStatistics.html or Appendix A of Piron et al. (2001).

energy in the stacked counts spectrum for the on region (resulting in a maximum energy of 30–90 TeV). Energy dispersion was not taken into account via a matrix, but in an approximate way in which the effective area is computed in such a way that it results in fully correct spectral results for power-law spectra with spectral index 2, and, given the good energy resolution of H.E.S.S., only small errors are made for other spectral shapes (Hoppe 2008a).

To describe the spectral shape of the VHE γ-ray emission, we fit a PL model to the data, i.e.,

$$\phi(E) = \frac{\mathrm{d}N}{\mathrm{d}E} = \phi_0 \left(\frac{E}{E_0}\right)^{-\Gamma}, \tag{24}$$

where ϕ_0 is the differential flux at a reference (pivot) energy E_0 and Γ is the spectral index. In addition, we also fit an exponential cutoff power-law (ECPL) model,

$$\phi(E) = \phi_0 \left(\frac{E}{E_0}\right)^{-\Gamma} \exp(-\lambda E), \tag{25}$$

which additionally contains the inverse cutoff energy $\lambda = 1/E_{\mathrm{cutoff}}$ as a third, free parameter. The reference (pivot) energy E_0 is not a free parameter in either model; we compute this parameter on a source-by-source basis to minimize the correlation between the other fit parameters.

We computed integral fluxes as

$$F(E_1, E_2) = \int_{E_1}^{E_2} \phi(E)\,\mathrm{d}E, \tag{26}$$

usually for the energy band above 1 TeV, with integral flux errors computed using Gaussian error propagation. We computed energy fluxes for a given energy band as

$$G(E_1, E_2) = \int_{E_1}^{E_2} E\,\phi(E)\,\mathrm{d}E. \tag{27}$$

The source catalog provides the PL fit results (see Table A.2 for a description of columns) for every source and the ECPL parameters where the ECPL model is more likely ($\mathrm{TS} = W_{\mathrm{PL}} - W_{\mathrm{ECPL}} > 9$). All aperture-photometry based flux measurements are corrected by the factor given in Eq. (21).

4.11.4. Flux points

Flux points are estimates of the differential flux ϕ at a given set of reference energies E_{ref}. To compute flux points for the HGPS catalog, we chose a method similar to that used for the *Fermi*-LAT catalogs (see, e.g., Sect. 5.3 in Acero et al. 2015). For every source we selected a total number of six bins (E_1, E_2) in reconstructed energy, logarithmically spaced between the safe energy threshold and a maximum energy of 50 TeV. The reference energy for the flux point estimation was set to the logarithmic bin center $E_{\mathrm{ref}} = \sqrt{E_1 E_2}$. The differential flux ϕ was computed via a one-parameter likelihood fit (same method as described in Sect. 4.11.3), under the assumption of the global best-fit PL and using only the data within the bin of reconstructed energy (E_1, E_2). An 1σ asymmetric error on ϕ was computed from the likelihood profile, and for spectral points of small significance ($\mathrm{TS} < 1$), in addition an upper limit on ϕ was computed at 95% confidence level. All spectral point measurements in the HGPS catalog are corrected by the factor given in Eq. (21).

4.12. Method discussion

The sensitivity profile and map shown in Fig. 4 were computed assuming a point-like source morphology and using the Li & Ma significance estimation. The likelihood fit method including the large-scale emission model component used for the catalog production fundamentally differs from that. We qualitatively discuss below the most important differences and their influence on the effective sensitivity with which the catalog was produced.

In Sect. 3.4.4, the sensitivity was defined as the minimum required flux for a source to be detected with a certain level of confidence. Assuming the source is extended, which applies to most of the Galactic sources found by H.E.S.S., the total flux of the source is distributed over a larger area on the sky. Given a fixed background level, the signal-to-noise ratio is decreased and the sensitivity scales with the size of the source as

$$F_{\mathrm{min}}(\sigma_{\mathrm{source}}) \propto \sqrt{\sigma^2_{\mathrm{source}} + \sigma^2_{\mathrm{PSF}}}, \tag{28}$$

where σ_{source} is the size of the source and σ_{PSF} the size of the PSF (Hinton & Hofmann 2009). It is constant for sources smaller than the PSF and increases linearly with source size for sources much larger than the PSF.

For low surface brightness sources close to the Galactic plane, high levels of contamination (defined as in Eq. (22)) from the large-scale emission model were observed. This effectively reduces the sensitivity close to the Galactic plane and even caused a few previously detected H.E.S.S. sources to fall below the detection threshold (see also Sect. 5.4.3) chosen for the HGPS analysis. For sources far from the Galactic plane, however, the influence of the large-scale emission can be neglected.

Systematic and statistical background uncertainties, which are neglected in this analysis, bias the sensitivity for large, extended sources. Neglecting background fluctuations in the likelihood fit can lead to an overestimation of the significance of large sources, which can lead to unreliable detections of large emission components. In addition, the adaptive ring method (Sect. 3.2.3), which has a minimal inner ring radius of 0.7°, does not provide a reliable background estimate for those large emission components.

Systematic uncertainties of various origins affect the spectral parameters of the sources. In addition to the transparency of the atmosphere, calibration, and event reconstruction (see Sect. 2), the analysis method itself can introduce uncertainties. In particular, the background and large-scale emission emission model, and the source extraction and measurement method (multi-Gaussian morphology and aperture photometry) influence the flux and spectral index measurement. We estimate the relative systematic uncertainties of the flux extracted from the maps (Sect. 3) and from the spectrum (Sect. 4.11) to be 30%; for the spectral index (Sect. 4.11) we estimate an absolute systematic uncertainty of 0.2. This estimate is based on the scatter seen in the cross-check analysis and other analyses (e.g., a source catalog extracted without a large-scale emission model component). For individual difficult sources (poor containment, large contamination, complex, and marginally significant morphology features), larger systematics may arise (see Sects. 5.4 and 5.5). We note that the systematic uncertainties quoted here are the same as in the previous HGPS publication (Aharonian et al. 2006a), and, as expected for a population of extended sources in the Galactic plane, these values are slightly larger than the systematic uncertainties previously estimated for isolated point-like sources such as the Crab Nebula (Aharonian et al. 2006b).

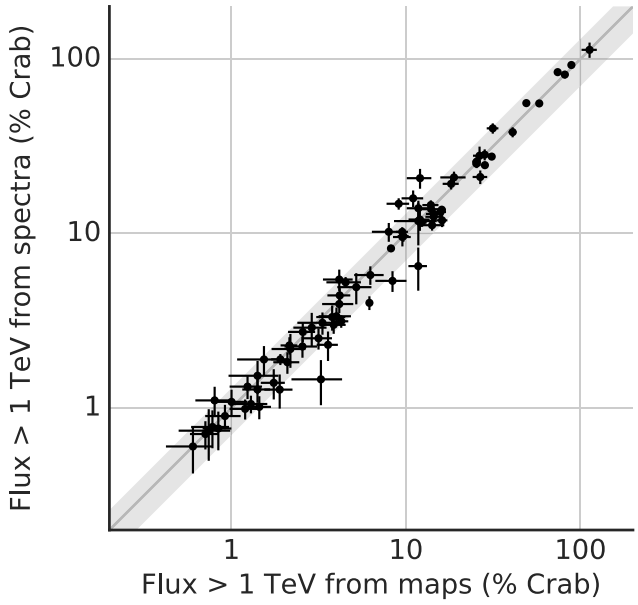

Fig. 9. Comparison of integral source flux measurements above 1 TeV as calculated with two different methods. The flux estimate from maps is the total source flux according to the morphology model fit, assuming a spectral index of $\Gamma = 2.3$ (the `Flux_Map` column in the catalog). The flux estimate from spectra is computed from the total source best-fit spectral model extracted using aperture photometry and aperture correction (the `Flux_Spec_Int_1TeV` column in the catalog). The gray band in the background illustrates a systematic uncertainty of 30% on the flux values.

A comparison of the two methods presented in this paper for calculating HGPS source integral flux ($E > 1$ TeV) was performed as a diagnostic test (see scatter plot in Fig. 9). The flux show on the x-axis is the total source flux estimated from the source morphology fit on the maps (given by Eq. (12)), assuming a power-law spectrum with index $\Gamma = 2.3$. The flux estimate on the y-axis was obtained from a spectral analysis (see Eq. (26) in Sect. 4.11), using a PL or ECPL spectral model assuption (best-fit model) and an aperture photometry method that includes a containment and contamination correction according to the HGPS multi-Gaussian plus large-scale emission model. One can see that the two flux estimates agree very well for most sources within the statistical errors and the 30% flux systematic uncertainty that we quote above. There are exceptions however, which can to a large degree be attributed to differences in the underlying morphology and spectral model assumptions of the two flux estimators. We note that when comparing either of these HGPS source flux estimates against the cross-check, the level of agreement is similar, but not quite as good (see Sect. 5.5 for a discussion of individual cases). When comparing against previous publications, the scatter is even larger (flux differences up to a factor of 2 in a few cases), which can in many cases be understood to be the result of differences in morphology model (of the source itself, of nearby overlapping sources, or the large-scale emission model) or the spectral extraction region; most previous publications did not apply containment or contamination corrections.

5. Results and discussion

This section presents the results and a discussion of the HGPS based on the data set (Sect. 2), maps (Sect. 3), and catalog (Sect. 4).

5.1. Source associations and firm identifications

Determining the physical nature of a VHE γ-ray source often requires detailed spectral and morphological characterization of the VHE emission and availability of complementary MWL information. Finding a likely counterpart of a point-like VHE source is generally easy thanks to the limited region of the sky to investigate. For an extended source, such as the vast majority of the HGPS sources, the procedure is often much more involved because of multiple spatial associations, unless the VHE morphology is similar to that observed at other wavelengths (e.g., for a large shell-type SNR).

We therefore make a distinction between source associations and firm identifications of sources. The former is a list of astronomical objects, extracted from catalogs of plausible counterparts, which are are found to be spatially coincident with the HGPS source. When particularly solid evidence exists that connects one of these associated objects to the VHE emission, such as variability or shell-type morphology, we consider the HGPS source to be firmly identified.

In Sect. 5.1.1 we first describe the systematic association procedure, followed by the discussion of the results of this search for plausible counterparts in Sect. 5.1.2. Finally, we present the list of firmly identified HGPS sources in Sect. 5.1.3.

5.1.1. Source association procedure

Our objective is to associate each HGPS source with plausible counterparts found among nearby objects in the most relevant counterpart catalogs (that is catalogs of objects already identified as VHE emitters such as SNRs and pulsar wind nebulae and high energy γ-ray sources, see Table 2). We search for these counterparts in a region larger than the nominal HGPS source size (its 68% containment radius); we associate all the objects whose cataloged positions are at an angular distance smaller than the source spectral extraction radius, $R_{\rm SPEC}$ (Sect. 4.11.1; see also Fig. A.2 ff.). This spatial criterion is motivated by the fact that often the origin of the relativistic particles is significantly offset from the VHE centroid, for example, when VHE pulsar wind nebulae (PWNe) are offset from energetic pulsars or extended well beyond their X-ray PWNe counterparts. We expect this procedure to be affected by source confusion (multiple associations that are difficult to disentangle), especially for larger VHE sources.

This criterion is a compromise between the number of spurious associations and the number of missed associations. A spurious association would be one with a counterpart that is physically unrelated to the HGPS source (e.g., a chance spatial coincidence in the same region of the sky). A missed association would be a real counterpart that is not selected by the procedure (e.g., a pulsar significantly offset from a VHE source could be missed even though it is known to generate a PWN). As a consequence of this spatial criterion, larger sources naturally has a larger number of associated objects. The criterion is intended to be loose (inclusive) to minimize missed associations at the expense of including potentially spurious associations. Nonetheless, this procedure has certain limitations, for example, difficulties in associating VHE emission with an SNR if the emission was produced in offset molecular clouds illuminated by cosmic rays that escaped from the SNR.

In the following paragraphs, we briefly describe the catalogs used for the automatic association procedure applied to search for counterparts. We also describe a list of additional objects that have been associated with HGPS sources in previous

Table 2. Results of the automatic association procedure for each catalog used (see main text for details and selections applied).

Type	Number of objects in HGPS region	Total number of associations	Number of HGPS sources with at least 1 association
2FHL sources	44	31	29
3FGL sources	352	64	40
Supernova remnants	211	24	21
Pulsar wind nebulae	29	16	16
Composite remnants	42	21	20
Energetic pulsars	222	47	42
Extra associations	–	20	–

Notes. The second column lists the numbers of objects in the HGPS survey region for each catalog. The third column gives the total number of associations found. The last column gives the number of HGPS sources having at least one associated object of a given category. The difference between the two last columns is only large for 3FGL because 3FGL is the only counterpart catalog for which the source density is so high that many HGPS sources are associated with multiple 3FGL sources. Out of the 78 HGPS sources, only 11 are left without any association.

publications but are not present in the counterpart search catalogs. We note that some of these catalogs contain a single, specific type of object (e.g., SNRs), whereas other catalogs contain multiple types of physical objects because they are the result of broad surveys at energies relevant to the HGPS (e.g., the *Fermi*-LAT catalogs).

High-energy γ-ray sources. We searched for associated high-energy (HE) γ-ray sources in the *Fermi*-LAT 2FHL source catalog (Ackermann et al. 2016) and the full 3FGL catalog (Acero et al. 2015). The 2FHL catalog covers the 50 GeV to ∼2 TeV energy range, and the 3FGL catalog covers the 0.1–300 GeV range. They contain 44 and 352 sources in the HGPS region, respectively. We expect the *Fermi*-LAT catalogs to contain a significant number of HGPS sources. In the case of 2FHL, this is due to its energy range, which partially overlaps that of the HGPS, and its sensitivity, which reaches ∼3–4% Crab in the HGPS region (Ackermann et al. 2016). But even without such overlaps, we expect to find many *Fermi*-LAT associations, since many objects emit γ-rays following a spectrum that extends from the HE to the VHE range. Even for noncontinuous spectra we expect to find numerous associations, for example, when a pulsar emits GeV emission detected by *Fermi*-LAT and its wind nebula emits TeV emission detected by H.E.S.S.

Supernova remnants and pulsar wind nebulae. Supernova remnants and PWNe are among the most common particle accelerators in the Galaxy and are well-known VHE γ-ray emitters. Nonetheless, it is often challenging to establish associations between SNRs and VHE sources. For example, only specific regions of an SNR shell could be emitting or neighboring molecular clouds could be illuminated by multi-TeV particles that escaped the shock front of the SNR. Pulsar wind nebulae evolve as their pulsar ages and the available rotational energy (spin-down power) decreases. Since the X-ray synchrotron radiation from PWNe arises from higher energy electrons than the IC radiation in the VHE gamma-ray band, and the cooling time of the electrons decreases with their energy ($t_c = E/(\mathrm{d}E/\mathrm{d}t)$, for radiative losses $t_c \propto 1/E$) we expect PWNe to shine longer in VHE gamma rays. Furthermore, a decreasing magnetic field with age can limit the emission time in radio and X-rays without affecting the VHE emission. As a result, some old PWNe should be undetectable outside the VHE γ-ray domain (see, e.g., Aharonian et al. 1997; de Jager & Djannati-Ataï 2009; H.E.S.S. Collaboration 2018e). For such old PWNe only the detection of a middle-aged energetic pulsar in the vicinity of a VHE source can provide evidence toward the true nature of the VHE emission.

To search for SNR and PWN associations, we take the most complete catalog of SNRs and PWNe to date into account, SNRcat[7] (Ferrand & Safi-Harb 2012). The SNRcat is a census of Galactic supernova remnants and their high-energy observations. It is based on the radio Catalogue of Galactic Supernova Remnants (Green 2014) but additionally includes other types of remnants in an effort to be as complete and up-to-date as possible. In particular, it contains plerionic objects, PWNe with no observed shell. The possible presence of a PWN is usually assessed based on the presence of diffuse, nonthermal emission in radio, X-rays, or even γ-rays. Several of these cataloged objects have been classified by SNRcat as candidate PWNe solely because of the presence of VHE emission in the vicinity of an energetic pulsar. We removed those objects from the catalog used in our association procedure to avoid cases in which we might misleadingly self-associate.

For the association procedure, we split the SNRcat objects into three subsets based on their apparent type. The first subset consists of objects that have no evidence of nebular emission and mostly belong to the shell or filled-center types in SNRcat; this subset contains 211 objects within the HGPS region. The second subset consists of objects that are listed in SNRcat as PWNe (or PWNe candidates) showing no evidence for shell-like emission; this subset contains 29 objects within the HGPS region. The third subset consists of objects showing evidence of both shell and nebular emission, which we refer to as composite objects; this subset contains 42 objects within the HGPS region. For a further discussion of a potential PWN nature of these objects see the population study presented in H.E.S.S. Collaboration (2018e).

Energetic pulsars. We selected energetic pulsars from version 1.54 of the ATNF catalog of radio pulsars (Manchester et al. 2005). We excluded millisecond pulsars because they are not expected to power VHE PWNe and applied a cut on the spin-down energy flux $\dot{E}/d^2 > 10^{33}$ erg s^{-1} kpc^{-2} on the remaining pulsars. In addition, to take into account energetic pulsars of unknown distance, we included all objects with a spin-down

[7] http://www.physics.umanitoba.ca/snr/SNRcat, accessed Oct 10, 2015.

luminosity $\dot{E} > 10^{34}$ erg s^{-1}, resulting in a total of 222 pulsars used in the association procedure. We did not take into account pulsars that do not have a measured $\dot{E}$. It is important to note that pulsars represent indirect associations: the associated pulsars are not directly emitting the unpulsed VHE γ-ray emission found in the HGPS, but rather indicate that they could be powering a PWN that directly emits such emission.

5.1.2. Association results and discussion

HE γ-ray sources. Of the 352 3FGL sources present in the HGPS region, we find 64 to be associated with an HGPS source. As expected, we also find a large portion of the 44 2FHL sources in the HGPS region to be associated with HGPS sources: only 13 of these have no HGPS counterpart. One of these sources is notably coincident with the VHE source candidate HOTS J1111−611 (Sect. 5.6.17). Many of the other 2FHL sources lacking an HGPS association tend to be located in low-sensitivity parts of the HGPS region. Only four 2FHL sources in parts of the HGPS with good sensitivity show no significant VHE emission in the HGPS: Puppis A (H.E.S.S. Collaboration 2015b), 2FHL J0826.1−4500, η Carinae, and the composite SNR G326.3−1.8 (Temim et al. 2013).

Supernova remnants. We find 24 of the 78 HGPS sources to be associated with shell-like SNRs. Given the large number of such objects in the HGPS region (211) and given their sizes, the number of chance coincidences is non-negligible. This is to be expected since we have not tried to specifically match SNR and HGPS source positions and sizes as in Acero et al. (2016). Nonetheless, as discussed below, we find six known shells in the HGPS to be firmly identified and two more to be VHE shell candidates based on their specific morphologies (H.E.S.S. Collaboration 2018j). We study the population of known SNRs in the HGPS further in a companion paper (H.E.S.S. Collaboration 2018l).

Pulsar wind nebulae and composites. We find 37 of the SNRcat objects (in the HGPS region) containing a PWN or PWN candidate to be associated with an HGPS source. Conversely, we find more than 40% of HGPS sources to have at least one associated object in the PWN or composite classes. This supports the notion that systems containing PWNe are prolific VHE emitters. As discussed below, we are able to firmly identify about half of these associations using additional observational evidence such as similar MWL morphology or energy-dependent γ-ray morphology.

Pulsars. We find 47 of all the HGPS sources to be associated with an energetic pulsar. This suggests that the population of HGPS sources contains numerous PWNe. However, we selected a relatively low threshold $\dot{E}$ in our association criteria to minimize missed associations. We quantitatively study such selection effects in a companion paper (H.E.S.S. Collaboration 2018e) that provides a detailed look at the physical characteristics of firmly identified PWNe and a list of candidate PWN identifications based on various expected characteristics.

Extra associations. For completeness, in addition to the associations obtained through the catalog-based, automatic procedure, we add a list of 20 extra associated objects that are plausible counterparts for some HGPS sources and are not covered by the limited set of catalogs we use. Previous publications had proposed most of these associations, often thanks to dedicated MWL observations of VHE source regions (e.g., the X-ray source XMMU J183245−0921539 and HESS J1832−093). We propose other associations in this work for some of the new sources (Sect. 5.6). We also include the original identifiers of VHE sources discovered first by other instruments (e.g., VER J1930+188, which corresponds to HESS J1930+188). Table A.9 includes all of these extra associations, labeled "EXTRA".

Sources without physical associations. Eleven HGPS sources do not have any associations with known physical objects, although some are associated with HE γ-ray sources. We list and discuss these briefly here (the new VHE sources are discussed in Sect. 5.6):

1. HESS J1457−593 is one of the new sources detected in the HGPS analysis. Although the automatic association procedure does not find any counterparts, the VHE γ-ray emission may originate in a molecular cloud illuminated by CRs that escaped from the nearby but offset SNR G318.2+0.1. This scenario is briefly described in Sect. 5.6.2.
2. HESS J1503−582 is also a new HGPS source and does not have any compelling association except for the HE γ-ray sources 3FGL J1503.5−5801 and 2FHL J1505.1−5808, neither of which is of a firmly identified nature. We describe this enigmatic source in Sect. 5.6.4.
3. HESS J1626−490 has only one association, with the HE γ-ray source 3FGL J1626.2−4911. A dedicated *XMM-Newton* observation did not reveal any compelling X-ray counterpart either (Eger et al. 2011).
4. HESS J1702−420 is near the point-like source 2FHL J1703.4−4145. The elongation of the VHE γ-ray emission prevented the automated procedure from making the association, but a connection between the objects seems plausible. The small size SNR G344.7−0.1 (about 8′ in diameter) is also in the vicinity and in good positional coincidence with the (point-like) 2FHL source.
5. HESS J1708−410 has no compelling association, even though this source was the target of dedicated X-ray observations to look for associated emission (Van Etten et al. 2009). Given the brightness and relatively steep spectrum of this VHE source ($\Gamma = 2.57 \pm 0.09$), the absence of a counterpart at lower γ-ray energies in the *Fermi*-LAT catalogs is surprising and suggests the emission peaks in the hundreds of GeV range.
6. HESS J1729−345 is north of the nearby SNR HESS J1731−347 (H.E.S.S. Collaboration 2011a). An investigation into a potential connection between the two suggests the VHE emission from the former could be from a molecular cloud illuminated by hadronic particles that escaped from the SNR (Cui et al. 2016).
7. HESS J1741−302 is the subject of a dedicated companion paper (H.E.S.S. Collaboration 2018k) discussing potential PWNe and SNR-related association scenarios, among others. These aspects are therefore not discussed here.
8. HESS J1745−303 is close to, but offset from, SNR G359.1−0.5. *Suzaku* observations have revealed neutral iron line emission in the region, suggesting the presence of molecular matter and making this object another possible case of a CR-illuminated cloud (Bamba et al. 2009). We find this object also to be associated with the HE γ-ray sources 2FHL J1745.1−3035 and 3FGL J1745.1−3011.

9. HESS J1828−099 is a new HGPS source described in Sect. 5.6.8.
10. HESS J1832−085 is also a new HGPS source, described in Sect. 5.6.9.
11. HESS J1858+020 has an association with the HE γ-ray source 3FGL J1857.9+0210 and is close to, but offset from, SNR G35.6−0.4. A dedicated study (Paredes et al. 2014) did not find any compelling X-ray counterpart, although multiple possible scenarios were investigated, including CR-illuminated molecular clouds.

5.1.3. Firmly identified HGPS sources

In this section, we go one step further and treat those HGPS sources for which the physical origin of the VHE γ-ray emission has been firmly identified. Whereas the association criteria were principally based on positional evidence (angular offset), we also perform a census of the additional evidence that is available to reinforce spatial associations and arrive at firm identifications. The supplementary observables we consider are correlated MWL variability, matching MWL morphology, and energy-dependent γ-ray morphology (Hinton & Hofmann 2009). Table 3 summarizes the results, along with the respective references for the additional evidence. Among the 78 sources in the HGPS region, we determine 31 to be firmly identified.

Firm identifications rely on different forms of evidence that vary depending on the source class. The VHE γ-ray emission from compact binary systems is always point-like and should exhibit variability that is also seen at lower energies. In contrast, the VHE emission from shell-type SNRs is extended (provided the SNR is sufficiently large and close) and nonvariable, but can be identified based on the specific shell morphology and correlated morphology at lower energies.

Composite SNRs have both a shell and an interior PWN detected at lower energies and can be more complex to identify correctly. If the angular size of the shell emission is larger than the size of the VHE emission, we can identify the VHE emission as coming from the PWN filling the SNR. This is the case, for example, for HESS J1747−281 (PWN in SNR G0.9+0.1) and HESS J1554−550 (PWN in SNR G327.1−1.1). In other cases, we are only able to identify the HGPS source with the composite SNR as a whole, i.e., we are confident that the VHE emission originates in the composite object but cannot disentangle whether it comes predominantly from the PWN or the shell (usually due to PSF limitations).

More evolved stellar remnant systems are difficult to identify firmly. We can make a firm PWN identification when there is a PWN of comparable size and compatible position detected at lower energies. This is the case, for example, for HESS J1420−607 (PWN G313.54+0.23) and HESS J1356−645 (PWN G309.92−2.51). In the absence of any clear PWN, or when its size at lower energies is much smaller than the VHE source, we have to rely on other evidence. The clearest such evidence is the detection of energy-dependent morphology, expected in PWNe because of the cooling of energetic electrons as they are transported away from the pulsar. At higher energies, the extent of the emission shrinks and its barycenter moves closer to the pulsar. This is the case for two sources thus far, HESS J1303−631 (PWN G304.10−0.24) and HESS J1825−137 (PWN G18.00−0.69). In the absence of such evidence, the identification of a VHE source as a PWN remains tentative when the only evidence is an energetic pulsar in the vicinity. Candidate PWN identifications are evaluated in detail in a companion paper (H.E.S.S. Collaboration 2018e).

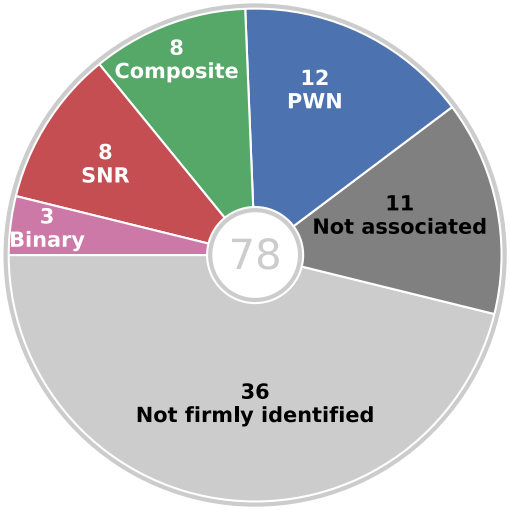

Fig. 10. Source identification summary pie chart. See Table 3 and Sect. 5.1.3.

A large percentage (39%) of the 31 firmly identified sources are PWNe. The next largest source classes identified are SNR shells (26%) and composite SNRs (26%). Finally, γ-ray binary systems are also identified in the HGPS. It is not yet possible to identify firmly more than half of the total 78 HGPS sources with the conservative criteria we adopted, although the vast majority have one or more promising spatial associations that could prove to be real identifications following more in-depth studies beyond the scope of this work. We do not find any physical associations for 11 of the VHE sources in the HGPS, although for some of these, potentially related emission is seen in HE γ-rays, and for others, offset counterparts are present but simply not found by the automated association procedure adopted (see previous section). Figure 10 summarizes these identifications.

We note that one source in HGPS, HESS J1943+213, is likely an extragalactic object. It has no measured extension and a radio counterpart that many recent studies tend to classify as a BL-Lac object (Peter et al. 2014; Straal et al. 2016; Akiyama et al. 2016). However, its VHE flux has not revealed any variability so far, which is unusual for such an object (Shahinyan & VERITAS Collaboration 2017).

5.2. Large-scale emission

In Sect. 4.6, we introduced an empirical spatial model to account for the large-scale VHE γ-ray emission we observed along the Galactic plane to detect and characterize accurately the discrete VHE γ-ray sources. This model provides an estimate of the spatial distribution of the large-scale VHE emission discovered by Abramowski et al. (2014a). We find that the fit amplitude, latitudinal width, and position of this model, shown on Fig. 6, are consistent with the latitude profile of that previous work. The width is also comparable to the HGPS source latitude distribution (Fig. 11, ff.) but smaller than that of molecular gas traced by CO emission (Dame et al. 2001).

Owing to the observational constraints and analysis used, the large-scale emission model cannot be considered a measurement of the total Galactic diffuse emission. The large-scale emission

Table 3. Table of 31 firmly-identified objects among the HGPS sources.

Source name	Identified object	Class	Evidence	Reference
HESS J1018−589 A	1FGL J1018.6−5856	Binary	Variability	H.E.S.S. Collaboration (2015c)
HESS J1302−638	PSR B1259−63	Binary	Variability	Aharonian et al. (2005c)
HESS J1826−148	LS 5039	Binary	Variability	Aharonian et al. (2006c)
HESS J0852−463	Vela Junior	SNR	Morphology	Aharonian et al. (2005e)
HESS J1442−624	RCW 86	SNR	Morphology	H.E.S.S. Collaboration (2018i)
HESS J1534−571	G323.7−1.0	SNR	Morphology	H.E.S.S. Collaboration (2018j)
HESS J1713−397	RX J1713.7−3946	SNR	Morphology	Aharonian et al. (2004b)
HESS J1718−374	G349.7+0.2	SNR	Position	H.E.S.S. Collaboration (2015a)
HESS J1731−347	G353.6−0.7	SNR	Morphology	H.E.S.S. Collaboration (2011a)
HESS J1801−233	W 28	SNR	Position	Aharonian et al. (2008d)
HESS J1911+090	W 49B	SNR	Position	H.E.S.S. Collaboration (2018d)
HESS J0835−455	Vela X	PWN	Morphology	Aharonian et al. (2006d)
HESS J1303−631	G304.10−0.24	PWN	ED Morph.	H.E.S.S. Collaboration (2012)
HESS J1356−645	G309.92−2.51	PWN	Position	H.E.S.S. Collaboration (2011b)
HESS J1418−609	G313.32+0.13	PWN	Position	Aharonian et al. (2006e)
HESS J1420−607	G313.54+0.23	PWN	Position	Aharonian et al. (2006e)
HESS J1514−591	MSH 15−52	PWN	Morphology	Aharonian et al. (2005d)
HESS J1554−550	G327.15−1.04	PWN	Morphology	Sect. 5.6.5
HESS J1747−281	G0.87+0.08	PWN	Morphology	Aharonian et al. (2005b)
HESS J1818−154	G15.4+0.1	PWN	Morphology	H.E.S.S. Collaboration (2014b)
HESS J1825−137	G18.00−0.69	PWN	ED Morph.	Aharonian et al. (2006f)
HESS J1837−069	G25.24−0.19	PWN	Morphology	Marandon et al. (2008)
HESS J1849−000	G32.64+0.53	PWN	Position	Sect. 5.6.15
HESS J1119−614	G292.2−0.5	Composite	Position	Sect. 5.6.1
HESS J1640−465	G338.3−0.0	Composite	Position	Abramowski et al. (2014b), Gotthelf et al. (2014)
HESS J1714−385	CTB 37A	Composite	Position	Aharonian et al. (2008b)
HESS J1813−178	G12.8−0.0	Composite	Position	Funk et al. (2007), Gotthelf & Halpern (2009)
HESS J1833−105	G21.5−0.9	Composite	Position	Sect. 5.6.10
HESS J1834−087	W 41	Composite	Morphology	H.E.S.S. Collaboration (2015d)
HESS J1846−029	G29.7−0.3	Composite	Position	Sect. 5.6.13
HESS J1930+188	G54.1+0.3	Composite	Position	Acciari et al. (2010), Sect. 5.4

Notes. The object classes are γ-ray binary, shell-type supernova remnant (SNR), pulsar wind nebula (PWN), and composite SNR (in cases where it is not possible to distinguish between the shell and interior nebula). The evidence used to identify the VHE γ-ray emission include position, morphology, variability, and energy-dependent morphology (ED Morph.).

model provides an estimate of the diffuse emission present in the HGPS maps. Its parameter values depend on the map construction technique, in particular the exclusion region mask used in the analysis (Sect. 3.2.2), i.e., changes in the mask can alter the parameters of the model. For instance, the peak observed at $\ell \sim 340°$ in Fig. 6 is due to the presence of low-level emission that is just below the threshold to be covered by the exclusion mask we use for the HGPS. While a significant percentage of the large-scale emission is expected to be truly interstellar diffuse emission, it is very likely that emission from discrete but unresolved sources contributes as well. Finally, some features in the HGPS large-scale emission model are likely artifacts of errors in the estimation of the background model of gamma-like cosmic ray EAS events (see Sect. 3.2); these events are the dominating model component in the HGPS counts maps, thus small relative errors in that background model can lead to significant changes in the excess model of the HGPS sources, but even more so the HGPS large-scale emission model.

5.3. Source parameter distributions

In the following section we study the global properties of the VHE γ-ray sources in the HGPS catalog. We compare certain key source parameters against each other and briefly discuss the implications in the context of the Galactic VHE source population, survey sensitivity, and firmly identified MWL source classes.

The latitude distribution of the 78 HGPS sources is shown in Fig. 11. The distribution has a mean of $b = -0.41°$ and a width of 0.87°. For visual comparison, the latitude distributions of the main classes of associated counterparts (Sect. 5.1) – SNRs, energetic pulsars, 3FGL sources, and 2FHL sources – are shown in this figure. Also shown for reference is an estimate of the matter density profile as traced by *Planck* measurements of CO(1-0) line emission (Planck Collaboration X 2016). It should be kept in mind throughout this section that the HGPS sensitivity is not uniform as a function of longitude or latitude (Sect. 3.4.4).

The HGPS latitude distribution of sources correlates well with both potential counterparts and tracers of matter density. The distribution is somewhat skewed toward negative latitudes even though the HGPS sensitivity has a relatively wide and flat coverage in latitude. In Fig. 11, the sensitivity is illustrated by two curves showing regions of relatively good sensitivity (e.g., at $\ell = 0°$) and relatively poor sensitivity (e.g., at $\ell = 333°$). These curves demonstrate that the HGPS sensitivity coverage in latitude is, in general, much wider than the HGPS source

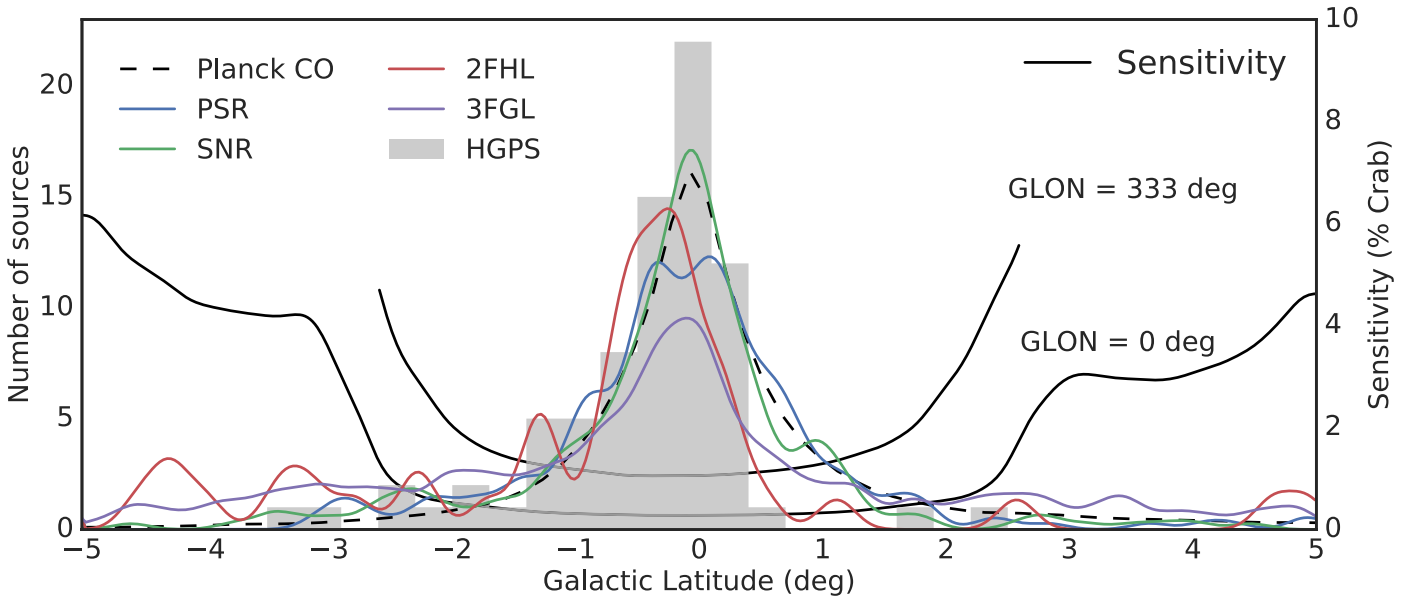

Fig. 11. Galactic latitude distribution of the HGPS sources (gray histogram). The bin size of this histogram is 0.3°. The HGPS point source sensitivity is shown (in units of % Crab) at two different longitudes of 0° and 333°. For comparison, the PSR, SNR, 3FGL and 2FHL source distributions in the HGPS longitude range are shown as overlaid curves, smoothed with Gaussians of width 0.15°. The dashed line shows *Planck* measurements of CO(1-0) line emission as an estimate for matter density in the Galaxy and similarly smoothed. All curves are normalized to the area of the histogram.

distribution. Although there are local exceptions at some longitudes, the latitude coverage is generally flat in the range $-2.0° < b < 1.5°$, at various locations even in $-2.5° < b < 2.5°$. However, the counterpart catalogs are known to suffer from various selection biases and the Galactic disk itself is known to not be perfectly symmetric as observed across the spectrum.

In addition, one might still argue that, given the narrow range of latitudes observed with respect to surveys at other wavelengths, the HGPS sources may not be representative of the underlying distribution of VHE γ-ray sources. However, in light of the counterpart distributions, in particular the 2FHL sources, it can be reasonably assumed that the limited latitude coverage only has a weak effect on the observed source population distribution.

The longitude distribution of the 78 HGPS sources is shown in Fig. 12, together with the molecular interstellar matter column density profile as traced by CO(1-0) line emission (same as in the previous figure). The latter, measured by *Planck* (Planck Collaboration X 2016), has a uniform exposure (sensitivity) over the sky, unlike the HGPS, adding caveats to potential detailed correlations seen in this figure. We can nevertheless robustly conclude that there is a very general correlation in longitude between the number of HGPS sources and the molecular matter column density and that the HGPS sources are mostly found in the inner ∼60° of the Galaxy. Additionally, the spiral arm tangents as traced by CO (Vallée 2014) are shown in Fig. 12. An increased number of sources could be expected in the directions of the near spiral arm tangents (see Fig. 16). In the longitude distribution, a slight excess of sources in the direction of *Scutum* and between *Norma* and *Crux-Centaurus* can be observed. However, because of the limited sample size of 1–6 sources per bin, no significant increased source density in the direction of spiral arm tangents can be observed.

For comparison, we also added distributions for the Fermi-LAT catalogs 3FGL and 2FHL to Fig. 12. While Fermi-LAT has a roughly uniform exposure, their sensitivity in the HGPS region is reduced in the inner Galaxy where diffuse emission is brighter, and also the source extraction is very different from the HGPS approach, so that a direct comparison is not possible. Finally we have chosen not to show the SNR and pulsar distributions in the Galactic longitude distribution at all because the coverage of those catalogs is not uniform.

We compare the HGPS source integral fluxes ($E > 1$ TeV) to source sizes in panel A of Fig. 13 and show the distributions of fluxes and sizes separately in panels B and C, respectively. In the flux–size figure, we plot the approximate flux sensitivity limit of the HGPS as a function of source size. One can see that the sensitivity worsens as the source size increases, as expressed by Eq. (28). The HGPS sources indeed generally follow this trend. From Fig. 13, we therefore conclude that the HGPS can be considered complete down to ∼10% Crab for sources <0.7°. For smaller sources (<0.1°), the HGPS achieves completeness at a few % Crab (see also Fig. 4).

We show the distribution of HGPS source integral fluxes ($E > 1$ TeV), which are calculated assuming a spectral index of $\Gamma = 2.3$, in panel B of Fig. 13. At higher fluxes, we naturally expect the number of sources to decrease. At the lowest fluxes, we also expect the number to be small, because we reached the sensitivity limit of the HGPS.

As can be seen in panel C of Fig. 13 and despite the modest H.E.S.S. PSF (0.08°), the majority of sources are not compatible with being point-like but rather found to be significantly extended and as large as 1°. Owing to the methods used for background subtraction (see Sect. 3.2.3), the HGPS is not sensitive to sources with larger sizes.

The firmly identified HGPS sources (Sect. 5.1) are highlighted in Fig. 13. It can be seen that all identified binary systems appear as point-like sources in the HGPS, as expected. The PWNe appear to have various angular sizes, in agreement with the diversity observed in the VHE PWN population (H.E.S.S. Collaboration 2018e). Most identified SNRs are

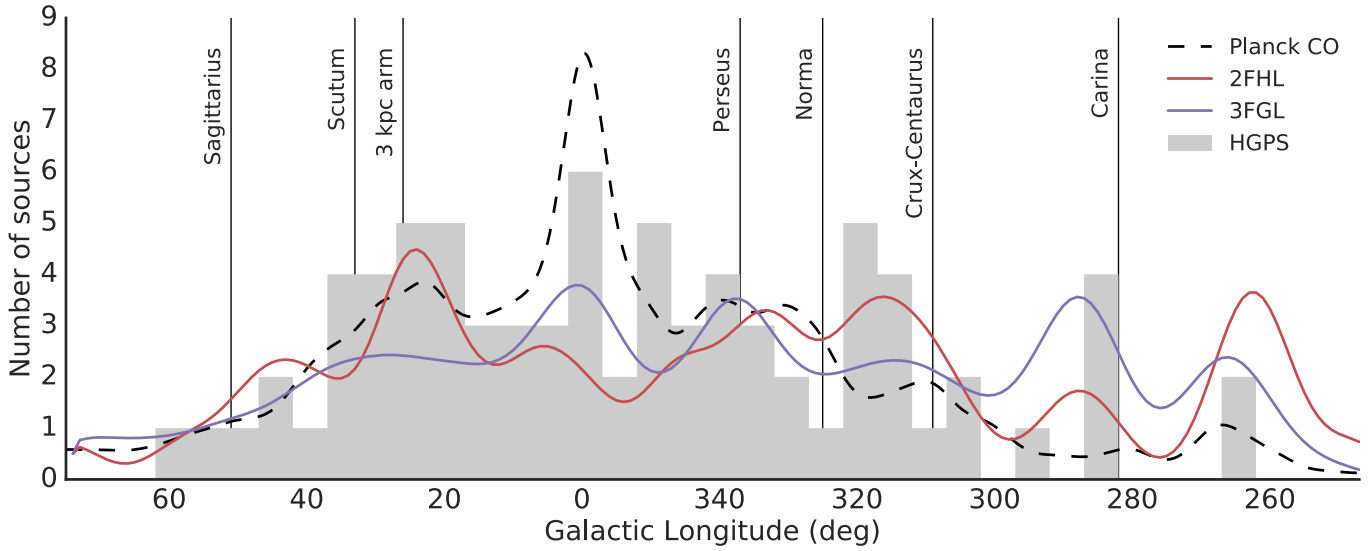

Fig. 12. Galactic longitude distribution of the HGPS sources (gray histogram). The bin size of this histogram is 5°. For comparison, the 3FGL and 2FHL source distributions (smoothed with a Gaussian of width 5°) and the *Planck* measurements of CO(1-0) line emission as an estimate for matter density in the Galaxy (smoothed with a Gaussian of width 2.5°) are shown for the range in Galactic latitude $b \leq 5°$ and normalized to the area of the histogram. Spiral arm tangent locations shown are from Vallée (2014).

extended, likely owing to selection bias (smaller SNRs are difficult to identify, e.g., through shell-like morphology) and the H.E.S.S. PSF. The identified composite SNRs, on the other hand, are typically smaller, owing to the difficulty in disentagling VHE emission from the SNR shell and interior PWN, similarly related to the H.E.S.S. PSF. In any case, it does not seem possible to identify the nature of the many unidentified sources solely on the basis of their sizes or a flux–size comparison.

Figure 14 shows the distribution of the HGPS source power-law (PL) spectral indices Γ. For consistency, the PL model spectral index is used for all sources, even those for which an exponential cutoff power law (ECPL) fits better. The index distribution has a mean $\Gamma = 2.4 \pm 0.3$. This is compatible with the index ($\Gamma = 2.3$) adopted in the production of the HGPS flux maps (Sect. 3.4.2) and the HGPS PSF computation (Sect. 4.3). We note that individual source indices have typical statistical uncertainties of order ±0.2 and a similar systematic uncertainty; HGPS data are often not sufficient to precisely constrain the index because the energy range covered with good statistical precision is typically only about one decade ($1 \lesssim E \lesssim 10$ TeV). Finally, the figure also shows how the firmly identified HGPS sources are distributed in index, showing no strong tendency with respect to source class.

We show the cumulative $\log N(>S) - \log S$ distribution of HGPS source integral fluxes ($E > 1$ TeV, obtained from the maps) in Fig. 15. The 78 HGPS sources span a range in flux from 0.6% Crab to 103% Crab; 32 sources are above 10% Crab. We performed an unbinned likelihood fit of a PL model to the $\log N - \log S$ distribution (also shown in Fig. 15), using only the range $S > 10\%$ Crab where we consider the HGPS survey mostly complete. The best-fit value of the PL slope is -1.3 ± 0.2 (for the cumulative distribution), and the amplitude corresponds to 32 ± 5 sources above 10% Crab. This slope is consistent with Galactic models in which equal-luminosity sources are homogeneously distributed in a thin disk, which have a predicted slope of −1 [8].

The only robust statement that can be inferred from the $\log N - \log S$ distribution of HGPS sources is that it provides a lower limit on the true $\log N - \log S$ distribution; that is, there are at least, for example, 70 sources above 1% Crab. If one assumes that $\log N - \log S$ distributions are always concave (which most "reasonable" spatial distributions and source luminosity functions encountered in the literature are), then the extrapolation of the PL fit shown in Fig. 15 sets an upper limit of ∼600 sources above 1% Crab, with a statistical error of a factor of 2.

More detailed analyses of the $\log N - \log S$ distribution or of the flux-size distribution are possible in principle but in practice do not yield robust results because of the limited number of sources and the large uncertainties concerning the effective sensitivity achieved. We emphasize that the catalog creation procedure is complex (special treatment of known shell-type sources, large-scale emission model component, 15 discarded and several merged components; see Sect. 4.9), with the net effect that the sensitivities shown in Fig. 4 and panel A of Fig. 13 are not reliably achieved, because those sensitivity estimates assume isolated sources, there is no underlying large-scale emission or source confusion, and there is a detection threshold of 5σ, whereas the component detection threshold of TS = 30 corresponds to $\sim 5.5\sigma$.

A representation of the Galaxy seen face-on is depicted in Fig. 16 to visualize how much of the Galaxy the HGPS has been able to probe at different sensitivity levels. Two limits are shown, illustrating the sensitivity detection limit (horizon) of the HGPS for potential point-like sources with presumed luminosity of 10^{33} and 10^{34} erg s^{-1}. Given the achieved sensitivity in the Galactic plane, it is clear that H.E.S.S. has only probed a small fraction of the Galaxy – just up to a median distance of 7.3 kpc for bright (10^{34} erg s^{-1}) point-like sources (and less for extended sources). Furthermore, this illustrative look at survey completeness strengthens the hypothesis that the large-scale emission described in Sect. 4.6 could be partly explained by a population of unresolved sources, presumed to be distant.

[8] The flux S of a source scales with the distance d like $S \propto L/d^2$, where L is the intrinsic luminosity of the source. For a thin disk, we have $N(>S) \propto d^2 \propto L/S$, which corresponds to a slope of −1.0 in the cumulative $\log N - \log S$ distribution.

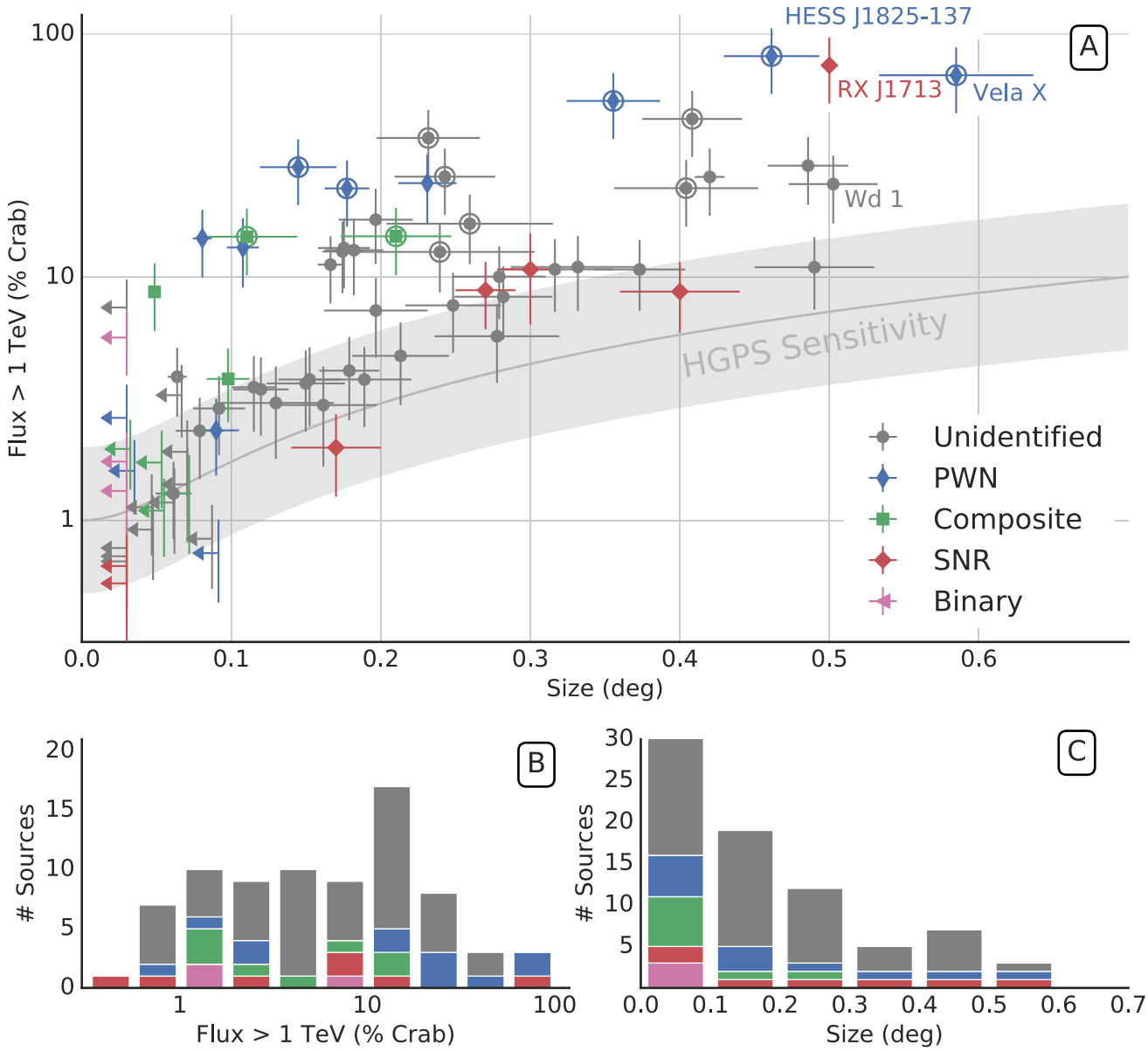

Fig. 13. *Panel A:* integral source flux ($E > 1$ TeV) vs. source size scatter plot with colors representing the different classes of firmly identified sources. For HGPS sources modeled as single Gaussians, the size is its width (σ). For sources modeled as multiple Gaussians (indicated with a circle around the marker), the size is the RMS of the two-dimensional intensity distribution (see Eq. (16)). For sources with shell-like morphology (SNRs), the size is the outer shell radius. To improve the visibility of the plot, we do not show the SNR Vela Junior (HESS J0852−463) at a size of 1° and a flux of 103% Crab. We illustrate the approximate sensitivity limit of the HGPS, as defined in Eq. (28), with an assumed point-source sensitivity of 1% Crab and an uncertainty band with a factor ±2 to represent the sensitivity variations in the survey region (see caveats in main text). *Panel B:* distribution of the integral fluxes ($E > 1$ TeV)of the HGPS sources; colors are shown as in *panel A*. *Panel C:* distribution of the HGPS source sizes; colors shown as in panel A. The first bin contains 30 sources, of which 17 are compatible with point-like sources according to Eq. (18). As in *panel A*, we omit Vela Junior, at a size of 1°.

5.4. Comparison with previous VHE publications

In total, we reanalyzed 48 VHE γ-ray sources that have been the subject of past H.E.S.S. publications. In this section we present a systematic comparison of the present HGPS results, with the latest published results, as summarized in *gamma-cat*[9], the open TeV source catalog.

We associated HGPS sources with previous analyses simply by the name of the source, which was unique except for three cases: HESS J1800−240, HESS J1746−308, and HESS J1930+188, which we discuss in detail in Sect. 5.4.2. We excluded these sources from the systematic comparison in the first place.

To further identify the cases for which we obtained significantly different results from previously published analyses, we compared the position, size, spectral index, and flux of the remaining uniquely associated sources, taking statistical and systematic errors of the measurements into account. For each of these parameters, we estimated the total uncertainty $\sigma_{\rm tot}$ as the 1σ statistical and systematic uncertainties added in quadrature. We estimated this quantity for both the HGPS-derived source parameters and previously published H.E.S.S. values.

[9] https://github.com/gammapy/gamma-cat, accessed July 24, 2017.

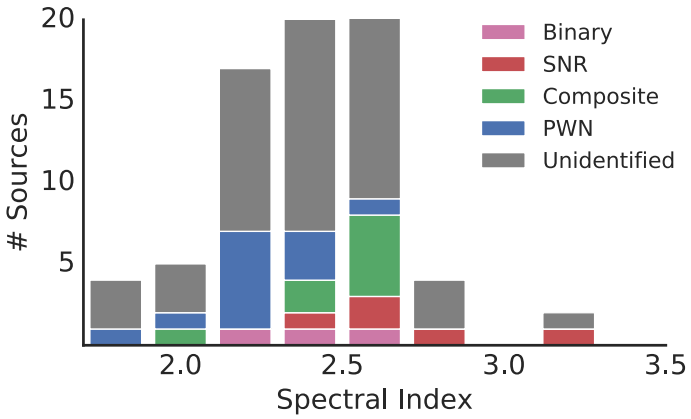

Fig. 14. Distribution of the HGPS source power-law (PL) spectral indices. For consistency, the PL model spectral index is used for all sources, even those for which an exponential cutoff power law (ECPL) fits better. Taking statistical and systematic uncertainties into account, all indices are compatible within 2σ with the mean $\Gamma = 2.4 \pm 0.3$ of the distribution.

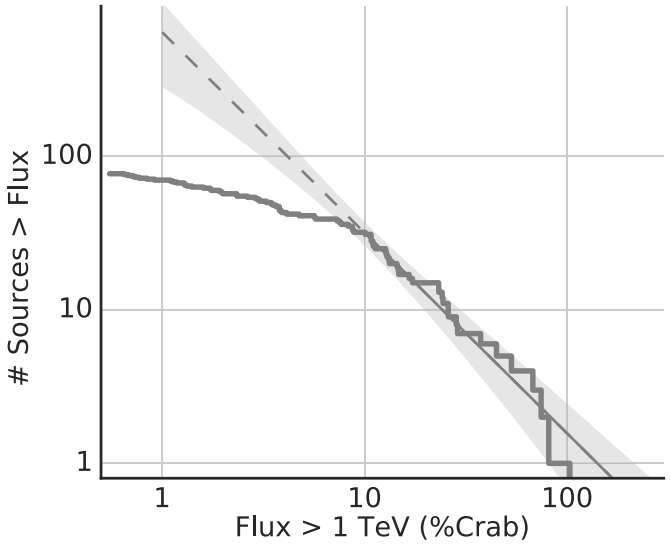

Fig. 15. Cumulative $\log N(>S) - \log S$ distribution for the HGPS sources, showing the number of sources N above given flux thresholds S (integral flux above 1 TeV in % Crab). The line and error band show the result of an unbinned PL fit above a flux threshold of 10% Crab; the dashed line in the 1–10% Crab flux range illustrates the extension of the PL to fluxes below 10% Crab (for comparison, not fitted in that range).

The systematic uncertainties on position and size are given in Sects. 4.10.2, and 4.10.3 respectively. Additionally, we assumed a systematic uncertainty $\Delta\Gamma_{\rm syst} = 0.2$ on the spectral index and 30% on the flux of the source, in agreement with previous estimates (Aharonian et al. 2006b). We then defined the criterion for significant outliers as

$$\Delta_{\rm HGPS-H.E.S.S.} > 2\sqrt{\sigma^2_{\rm tot,HGPS} + \sigma^2_{\rm tot,H.E.S.S.}}, \quad (29)$$

where $\Delta_{\rm HGPS-H.E.S.S.}$ is the difference between the corresponding parameter values. When comparing the position we chose the angular separation as comparison parameter. We note that for many sources, the data sample used here is significantly different from that used in the publication, hence the correlation of statistical errors is usually not too large.

We first discuss the general level of agreement between the current and previous analyses (excluding the outliers) in Sect. 5.4.1 and later discuss the outliers of the comparison individually in Sect. 5.4.2.

5.4.1. Agreement with previous publications

For the vast majority of sources, we find that there is good agreement between the HGPS-derived position, morphology, and spectrum within the statistical and systematic uncertainties.

Position. We found the position of 43 (out of 45) sources to be compatible with the previously published value, according to Eq. (29). For point-like sources we found an average shift of 0.02 ± 0.01 deg, while for extended sources the value was 0.06 ± 0.05 deg. Both values agree well with the expected scatter considering the statistical and systematic uncertainties on the measurements. As an additional check, we also verified that the positions of the identified γ-ray binaries (known point sources) HESS J1826−148 and HESS J1302−638 are in good agreement (within 40″) with the reference positions of the corresponding objects LS 5039 and PSR B1259−63 as listed in SIMBAD[10].

Size. Comparing the sizes of the extended sources we found 30 (out of 35) sources to be compatible with the previously published value. The average size difference for the extended sources was on the order of ∼18%, the distribution of values having a width of ∼40%. This indicates that with the current analysis we measured slightly larger sizes of the sources on average, but the distribution is dominated by a large scatter. We expect the scatter to result mainly from differences in the analysis procedure. Previous analyses mainly fitted single Gaussian morphologies, while in this analysis we allowed for multiple Gaussian components. Further differences are the addition of the large-scale emission model and the systematic modeling of emission from neighboring sources.

Previous publications found seven sources to be compatible with a point-like source. In the current analysis we found all these sources to be compatible with a point-like source again. Additionally, we identified the following three cases that are compatible with a point-like source according to Eq. (18), which were previously found to be extended:

1. For HESS J1427−608 we measured a size of $0.048 \pm 0.009°$, compared to $0.063 \pm 0.010°$ in Aharonian et al. (2008a). This source is a borderline case that just meets our criterion for a point-like source.
2. For HESS J1714−385 we found a size of $0.034 \pm 0.011°$ compared to $0.067 \pm 0.017°$ in Aharonian et al. (2008b). With the current analysis, a smaller size was found because underlying emission was modeled by separate emission components (see Fig. 5).
3. We now measure the size of HESS J1808−204 to be $0.058 \pm 0.014°$ (consistent with point-like, in the definition of Eq. (18)), compared to the previously measured size $0.095 \pm 0.015°$ (extended) (H.E.S.S. Collaboration 2018a). This discrepancy is due to the HGPS's inclusion of a large-scale emission component that now models γ-ray excess previously accounted for in the source component itself.

Flux. We found the flux of 42 (out of 45) sources to be compatible with the previous published value, according to Eq. (29). The average difference in flux for extended sources was 3% with

[10] http://simbad.u-strasbg.fr/simbad

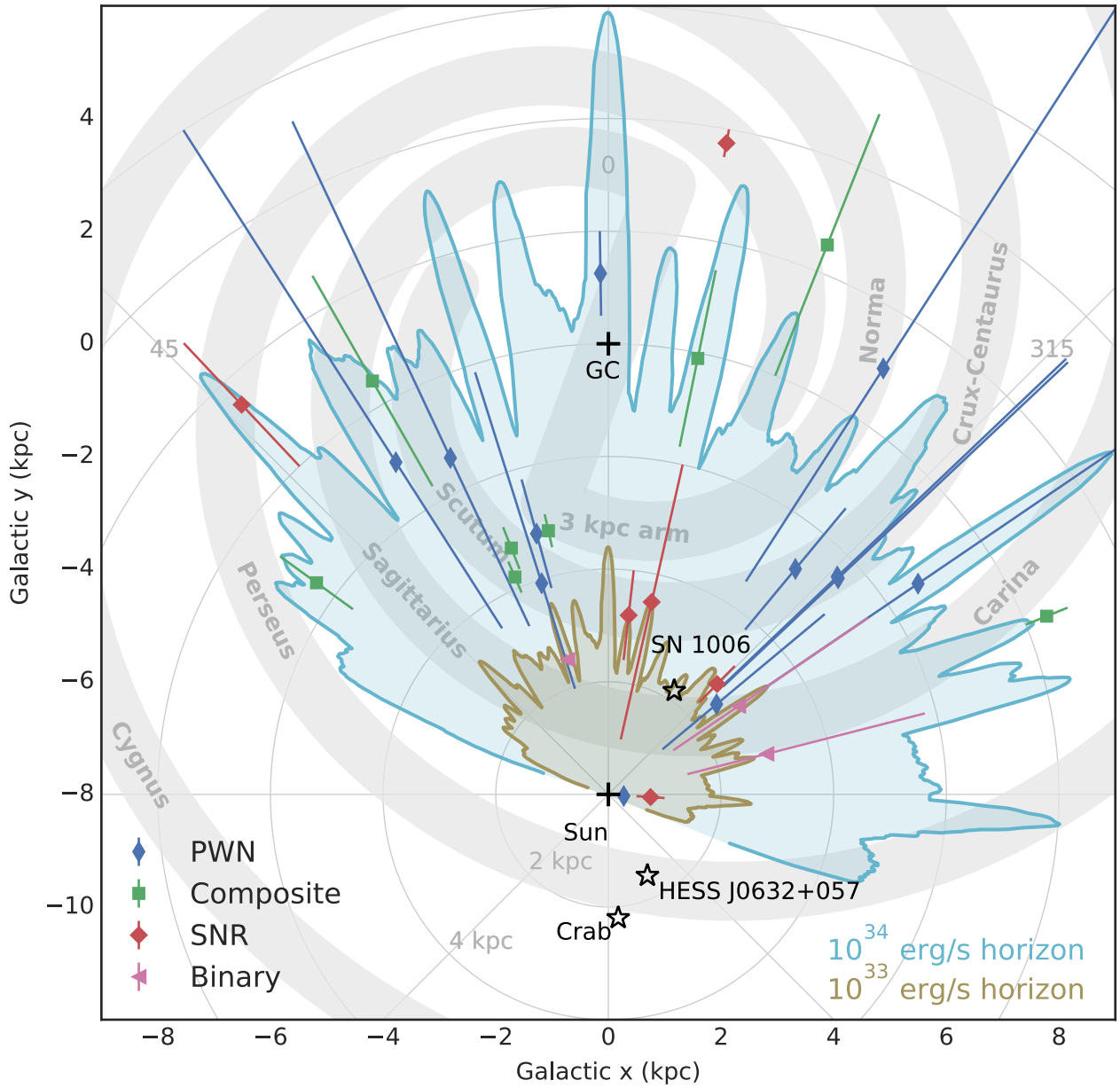

Fig. 16. Illustration of the location of identified H.E.S.S. sources in the Galaxy with respect to HGPS completeness (sensitivity limits). This is a face-on view; the spiral arms (Vallée 2014) are schematically drawn as gray bars. The HGPS horizons for source luminosities of 10^{33} and 10^{34} erg s^{-1} (for a putative 5σ detection of a point-like source, same as Fig. 4) are depicted by light blue and light brown lines (and shaded regions therein), respectively. The source distances are from SNRcat (Ferrand & Safi-Harb 2012) and ATNF pulsar catalog (Manchester et al. 2005). When no distance uncertainties were available, we applied a generic uncertainty of factor two on the distance. The three labeled sources are the Galactic γ-ray sources outside the HGPS region detected by H.E.S.S.

a width of 43% for the distribution of values. While the average value is compatible with previous analyses, we still found a large scatter (albeit compatible to the systematic and statistical errors) of the distribution.

A fair comparison between flux values obtained with the current method and earlier analyses proved to be difficult again because of fundamental differences between the methods used. In previous publications, aperture photometry was mostly used, while in this analysis the main flux measurement was based on a model fit, taking the PSF and morphology of the source and large-scale emission into account. Flux estimate differences with these two methods are shown in Fig. 9 (both measures from the HGPS analysis, not with respect to previous publications). Many of the differences in spectra and fluxes measured in the HGPS analysis and previous publications are the result of changes in the spectral extraction region (position and size).

Spectral index. For all sources we found the spectral power-law indices to be compatible with the previously published values. The mean difference in spectral index was 0.04 with a width of 0.23 for the distribution. This is well compatible with the expected scatter taking statistical and systematic uncertainties of the measured spectral indices into account.

5.4.2. Differences with previous publications

In the following paragraphs, we list and discuss the outliers as identified by Eq. (29).

HESS J0835−455. This source (Vela X) exhibits complex morphology, and the HGPS analysis best models the VHE emission as a superposition of three Gaussian components with an average size 0.58° ± 0.052°. This value is somewhat larger than the value published first in Aharonian et al. (2006d), where it was modeled as a single asymmetric Gaussian of size 0.48° ± 0.03° × 0.36° ± 0.03°. However, a more recent H.E.S.S. publication (Abramowski et al. 2012a) studied the complex emission more thoroughly. It fit profiles of the emission along two perpendicular axes, the main one aligned with the primary orientation of the emission. Along the major axis, the study measured a Gaussian size 0.52° ± 0.02°, and along the minor axis, two Gaussians (sizes 0.12° ± 0.02° and 0.60° ± 0.04°) were required to best fit the emission. The HGPS model of the emission from HESS J0835−455 is thus largely compatible with the most recent dedicated study of the VHE emission, and the apparent discrepancy is simply a result of comparing two different multi-component models with our general outlier criterion (Eq. (29)).

HESS J1646−458. HESS J1646−458 is a complex emission region located in the vicinity of the stellar cluster Westerlund 1. Its morphology suggests it consists of multiple sources. Abramowski et al. (2012b) separated the emission into at least two distinct features (with radii 0.35° and 0.25°, respectively) as well as some structured extended emission, distributed over the signal region of 2.2° diameter, and even extending beyond. A flux above 1 TeV in the signal region of $7.6 \pm 1.3 \pm 1.5 \times 10^{-12}$ cm^{-2} s^{-1} was derived, and a spectral index of $2.19 \pm 0.08 \pm 0.20$. An ON-OFF background estimation technique was used to cope with the large source size. In the HGPS analysis, this complex emission is modeled by a single Gaussian component of 0.5° size shifted by 0.47° from the center of the region used in Abramowski et al. (2012b), with a lower flux above 1 TeV of $5.48 \pm 0.46 \times 10^{-12}$ cm^{-2} s^{-1}, and steeper index of 2.54 ± 0.13. Given the complex morpology and the large scale of the spectral extraction region used in Abramowski et al. (2012b), significant differences in source parameters are to be expected; in the HGPS analysis part of the flux is absorbed in the large-scale diffuse background.

HESS J1708−410. The flux above 1 TeV of HESS J1708−410 is found to be smaller in the HGPS analysis than in Aharonian et al. (2008a). While the size of the source is similar in both cases, the different approaches used in the HGPS analysis lead to different integration radii used to derive the source spectrum. The HGPS analysis uses an integration radius about two times smaller than in the dedicated analysis, which explains the apparent discrepancy.

HESS J1729−345. For HESS J1729−345, the HGPS analysis finds a flux above 1 TeV larger than in H.E.S.S. Collaboration (2011a). Because of the HGPS morphology modeling of the source and its procedure to define the integration radius, the spectrum of this source is derived in a region with a radius about two times larger than in the dedicated publication, accounting for the observed difference.

HESS J1745−303. HESS J1745−303 was studied in Aharonian et al. (2008c) with 80 h of data. Its morphology is complex and three subregions, called A, B, and C, were discussed. In the HGPS analysis, with more than 160 h on the region, two distinct sources are detected: HESS J1745−303 and HESS J1746−308. The former encloses the hotspots A and C and a fraction of region B. A second source is now detected at $b = -1.11°$ latitude. This source contains part of hotspot B and emission at large latitudes that was not significant before, likely due to the additional livetime obtained since 2008. It is fainter and its spectrum is very steep but poorly constrained. There is also a third extended ($\sigma \sim 0.5°$) Gaussian component in the region. It is currently considered to be a diffuse component. The association of the two sources and the extended component is unclear and the exact morphology of the VHE emission in the region will require dedicated studies.

HESS J1800−240. In Aharonian et al. (2008d) the emission in the region of W 28 was found to be split into two components: HESS J1801−233 (addressed below), which is not significant in the HGPS analysis and is coincident with the W 28 SNR itself, and a complex region HESS J1800−240 offset by 0.5° to the south. The latter was previously found to be resolved into three hotspots dubbed HESS J1800−240 A, B, and C (Aharonian et al. 2008d). Since sources HESS J1800−240 A and B are spatially coincident with molecular clouds, Aharonian et al. (2008d) suggested that they were produced by CRs that had escaped the SNR and had illuminated ambient gas clouds, making this system an archetype of CR escape from evolved SNRs (see, e.g., Aharonian, & Atoyan 1996; Slane et al. 2015; Gabici & Montmerle 2015). In the HGPS analysis, however, only one source is redetected, HESS J1800−240, as one large Gaussian component centered on the hotspot B. The separation into several components does not result in a high enough TS to separate it into several significant sources in the analysis shown here.

HESS J1825−137. HESS J1825−137 is a large PWN with a bright core surrounded by extended, asymmetric emission. The HGPS analysis finds it has a size of 0.46° ± 0.03°, using three Gaussian components to model the VHE entire γ-ray emission. This is significantly larger than the 0.24° ± 0.02° obtained with a single symmetric Gaussian model or the 0.23° ± 0.02° × 0.26° ± 0.02° with a single asymmetric Gaussian in Aharonian et al. (2006f). These models were stated to have rather poor χ^2 goodness-of-fit values. The more complex approach taken for the morphology modeling in the HGPS improves the description of the γ-ray emission from this PWN and accounts for the differences with respect to previous, simpler modeling.

HESS J1837−069. The HGPS analysis of HESS J1837−069 finds a size of 0.36° ± 0.03° based on modeling the VHE γ-ray emission as three Gaussian components. This is larger than the size previously derived using a single asymmetric Gaussian (Aharonian et al. 2006a), i.e., 0.12° by 0.05°; and using a single Gaussian (Marandon et al. 2008), i.e., 0.22°. The more complex modeling of the HGPS, which also takes into account more of the extended nebular emission from this identified PWN, explains the apparent discrepancy. Consequently, we used a larger region (twice the radius compared to Aharonian et al. 2006a) to derive the spectrum, leading to an integral flux above 1 TeV that is larger by a factor of ∼3 than in the dedicated publication.

HESS J1857+026. The size of the source HESS J1857+026 is significantly larger in this analysis than previously published in Aharonian et al. (2008a). In the latter, the source is fit with an asymmetric Gaussian (0.11° ± 0.08° × 0.08° ± 0.03°), whereas

the HGPS analysis best models the source with two Gaussian components for an approximate size of 0.26° ± 0.06°. The difference in size is explained by the multicomponent approach of the HGPS that better takes into account the larger scale emission underneath the central bright core.

HESS J1908+063. The position and size published in Aharonian et al. (2009) are significantly different from those obtained in the HGPS analysis. The position is offset by 0.17° and the size is found to be 0.48° ± 0.04°, which is 0.14° larger. We note that the size we find is consistent with that measured by the VERITAS Collaboration (Aliu et al. 2014b), even though the positions differ by 0.3°. A plausible cause for these discrepancies is that this is a large source likely composed of multiple components, where results are expected to be sensitive to the morphology assumptions and to details in background modeling techniques, in particular, if those tend to absorb large-scale features.

HESS J1923+141. The VHE γ-ray source HESS J1923+141 (preliminary H.E.S.S. results published in Fiasson et al. 2009) is spatially coincident with the W 51 region, studied in detail with the MAGIC IACT (Aleksić et al. 2012). The HGPS results are generally compatible with those from MAGIC. However, the latter shows evidence for a γ-ray source composed of two components above 1 TeV, which cannot yet be confirmed by H.E.S.S. One component is coincident with the interaction region between W 51C and W 51B, while the other is coincident with the potential PWN CXOU J192318.5+140305 (Koo et al. 2005), suggesting that HESS J1923+141 may be a composite of VHE emission of different astrophysical origins.

HESS J1930+188. The VHE γ-ray source, discovered with VERITAS (with the identifier VER J1930+188, Acciari et al. 2010), is coincident with the composite SNR G54.1+0.3 and the pulsar PSR J1930+1852. We report on the H.E.S.S. observations of this source for the first time here. The HGPS source is found to have a slightly displaced position from the pulsar and the VERITAS best fit (by 0.04°). Despite the agreement with the VERITAS spectral index, the integral flux above 1 TeV found in our analysis is ∼40% lower than their published flux. We note, however, that the apparent discrepancy with VERITAS is not confirmed by our cross-check analysis, which yields a flux for this source that is larger by more than the nominal 30% systematic flux uncertainty, and is in agreement with the VERITAS measurement.

5.4.3. Sources not redetected

In total, there are four previously published VHE γ-ray sources that are not redetected with the current HGPS analysis. All of these are rather faint sources which, for the HGPS analysis, yield significances close to the HGPS detection threshold of $TS = 30$. We consider these as real sources of γ-rays; the nondetection in the HGPS is primarily a result of differences between the HGPS analysis and specific analysis methods. We found that some of the most relevant differences are

1. event reconstruction and γ-ray-hadron separation cuts that are less sensitive compared to more specialized methods that have been used in individual source analyses;
2. higher energy threshold in the HGPS analysis, in conjunction with a soft spectrum of the tested source;
3. use of the 2° FoV offset cut (see Sect. 3.1), which is tighter than the value used in many previous H.E.S.S. publications (2.5° or even 3°).

In addition, the use of a large-scale emission model and the modeling of nearby extended components and overlapping sources modifies the measured flux and hence the significance of a source compared to previous analyses, where larger scale background features were accounted for in different ways (e.g., partly absorbed in the ring background). Given these differences, it is not surprising that few faint sources fail the HGPS detection criteria.

In the following paragraphs, we describe the individual cases in more detail. For completeness, we added all missing sources to the final HGPS catalog; the source parameters were taken from the corresponding publication (see also Table 1).

HESS J1718−374 and HESS J1911+090. These VHE γ-ray sources (Figs. A.2 and A.3) were previously detected toward the SNR G349.7+0.2 and W 49B/SNR G43.3−0.2, respectively. Both are thought to result from interactions with molecular clouds and exhibit correspondingly steep (soft) spectra, which have PL indices $\Gamma = 2.80 \pm 0.27$ (H.E.S.S. Collaboration 2015a) and 3.14 ± 0.24 (H.E.S.S. Collaboration 2018d), respectively. The energy threshold of the analyses is therefore key to detecting these sources. As described in Sect. 3, the maps that serve as a starting point for the source catalog have been produced using the hard cuts configuration and a conservative safe energy threshold, explaining the lack of detection of these sources in the HGPS analysis.

HESS J1741−302. The unidentified source HESS J1741−302 is located on the Galactic plane ($b = 0.05°$) and ∼1.7° away from the Galactic center. With an integral flux of ∼1% Crab above 1 TeV it is one of the faintest H.E.S.S. sources detected so far (H.E.S.S. Collaboration 2018k). Because of the addition of the large-scale emission model in the HGPS analysis, HESS J1741−302 does not reach the HGPS TS = 30 detection threshold.

HESS J1801−233. This source is part of the HESS J1800−240 and HESS J1801−233 source complex discussed above, characterizing emission features of the SNR W 28 region (Aharonian et al. 2008d). The emission was found to be split into two components: HESS J1801−233, which is coincident with the northeastern boundary of W 28 where the shockwave is interacting with a molecular cloud, and a complex region HESS J1800−240 offset by 0.5° to the south. HESS J1801−233 does not reach the TS = 30 threshold and is therefore not found to be significant in the HGPS analysis. We note that the γ-ray emission from W 28 is bright in the GeV range and is clearly detected above 50 GeV (Ackermann et al. 2016). It has a steep spectral index of 2.7 ± 0.3 at VHE (Aharonian et al. 2008d). It is therefore not detected here because of our higher analysis energy threshold (about 400 GeV at a longitude of 7°, see Fig. 2) and because of the inclusion of the large-scale emission model in our analysis, which reduces the significance of such a faint source. Furthermore, we reiterate that HESS J1800−240 is detected in the HGPS as one large Gaussian source, see Sect. 5.4.2, rather than three individual hotspots as in Aharonian et al. (2008d). This potentially also contributes to a reduction of the significance of this previously established source HESS J1801−233.

5.5. Comparison with the cross-check analysis

For most sources, the spectral fit results reported in this catalog agree with those obtained from the independent cross-check analysis (see Sect. 4.12). For the following sources, however, larger differences, exceeding the systematic errors, are observed. Several factors could explain these differences, such as the lower energy threshold in the cross-check analysis, the differences in the morphology models, or the fact that the cross-check spectrum analysis is run for the positions and sizes obtained with the main analysis.

- HESS J1503−582 (see Sect. 5.6.4): While the spectral indices are compatible, the derived integral flux above 1 TeV is about two times higher in the main analysis than in the cross-check analysis.
- HESS J1646−458 (Westerlund 1): the cross-check analysis gives a spectrum that is about two times brighter around 1 TeV, with a curvature or cutoff leading to similar fluxes as the main analysis at low and high energies. We would like to stress again that the HGPS analysis for this source is not very reliable, because the source size is similar to the H.E.S.S. field of view and a more careful individual study and background estimation is needed, as explained in Sect. 5.4.2 which points out the differences with the previously published measurement.
- HESS J1718−385: For both the main and cross-check analyses, the preferred spectral model is a power law with an exponential cutoff. The cutoff energies are compatible and the spectra are in agreement above ∼3 TeV. However, below this energy, some discrepancy is observed as the main analysis spectral fit yields a spectral index that is harder than in the cross-check analysis, resulting in an integral flux above 1 TeV about two times lower in the main analysis than in the cross-check analysis.
- HESS J1729−345: While the derived spectral indices are compatible, the integral flux above 1 TeV is about two times higher in the cross-check analysis than in the main analysis.
- HESS J1746−308: The large spectral index derived from the main analysis could not be confirmed by the cross-check analysis. The differential flux values at 1 TeV are compatible, but the discrepancy in the obtained spectral indices leads to an integral flux above 1 TeV about two times higher in the cross-check analysis than in the main analysis.
- HESS J1852−000 (see Sect. 5.6.16): The derived spectral indices are compatible, but the integral flux above 1 TeV is about two times higher in the cross-check analysis than in the main analysis.

Spectral model results for these six sources should therefore be treated with caution.

5.6. New VHE sources

During the construction of the HGPS catalog, statistically significant VHE γ-ray emission was detected from 16 sources which were not previously known or for which only preliminary detections had been published (e.g. in conference proceedings). All of these new sources are confirmed by the cross-check analysis – we do not expect any of these new sources to be a false detection (see Sects. 4.8 and 4.9). The morphological and spectral properties of these new, confirmed VHE sources are provided in Tables A.7 and A.8, their spectra are shown in Fig. 17. Each new source is also briefly described in the following sections, in the context of its MWL environment and possible origin of the VHE γ-rays.

5.6.1. HESS J1119−614

We confirm the discovery of VHE γ-ray emission from HESS J1119−614 (Fig. 18) and identify it as the composite SNR G292.2−0.5. We base the firm identification on the basis of spatial coincidence with the SNR and its associated PWN G292.15−0.54 and highly magnetized pulsar PSR J1119−6127. H.E.S.S. previously published (Djannati-Ataï et al. 2009) preliminary source properties that are compatible with the HGPS results.

A compact (size $6'' \times 15''$), nonthermal PWN has been detected in X-rays (Gonzalez & Safi-Harb 2003; Safi-Harb & Kumar 2008) and is considered a candidate PWN in HE γ-rays (Acero et al. 2013). It is powered by the energetic pulsar PSR J1119−6127, with spin-down luminosity $\dot{E} = 2.3 \times 10^{36}$ erg s^{-1} and distance $d = 8.4 \pm 0.4$ kpc (Caswell et al. 2004). The pulsar has been detected in radio (Camilo et al. 2000) and HE γ-rays (Parent et al. 2011; Acero et al. 2015, as 3FGL J1119.1−6127 in the latter) and is characterized by a relatively high surface B-field (4.1×10^{13} G). Despite it being a rotation-powered pulsar, it has recently joined the other high-B pulsar PSR J1846−0258 in revealing a magnetar-like behavior (Göğüş et al. 2016; Younes et al. 2016; Antonopoulou et al. 2016). It is further notable for being among the handful of pulsars for which braking indices have been measured, in this case $n = 2.684 \pm 0.002$ (Weltevrede et al. 2011), as opposed to simply assuming $n = 3$, giving a more precise characteristic age $\tau_c = \frac{P}{(n-1)\dot{P}} = 1.9$ kyr, where P and $\dot{P}$ are the currently measured period and period derivative, respectively.

Considering the luminosity of HESS J1119−614, $L_\gamma(1\text{–}10\,\mathrm{TeV}) = 2.4 \times 10^{34} (d/8.4\,\mathrm{kpc})^2$ erg s^{-1}, the apparent efficiency of converting the pulsar's rotational energy to γ-rays, $\epsilon_{1\text{–}10\,\mathrm{TeV}} \equiv L_\gamma/\dot{E} = 1.1\%$, is compatible with the efficiencies ($\lesssim$10%) of other VHE sources that have been identified as PWNe (Kargaltsev et al. 2013). The offset of the VHE emission from this young pulsar, where the X-ray PWN is located, is not statistically significant with respect to the uncertainty on the best-fit VHE centroid (±0.02°).

The age of SNR G292.2−0.5 is in the range 4.2–7.1 kyr (Kumar et al. 2012). This can be reconciled with the characteristic age of the pulsar if the braking index n was much smaller than the current value until recently. This assumption is reasonable in light of recent evidence for erratic radio timing behavior from the pulsar (Weltevrede et al. 2011). The X-ray emission from the SNR is predominantly thermal and has an additional hard, nonthermal, X-ray component. This nonthermal emission is likely from the PWN, although an origin in the SNR reverse shock could not be ruled out (Kumar et al. 2012).

The X-ray spectral measurements suggest the SNR is generally expanding in a low-density medium, appearing to disfavor a hadronic origin for the VHE γ-rays (Drury et al. 1994). However, there is also evidence for localized, high-density regions near the eastern SNR shell, including dark clouds and CO features (Kumar et al. 2012). We cannot confirm the claim by Kumar et al. (2012), based on preliminary H.E.S.S. results (Djannati-Ataï et al. 2009), that no VHE emission is detected from the eastern SNR shell, as it is well within the VHE emission region in the HGPS analysis.

In conclusion, while the identification with the composite SNR and PWN system is firm, it is not yet clear whether the VHE emission originates in the SNR shock, either leptonically, from the shell itself, or hadronically, from interactions with ambient media; the PWN; or some combination thereof.

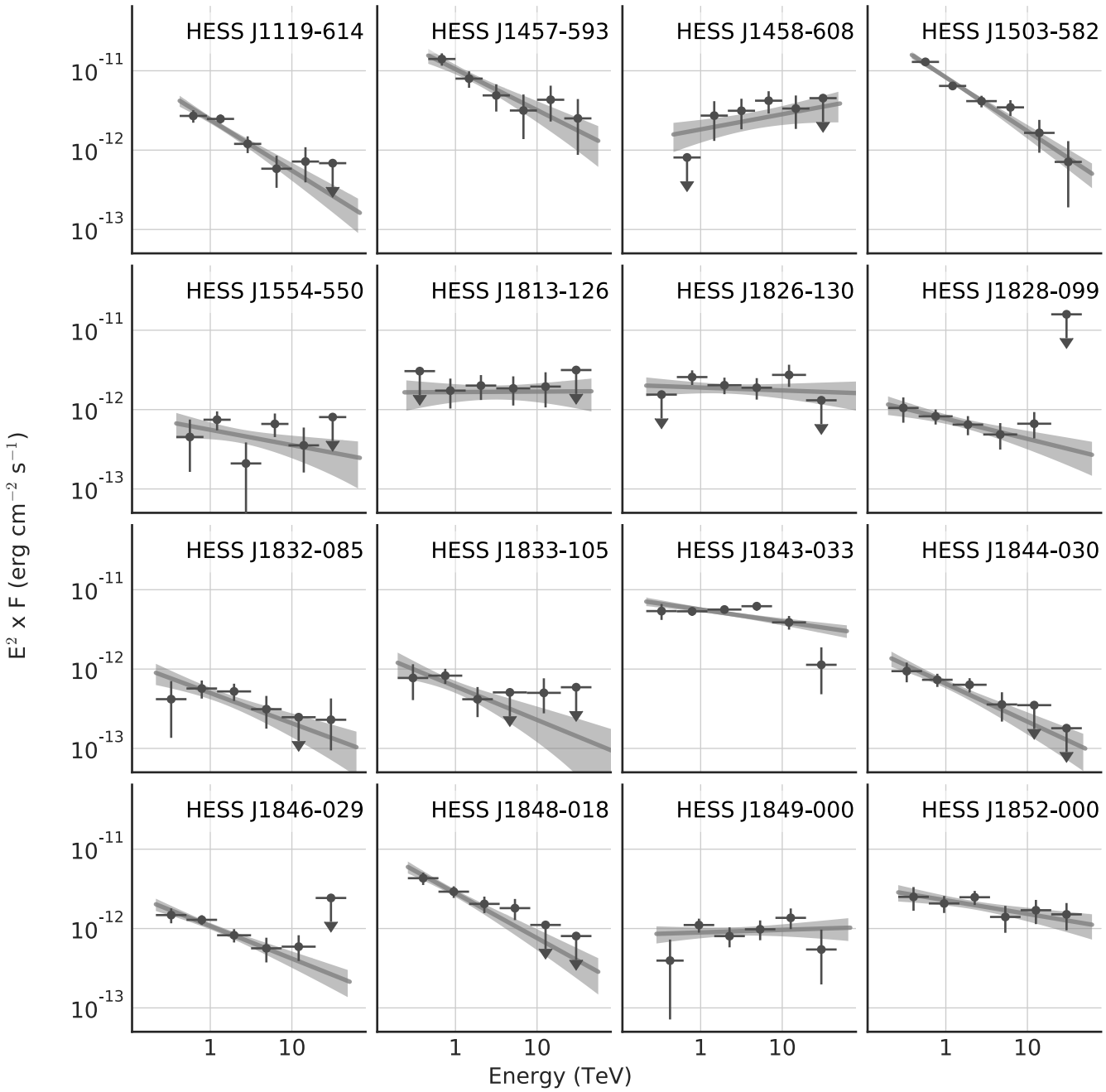

Fig. 17. Fitted power-law spectral models with uncertainty bands and flux points for new sources.

5.6.2. HESS J1457−593

VHE γ-ray emission from the new source HESS J1457−593 (Fig. 19) is associated with the SNR G318.2+0.1, on the basis of a spatial coincidence with a shell-type SNR and lack of other potential MWL counterparts. Preliminary H.E.S.S. morphological properties were initially published by Hofverberg et al. (2010). The HGPS source position is compatible with the preliminary position; however, the size of the source in the catalog is different because of a difference in the assumed morphological model. Previously, the source was modeled as an asymmetric Gaussian ($0.31^\circ \pm 0.07^\circ$ by $0.17^\circ \pm 0.05^\circ$) whereas the HGPS source is modeled, like all HGPS sources, as a symmetric Gaussian ($0.33^\circ \pm 0.04^\circ$). Nonetheless, the spatial overlap between HESS J1457−593 and the southern part of the SNR shell still holds.

G318.2+0.1 is observed as a relatively large ($40' \times 35'$) shell in radio (e.g., Whiteoak & Green 1996), which is characterized by two arc-like, nonthermal filaments in the northwest and southeast (SE) that together form the shell. The VHE emission is much larger than the SNR shell, and the VHE centroid is significantly offset (~0.4°) from the SNR center, although it is partially coincident with the SE rim of the shell. Furthermore, there is evidence in ^{12}CO (Dame et al. 2001) of a giant molecular cloud (GMC) at $(\ell, b) \approx (318.4^\circ, -0.5^\circ)$ coincident with both the VHE emission and the SE rim; this GMC is $1.8^\circ \times 1.1^\circ$ (average physical size 80 pc) in size and has mass $\sim 3{\times}10^5\ M_\odot$ and density $\sim 40\ \mathrm{cm}^{-3}$, assuming the near solution of the kinematic distance 3.5 ± 0.2 kpc (Hofverberg et al. 2010). Little is known about G318.2+0.1 itself, but assuming it is at the same distance as the GMC and further assuming a Sedov-Taylor model for the SNR evolution, its physical diameter would be ~40 pc

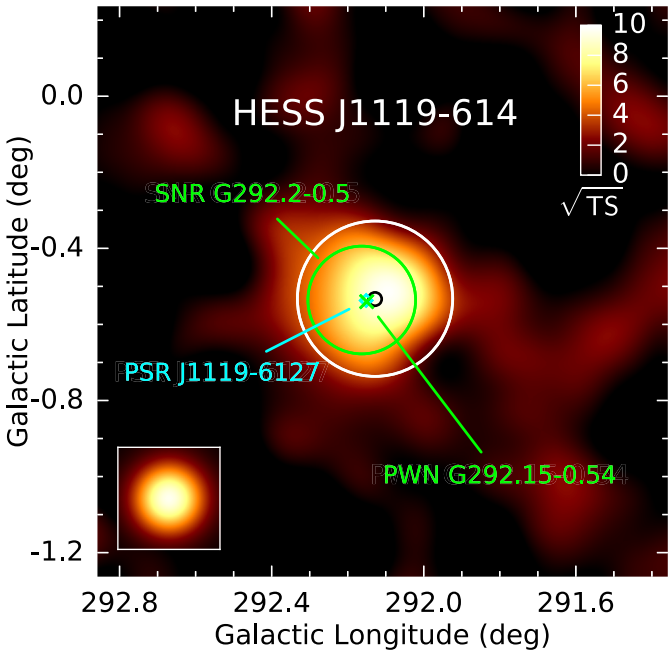

Fig. 18. Significance ($\approx \sqrt{\mathrm{TS}}$) of the VHE γ-ray excess, centered on the new source HESS J1119−614, with the H.E.S.S. The PSF for this data set shown inset. The black circle at the center indicates the 68% uncertainty in the best-fit centroid of the VHE emission. The white circle represents the 70% containment region of the emission (R_SPEC, used also for spectral measurement). The approximate size of the radio shell of SNR G292.2−0.5 is shown as a green circle and the PWN G292.15−0.54 as a green marker. The position of the pulsar PSR J1119−6127 is denoted by a cyan diamond. The FoV is 1.5° × 1.5°.

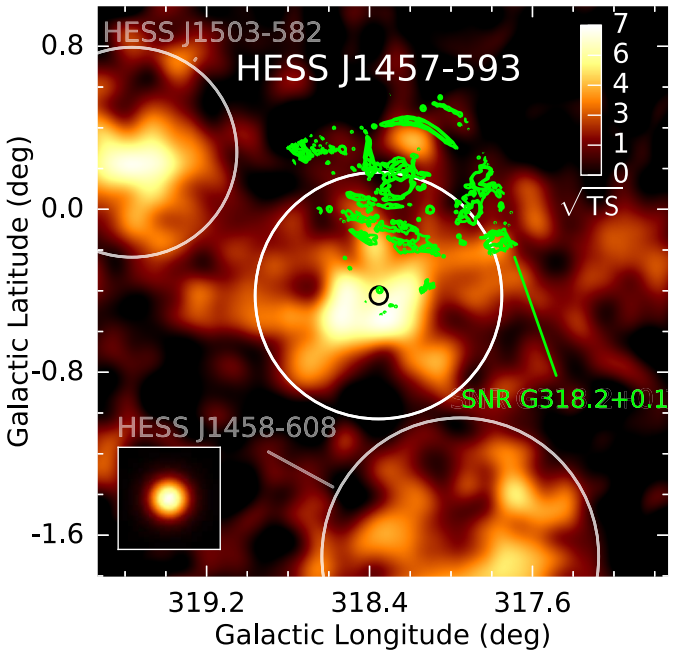

Fig. 19. VHE γ-ray image: HESS J1457−593. See Fig. 18 for a general description. Additionally, the SNR G318.2+0.1 is shown by plotting its 843-MHz radio intensity (Whiteoak & Green 1996) with contours at 4, 8, and 12 mJy beam^{-1}. The FoV is 2.8° × 2.8°.

and its age ∼8 kyr. These data suggest a plausible SNR and molecular cloud interaction scenario (e.g., Gabici et al. 2007), where particles are accelerated in the shell, escape, and interact with a nearby but offset MC, producing γ-rays via hadronic p-p collisions.

An X-ray study of the SNR with *BeppoSAX* and *ROSAT* did not find evidence for shell-like, nonthermal emission, nor thermal X-ray emission that should trace the interaction between the SNR and ISM (Bocchino et al. 2001). However, several hard X-ray sources were found, suggestive of at least localized nonthermal electron acceleration. Additional MWL observations and spectral modeling are required to further investigate the scenario responsible for the production of VHE γ-rays.

5.6.3. HESS J1458−608

VHE γ-ray emission from the new source HESS J1458−608 (Fig. 20) is associated with the pulsar PSR J1459−6053 and can likely be identified as a heretofore undetected PWN, on the basis of a spatial coincidence with an energetic pulsar and the absence of other plausible MWL counterparts. Preliminary VHE morphological and spectral properties were first announced by de los Reyes et al. (2012). The updated morphological properties from the HGPS catalog differ from those preliminary ones, which had underestimated the extent of the large, complex emission region (0.37° ± 0.03° vs. 0.17° ± 0.07°; both morphological models 2D symmetric Gaussian), likely due to the irregular shape of the emission. Previously there was a hint for additional structure, possibly a second source hidden in the tail of a dominant source, but this remains statistically insignificant in the HGPS analysis with respect to a single-source Gaussian morphology. Also of note, the best-fit centroid of the VHE emission is now located closer to the γ-ray pulsar (0.11° vs. 0.16° offset), bolstering the scenario in which the VHE emission is interpreted as a PWN powered by the pulsar. As expected for such changes in morphological properties, the HGPS spectral results also differ from the previously derived preliminary values.

The pulsar PSR J1459−6053 (also 3FGL J1459.4−6053) is a relatively old (τ_c = 65 kyr) but still very energetic HE γ-ray pulsar with a spin-down luminosity 9.1×10^{35} erg s^{-1} and unknown distance (d < 22 kpc) (Abdo et al. 2013). As noted above, it is offset 0.11° from the VHE centroid, which is consistent with offsets observed in other PSR and VHE PWN systems (e.g., Kargaltsev et al. 2013). The putative PWN has not been detected in X-rays potentially because of the age of the system (Ray et al. 2011) or HE γ-rays (Acero et al. 2013).

The new VHE spectrum (E > 0.46 TeV) is consistent with the 31–316 GeV *Fermi*-LAT upper limits. However, the conclusion, made by Acero et al. (2013), that the peak of the PWN's inverse Compton emission is located in this energy range has to be revised as the peak can now only be inferred to be at higher energies.

Apart from the HE γ-ray pulsar, there is a second HE source (3FGL J1456.7−6046) in the FoV. However, it is unclear if it is related to the PSR and PWN scenario, since it exhibits a highly curved, log-parabolic spectrum typical of blazars and a TS that fluctuates strongly with the choice of diffuse model or analysis method (Acero et al. 2015).

5.6.4. HESS J1503−582

HESS J1503−582 (Fig. 21) is a new source for which the origin of the VHE γ-ray emission is unidentified. H.E.S.S. earlier announced preliminary morphological and spectral properties

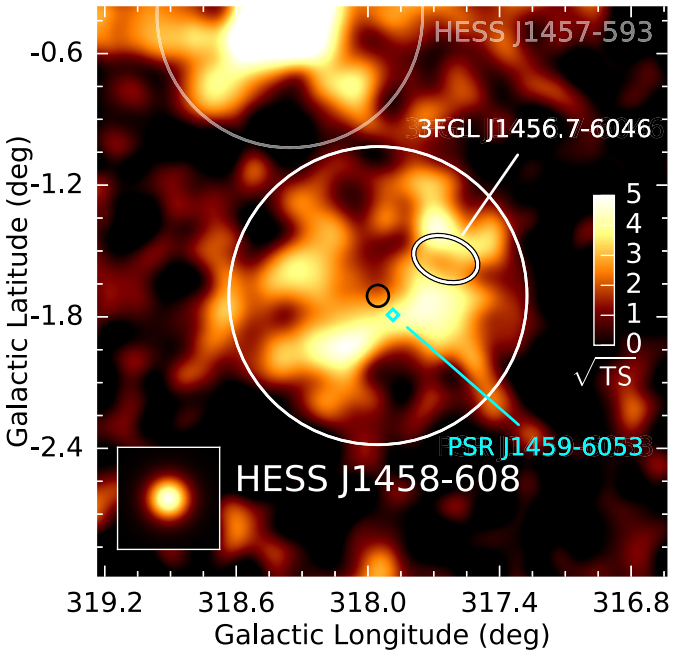

Fig. 20. VHE γ-ray image: HESS J1458−608. See Fig. 18 for a general description. Additionally, the ellipse represents the 95% uncertainty in the position of the HE γ-ray point source 3FGL J1456.7−6046, and the cyan diamond indicates the position of the pulsar. The FoV is $2.6° \times 2.6°$.

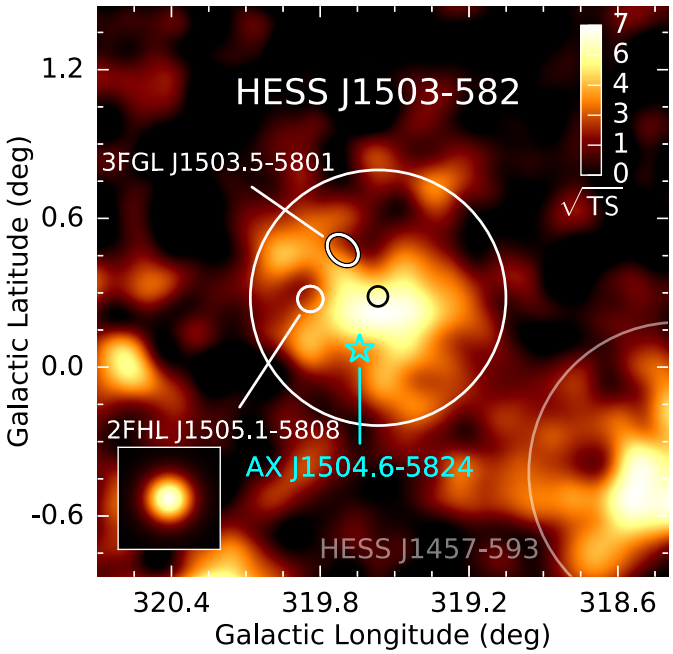

Fig. 21. VHE γ-ray image: HESS J1503−582. See Fig. 18 for a general description. Additionally, the ellipse represents the 95% uncertainty in the position of the HE γ-ray point source 3FGL J1503.5−5801; the circle represents the 68% uncertainty in the position of the HE ($E > 50$ GeV) γ-ray point source 2FHL J1505.1−5808; and the star represents the location of the X-ray point source. The FoV is $2.3° \times 2.3°$.

for this source (Renaud et al. 2008), which are now superseded by those in this paper. The VHE emission appears to be one of the softest ($\Gamma = 2.68 \pm 0.08_{\rm stat}$) in the HGPS, although both its morphological and spectral properties are affected by systematic uncertainties larger than nominal (see, e.g., Sects. 4.12 and 5.5).

A point-like HE ($E > 50$ GeV) γ-ray source, 2FHL J1505.1−5808 (Ackermann et al. 2016), is spatially coincident with the VHE emission region. A comparison of the VHE and HE ($E > 50$ GeV) spectra suggests that it may be a PWN (Ackermann et al. 2016), although no PWN or energetic pulsar has been detected so far. Another, different, point-like HE ($E > 100$ MeV) γ-ray source, 3FGL J1503.5−5801 (Acero et al. 2015), is also within the VHE region. Its nature is unknown, but its log-parabolic spectrum suggests it may not be directly related to HESS J1503−582.

Faint X-ray emission (AX J1504.6−5824, Sugizaki et al. 2001) is present toward the edge of the VHE emission. Nominally cataloged as a cataclysmic variable, its X-ray properties are not well known owing to the low *ASCA* sensitivity. Analysis of more sensitive data from other X-ray telescopes is needed to investigate the possibility it may be a PWN; this is the case despite a lack of an energetic pulsar in the vicinity, but bearing in mind the unknown nature of the nearby 3FGL source.

A relatively comprehensive search of MWL archives (Renaud et al. 2008) led to the investigation of an atypical scenario where the VHE emission could be linked with a forbidden velocity wing (FVW): faint, characteristic 21 cm H I line emission structures seen as deviations from the canonical Galactic rotation curve (Kang & Koo 2007). The hypothesis is that this FVW, FVW 319.8+0.3, may be related to an older SNR in its radiative phase, as was the case for two other FVWs (Koo et al. 2006; Kang et al. 2012). Although the SNR would no longer have sufficient shock velocity to accelerate particles responsible for producing VHE γ-rays (Ptuskin & Zirakashvili 2005), it could nevertheless be indicative of increased or more recent activity in the region (stellar winds and/or supernova explosions). A large H I shell, the result of such activity, is nearby (see McClure-Griffiths et al. 2002, GSH 319−01+13); however, its centroid is substantially offset by more than 1° from HESS J1503−582 and its extent considerably larger than the VHE emission region, so it seems unlikely to be related.

On the other hand, VERITAS also searched for VHE emission from an FVW, one which does show clear shell-type emission in H I (FVW 190.2+1.1). Despite observations that reached a sensitivity better than 1% Crab, VERITAS did not detect any significant VHE emission (Holder 2009). Furthermore, there is no definitive identification of VHE emission from young stellar clusters, with the possible exception of the superbubble 30 Dor C in the LMC (H.E.S.S. Collaboration 2015e). Therefore, this FVW scenario remains speculative.

5.6.5. HESS J1554−550

VHE γ-ray emission from the new source HESS J1554−550 (Fig. 22) is firmly identified with the PWN G327.15−1.04 within the composite SNR G327.1−1.1, on the basis of both a spatial coincidence with the PWN and the size of the VHE emission region, which can be constrained to less than 0.035°. Preliminary H.E.S.S. morphological and spectral properties of the VHE source were first published by Acero et al. (2012) and are compatible with the HGPS results. However, while previously the source size was given as $0.03° \pm 0.01°$, the more conservative HGPS analysis procedure used here (Sect. 4.10.2) finds the source to be compatible with being point-like, and there is a limit on the size that is nonetheless compatible.

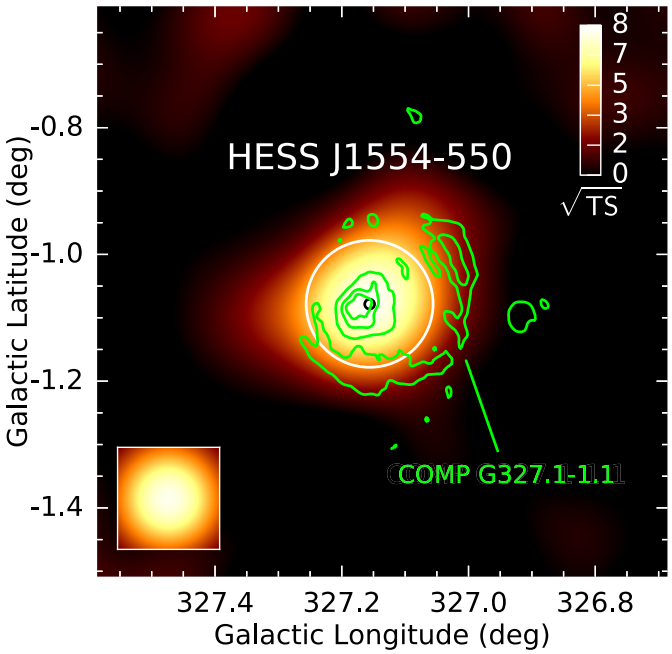

Fig. 22. VHE γ-ray image: HESS J1554−550. See Fig. 18 for a general description. Additionally, the composite SNR is shown by plotting its 843-MHz radio intensity (Whiteoak & Green 1996) with contours at 1, 8, and 15 mJy beam^{-1}. The FoV is 0.9° × 0.9°.

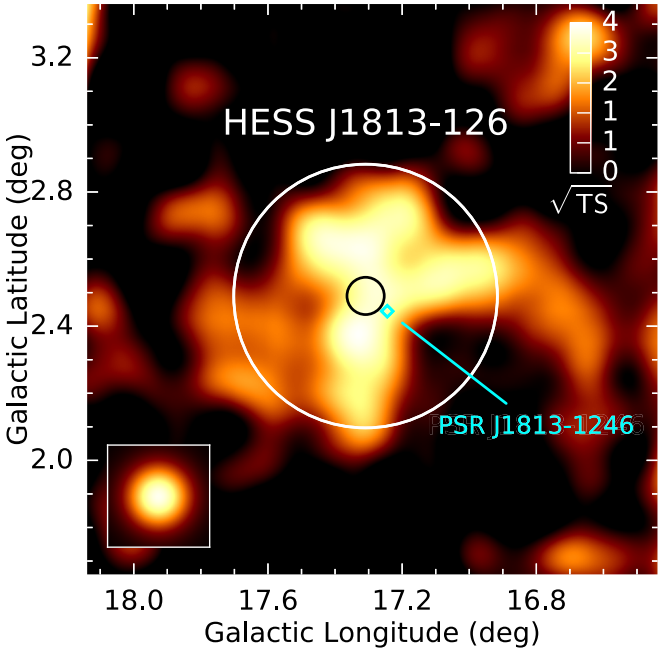

Fig. 23. VHE γ-ray image: HESS J1813−126. See Fig. 18 for a general description. Additionally, the position of the pulsar is denoted by a cyan diamond. The FoV is 1.7° × 1.7°.

The VHE size limit rules out significant emission from the outer shell of the SNR and is compatible with the compact, nonthermal PWN, which is observed in both radio and X-rays (Temim et al. 2009, 2015) but not HE γ-rays (Acero et al. 2013; Ackermann et al. 2016). Furthermore, the VHE centroid is compatible with the peak of the radio emission from the PWN and the tail of X-ray PWN. Although pulsed emission from the putative pulsar at the heart of the composite SNR has not been detected in radio, X-ray, nor HE γ-ray bands, the X-ray data provide evidence for the existence of a powerful pulsar, that has an estimated $\dot{E} = 3.1 \times 10^{36}$ erg s^{-1} (Temim et al. 2015). The distance to the SNR is not well determined, but has been estimated to be roughly 9 kpc (Sun et al. 1999). Assuming this distance, the VHE luminosity of HESS J1554−550 is $L_\gamma(1\text{–}10\ \mathrm{TeV}) = 1.0 \times 10^{34}(d/9\ \mathrm{kpc})^2$ erg s^{-1} and the apparent efficiency $\epsilon_{1-10\ \mathrm{TeV}} \equiv L_\gamma/\dot{E} = 0.3\%$, which is compatible with the efficiencies ($\lesssim$10%) of other VHE sources that have been identified as PWNe (Kargaltsev et al. 2013).

5.6.6. HESS J1813−126

The HGPS catalog analysis has revealed an intriguing new source of VHE γ-rays (Fig. 23) not previously detected, one of the few off-plane VHE sources ($b = 2.5°$). The only plausible MWL counterpart associated with this emission is the energetic pulsar PSR J1813−1246 (Abdo et al. 2009a), marginally coincident with the VHE best-fit centroid. This suggests the VHE emission originates in a PWN powered by the pulsar, which has a spin-down luminosity $\dot{E} = 6.3 \times 10^{36}$ erg s^{-1} and characteristic age $\tau_c = 43$ kyr. The pulsar is one of the brightest γ-ray pulsars (3FGL J1813.4−1246, Acero et al. 2015) and the second-most energetic, radio-quiet pulsar. This pulsar also been found to exhibit strong X-ray pulsations, and its distance has been recently constrained to $d > 2.5$ kpc (Marelli et al. 2014). This implies a lower limit on the VHE luminosity $L_\gamma(1\text{–}10\ \mathrm{TeV}) > 2.9 \times 10^{33}$ erg s^{-1} and a corresponding limit on the apparent efficiency $\epsilon_{1-10\ \mathrm{TeV}} > 0.05\%$.

In other energy bands, no off-pulse emission (e.g. emission from the putative PWN) is detected in HE γ-rays (0.1–100 GeV) based on the analysis of five years of *Fermi*-LAT data (Marelli et al. 2014), dismissing earlier hints for a GeV PWN (Ackermann et al. 2011; Abdo et al. 2013), likely owing to the larger data set and improved models for diffuse emission used in the new analysis. In X-rays (0.3–10 keV), despite relatively deep *XMM-Newton* (130 ks) and *Chandra* (50 ks) observations, no PWN is detected beyond 1–1.5″ from the pulsar (Marelli et al. 2014). This is very unusual for a pulsar this energetic; that is the derived upper limits in X-rays are only marginally compatible with known relations between PWN and pulsar luminosities (Kargaltsev & Pavlov 2008) and between PSR luminosity and distance to the PWN termination shock (Gaensler & Slane 2006).

Therefore, HESS J1813−126 appears to be a rare case of a relic PWN (de Jager & Djannati-Ataï 2009) currently detected exclusively in the VHE domain. Observations in the hard X-ray domain with *NuSTAR* would be useful to investigate the hint of a signal seen at 30–520 keV with *INTEGRAL* (Marelli et al. 2014) and to determine if there is an unpulsed, nebular component visible at those energies. Regardless, further work modeling the MWL spectral energy distribution is necessary to fully investigate this intriguing system.

5.6.7. HESS J1826−130

The HGPS catalog analysis reveals a distinct new source of VHE γ-rays, HESS J1826−130 (Fig. 24), in what was previously considered extended emission from the nearby PWN HESS J1825−137 (Aharonian et al. 2006f). Because of the very close proximity to its bright neighbor, the spectral measurement

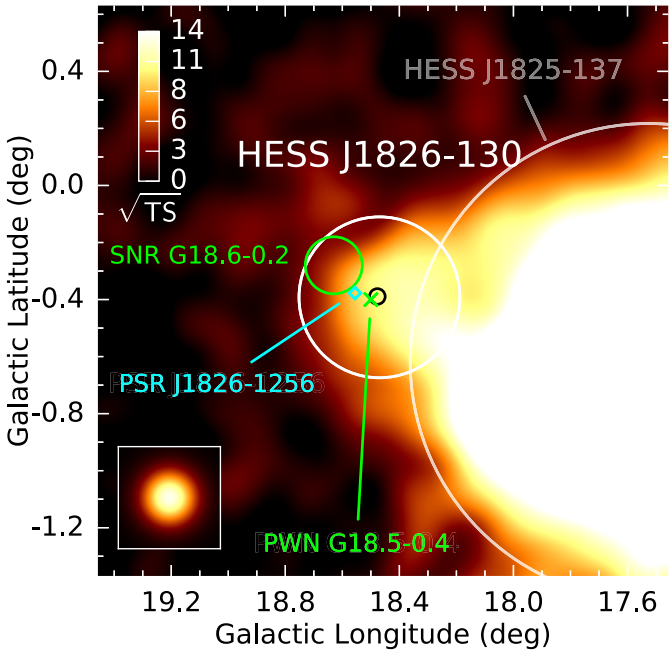

Fig. 24. VHE γ-ray image: HESS J1826−130. See Fig. 18 for a general description. Additionally, the approximate centroid of the PWN is marked by a green cross, and the pulsar position is marked by a cyan diamond. The FoV is 2.0° × 2.0°.

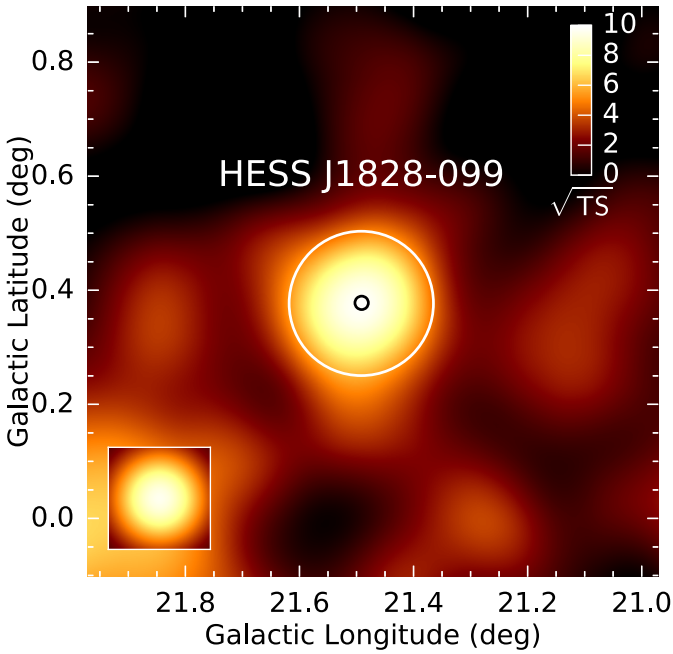

Fig. 25. VHE γ-ray image: HESS J1828−099. See Fig. 18 for a general description. The FoV is 1.0° × 1.0°.

is highly contaminated (41%). Angüner et al. (2017) reported preliminary findings for this new source.

HESS J1826−130 is associated with the "Eel" PWN[11] (PWN G18.5−0.4), an elongated, nonthermal, X-ray source observed with *Chandra* (Roberts et al. 2007), and the energetic pulsar PSR J1826−1256 (Abdo et al. 2009a), on the basis of a spatial coincidence. The best-fit VHE centroid is compatible with the Eel, while the pulsar is somewhat offset (0.09°) from the centroid but well within the VHE emission region (size 0.15° ± 0.02°). The pulsar is now notable for being one of the brightest radio-quiet γ-ray pulsars (3FGL J1826.1−1256; Acero et al. 2015). The distance of the pulsar is unfortunately not known, which precludes conclusions on the energetics, but its position, $\dot{E} = 3.6 \times 10^{36}$ erg s^{-1}, and $\tau_c = 14$ kyr suggest it is probably powering the Eel. The PWN is not detected in HE γ-rays (Ackermann et al. 2011, 2016). Finally, we note that dense molecular gas was also found overlapping HESS J1826−130 at a distance matching that of the dispersion measure of the pulsar (Voisin et al. 2016), suggesting a possible hadronic origin for this VHE source.

The SNR G18.6−0.2 (Brogan et al. 2006) is also coincident with the VHE emission region, although it is significantly smaller in size (0.1° diameter). Very little is known about this SNR, except that a partial shell-type morphology has been observed so far only in radio and IR and that its distance is estimated to be 4.0–5.2 kpc (Johanson & Kerton 2009).

A firm identification of the VHE source as a PWN is not possible at this time, in part resulting from the unknown distance to the Eel PWN and PSR system and the poorly studied SNR. We are currently preparing more advanced VHE spectral analysis methods that can account for contamination in crowded FoVs. These methods will enable more accurate modeling of the SED.

[11] Roberts et al. (2007), based on visual inspection of the VHE images, first suggested that the VHE emission is separate from the PWN HESS J1825−137 and associated it with the Eel.

5.6.8. HESS J1828−099

HESS J1828−099 is a new source of VHE γ-rays (Fig. 25), which is unique because it appears to be completely dark at lower energies with no apparent associations (see Table A.9). It is also notable for being one of the 17 point-like sources in the HGPS catalog with a size (Gaussian std. dev.) less than 0.07°. The detection of a spatially coincident HE γ-ray source has been claimed (Neronov & Semikoz 2010) but not confirmed with the latest, significantly larger *Fermi*-LAT data sets, i.e. there is no respective source neither in the 3FGL catalog (Acero et al. 2015) nor 2FHL catalog ($E > 50$ GeV; Ackermann et al. 2016). Deeper follow-up observations in especially the radio and X-ray bands are strongly encouraged to probe nonthermal emission.

5.6.9. HESS J1832−085

HESS J1832−085 (Fig. 26) is an unidentified source of VHE γ-rays. It is notable for its point-like morphology, which is measured to be less than 0.05° in extension, and its scarcity of promising MWL counterparts.

An interesting object that is spatially coincident with HESS J1832−085 is the pulsar PSR J1832−0827 (Clifton & Lyne 1986), which has so far only been detected in radio wavelengths. The pulsar is likely at a distance of ≈4.9 kpc (Cordes & Lazio 2002), in agreement with other estimates in the range 4.4–6.1 kpc (Frail et al. 1991) and has a spin-down luminosity[12] $\dot{E} = 9.3 \times 10^{33}$ erg s^{-1} (Hobbs et al. 2004b). It is one of the few pulsars with a measured braking index, $n = 2.5 \pm 0.9$ (Johnston & Galloway 1999), providing a characteristic age $\tau_c \approx 200$ kyr. Another very intriguing object in the FoV is the energetic millisecond pulsar PSR J1832−0836, which has a 2.7 ms period (Burgay et al. 2013). It has a spin-down luminosity $\dot{E} = 1.7 \times 10^{34}$ erg s^{-1}, a very large characteristic age (typical

[12] This pulsar was not selected by the standardized HGPS association procedure (Sect. 5.1) as a possible counterpart because its luminosity is just below the $\dot{E} > 10^{34}$ erg s^{-1} threshold.

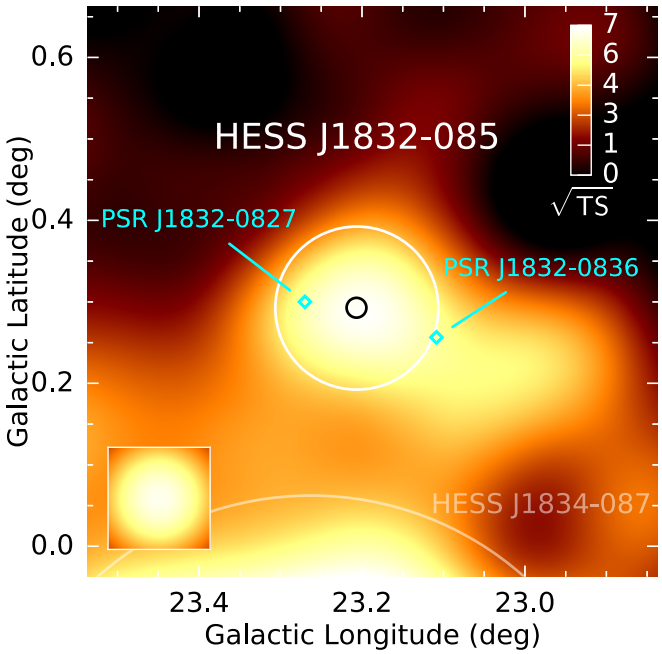

Fig. 26. VHE γ-ray image: HESS J1832−085. See Fig. 18 for a general description. Additionally, the position of the two pulsars are denoted by cyan diamonds. The FoV is $0.7° \times 0.7°$.

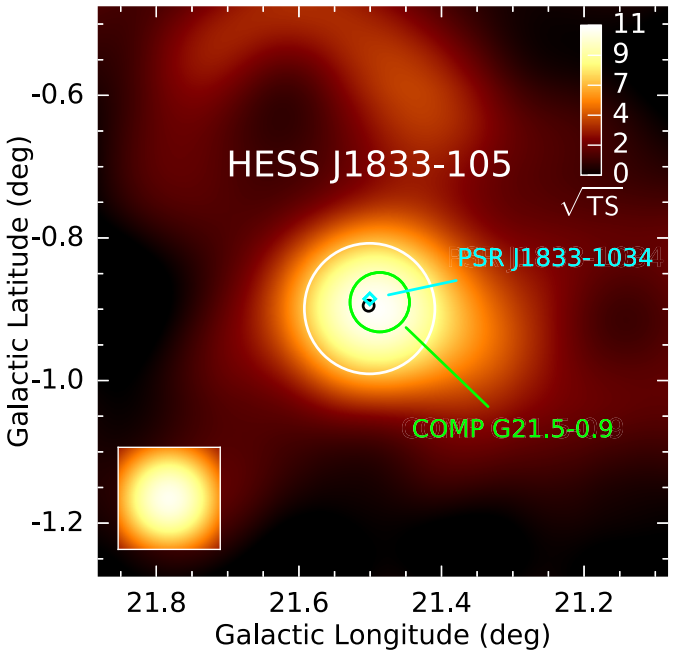

Fig. 27. VHE γ-ray image: HESS J1833−105. See Fig. 18 for a general description. Additionally, the composite SNR is shown by plotting a green circle approximating the radio shell, and the pulsar position is denoted by a cyan diamond. The FoV is $0.8° \times 0.8°$.

of millisecond pulsars) $\tau_c = 5 \times 10^9$ kyr, and distance 1.1 kpc (Cordes & Lazio 2002).

There are no known PWNe associated with these two pulsars nor close to HESS J1832−085. If either or both of these pulsars are powering VHE PWNe, a relatively large conversion efficiency of $\epsilon_{1-10\,\mathrm{TeV}} \sim 23\%$ would be required for PSR J1832−0827, and a more reasonable $\epsilon_{1-10\,\mathrm{TeV}} \sim 0.6\%$ for PSR J1832−0836. The older ages are at odds with the inferred small sizes of the VHE PWNe, constrained to be less than $\approx 4\ (d/4.9\ \mathrm{kpc})$ pc and $\approx 1\ (d/1.1\ \mathrm{kpc})$ pc, respectively. These circumstances, plus the borderline low spin-down luminosity of PSR J1832−0827, combine to disfavor a PSR and PWN scenario as the origin of the VHE emission in light of the known VHE PWN population (H.E.S.S. Collaboration 2018e). The millisecond pulsar scenario is even more uncertain. That pulsar is slightly more energetic and much closer, but thus far millisecond pulsars, with ages of billions of years, are not known to produce PWNe that emit detectable levels of γ-rays at TeV energies. Therefore, the origin of the emission from this new, enigmatic, VHE γ-ray source is still very much unclear.

5.6.10. HESS J1833−105

VHE γ-ray emission from the new source HESS J1833−105 (Fig. 27) can now be firmly identified with the composite SNR G21.5−0.9 (Wilson & Weiler 1976), which contains a Crab-like PWN. Preliminary H.E.S.S. source properties were previously shown (Djannati-Ataï et al. 2008) and are compatible with the HGPS results, although at the time it was not yet possible to disentangle the possible contributions to the VHE emission from the PWN and SNR shell.

The new identification is supported by a positional coincidence between the VHE emission centroid and the PWN center, but most importantly by the lack of extension of the VHE emission region; this region is constrained to be less than 0.03°, which is our systematic limit for source sizes. This implies that we cannot claim significant VHE emission from the forward shock of the spherical, faint SNR shell at a radius of 0.038° (Bocchino et al. 2005).

The PWN has also been detected in X-rays (Safi-Harb et al. 2001; Bocchino et al. 2005) and IR (Zajczyk et al. 2012) although not in HE γ-rays (Acero et al. 2013), and its distance has been estimated to be $d \approx 4.8$ kpc (Tian & Leahy 2008). It is powered by the very energetic PSR J1833−1034, currently the fifth most energetic pulsar known in the Galaxy, and has a spin-down luminosity $\dot{E} \approx 3.4 \times 10^{37}$ erg s^{-1}. The pulsar has been detected in radio (Gupta et al. 2005; Camilo et al. 2006) and HE γ-rays (as 3FGL J1833.5−1033; Acero et al. 2015). The age of the system has been argued to be 870^{+200}_{-150} yr (Bietenholz & Bartel 2008), which is significantly less than the $\tau_c = 4.9$ kyr of the pulsar.

Considering the luminosity of HESS J1833−105, $L_\gamma(1{-}10\ \mathrm{TeV}) = 2.6 \times 10^{33}\ (d/4.9\ \mathrm{kpc})^2$ erg s^{-1}, the apparent efficiency converting the rotational energy of the pulsar to γ-rays, $\epsilon_{1-10\,\mathrm{TeV}} \equiv L_\gamma/\dot{E} = 0.08\%$, is compatible with the efficiencies ($\lesssim 10\%$) of other VHE sources that have been identified as PWNe (Kargaltsev et al. 2013).

The HGPS results confirm predictions that the PWN would emit VHE γ-rays at the level of a few percent of the Crab Nebula and exhibit a relatively hard spectrum (de Jager et al. 1995).

5.6.11. HESS J1843−033

An extended region of VHE emission, called HESS J1843−033, was first published by Hoppe (2008b). This emission is resolved by the HGPS catalog analysis into three components that

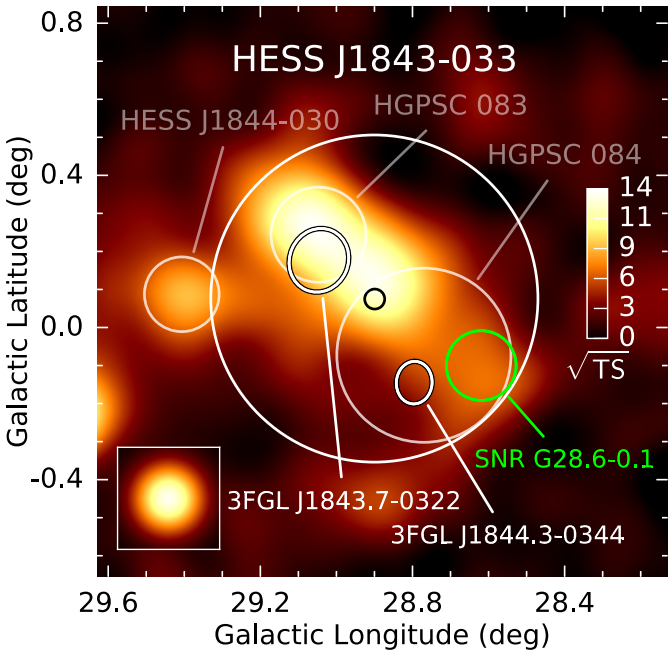

Fig. 28. VHE γ-ray image: HESS J1843−033. See Fig. 18 for a general description. Additionally, the SNR is shown by plotting a green circle approximating the radio shell. The 3FGL ellipses represents the 95% uncertainty in the position of the HE γ-ray point sources. The FoV is $1.4° \times 1.4°$.

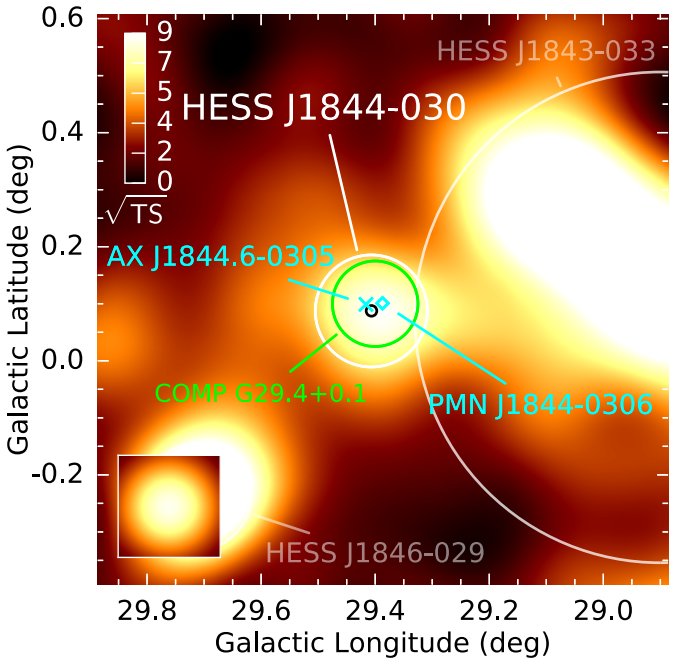

Fig. 29. VHE γ-ray image: HESS J1844−030. See Fig. 18 for a general description. Additionally, the composite SNR is shown by plotting a green circle approximating the radio shell. The position of the X-ray source is denoted by a cross, while the position of PMN J1844−0306 is indicated by a diamond. The FoV is $1.0° \times 1.0°$.

were merged into two distinct sources: HESS J1843−033 and HESS J1844−030.

HESS J1843−033 consists of two merged offset components (HGPSC 83 and HGPSC 84) and is therefore highly structured (see Fig. 28). The image of the source shows two peaks separated by ∼0.2°. The first Gaussian component is clearly associated with the upper peak. The second Gaussian component is larger and offset with respect to the lower peak. This is due to more diffuse, low-brightness emission around $(\ell, b) = (28.6°, -0.1°)$, suggesting the presence of another currently unresolved source that shifts the position of the second component. HESS J1843−033 is therefore most probably a complex region with overlapping sources that were merged in the HGPS analysis.

Two GeV sources, 3FGL J1843.7−0322 and 3FGL J1844.3−0344, are found within the R80 extension of the source. The former is found in the main region of emission but does not seem to correlate well with any of the two main peaks. The latter *Fermi*-LAT source is located in the low-brightness region around $(\ell, b) = (28.6°, -0.1°)$.

No compelling radio counterpart was found in the VLA Galactic Plane Survey (Stil et al. 2006). Dedicated X-ray observations show the presence of a faint absorbed extended source with a nonthermal spectrum that is coincident with the HGPSC 83 component. No compelling counterpart for the second component has been found. We note however that the nearby radio SNR G28.6−0.1 (Helfand et al. 1989) is filled with nonthermal X-rays (Ueno et al. 2003). If this emission is due to synchrotron X-rays produced by energetic electrons, IC emission at VHE is likely contributing to the low-brightness emission that is visible around the SNR position in Fig. 28.

5.6.12. HESS J1844−030

HESS J1844−030 is a faint VHE γ-ray source that compatible with being point-like and located in the vicinity of the complex region of HESS J1843−033. It is positionally coincident with a number of distinct objects, most notably the radio source PMN J1844−0306 (cyan diamond in Fig. 29). The nature of the latter is ambiguous. Its elongated, jet-like morphology is very reminiscent of a radio galaxy, which is supported by 6 cm VLA observations revealing polarization along the structure (Helfand et al. 1989). This elongated radio feature is surrounded by a partial ring visible in the 21 cm VLA continuum image. The object is therefore classified as a SNR candidate in the MAGPIS catalog (Helfand et al. 2006), G29.37+0.10. It is also coincident with the X-ray source AX J1844.7−0305 (Vasisht et al. 2000; Sugizaki et al. 2001).

The association of the jet radio feature and the SNR candidate is unclear. Although rare, SNRs with jets are plausible, for example PWN structures such as MSH 15−52 (Gaensler et al. 2002) or the SS433/W 50 microquasar SNR system with its radio jets and lobes (Dubner et al. 1998; H.E.S.S. Collaboration 2018m). The jet structure could also be a background radio galaxy aligned by chance with a faint radio shell. We note, however, thanks to H I absorption, Johanson & Kerton (2009) place the source at a distance between 5 and ∼15 kpc. Interestingly, a heavily absorbed X-ray PWN, dubbed G29.4+0.1, is present in SNRcat and overlaps with a part of PMN J1844−0306. Further MWL observations will be necessary to assess the nature of the system and the origin of the VHE emission.

5.6.13. HESS J1846−029

VHE γ-ray emission from the new source HESS J1846−029 (see Fig. 30) is spatially coincident with G29.7−0.3 (also known as Kes 75), one of the youngest composite SNRs in the Galaxy, which contains the nebula of PSR J1846−0258. Preliminary results were presented in Djannati-Ataï et al. (2008) and are compatible with those obtained in the HGPS analysis.

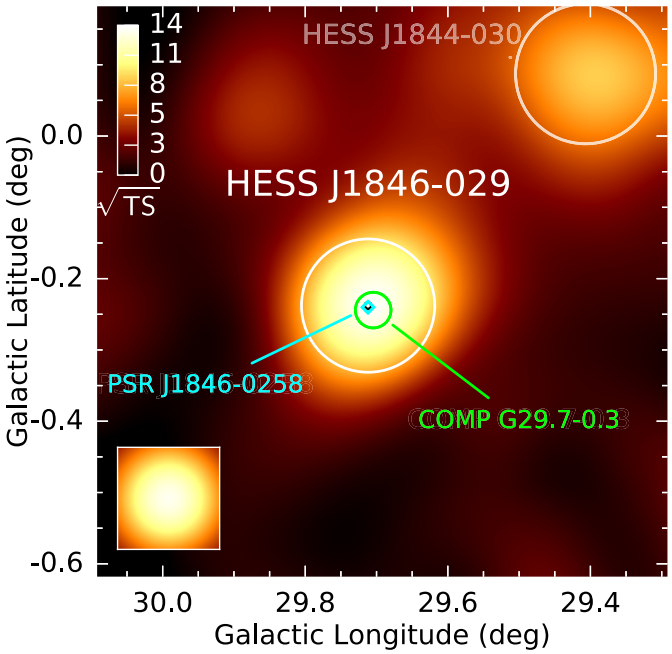

Fig. 30. VHE γ-ray image: HESS J1846−029. See Fig. 18 for a general description. Additionally, the composite SNR is shown by plotting a green circle approximating the radio shell. The position of the pulsar is indicated by a cyan diamond. The FoV is 0.8° × 0.8°.

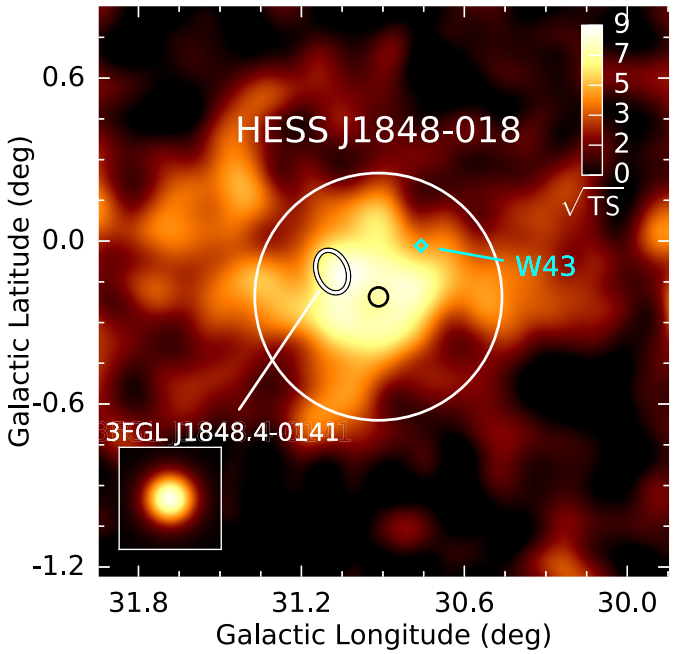

Fig. 31. VHE γ-ray image: HESS J1848−018. See Fig. 18 for a general description. Additionally, the 3FGL ellipse represents the 95% uncertainty in the position of the HE γ-ray point source. The central stellar cluster of the mini-starburst W 43 is denoted by a diamond. The FoV is 2.1° × 2.1°.

PSR J1846−0258 is a young, high magnetic-field pulsar. This source has a rotation period of 324 ms and a spin-down power of 8.3×10^{36} erg s^{-1}. It is among the youngest pulsars in the Galaxy with a characteristic age of only 723 yr (Livingstone et al. 2006). It has experienced a strong increase in its pulsed flux in June 2006 associated with spectral (Kumar & Safi-Harb 2008) and timing (Gavriil et al. 2008) changes in a similar manner to magnetars. The result of the search for variations in the VHE source flux at various timescales was negative (Terrier et al. 2008a).

A nebula of 20″ in radius surrounds the pulsar in radio and X-ray wavelengths and *Chandra* high-resolution observations have revealed a jet and torus (Ng et al. 2008). A 3′ diameter asymmetric radio shell surrounds the PSR and PWN system. It consists mainly of two lobes to the south of the pulsar. These lobes are emitting X-rays from heated swept-up interstellar matter and ejecta (Morton et al. 2007). Infrared measurements suggest that the shock is in a region of typical density of 60 cm^{-3} (Temim et al. 2012). Su et al. (2009) found a bubble in the molecular matter in good coincidence with the SNR. They proposed that this structure is the wind blown bubble of the SNR progenitor.

The extension of the VHE emission from HESS J1846−029 is compatible with that of a point-like source. The upper limit on the size is 0.03°, that is, comparable with the SNR shell size. The position of this object is compatible with the position of PSR J1846−0258, within localization uncertainties. Therefore, we are not able to distinguish between emission from the shell and emission from the PWN in this composite object.

Assuming a distance of 6 kpc (Leahy & Tian 2008), which yields a luminosity of $L_\gamma(1 - 10\ \mathrm{TeV}) = 6.9 \times 10^{33}\ (d/6\ \mathrm{kpc})^2$ erg s^{-1}, the apparent conversion efficiency of the rotational energy of the pulsar to γ-rays is $\epsilon_{1-10\,\mathrm{TeV}} \equiv L_\gamma/\dot{E} = 0.08\%$. The VHE emission is therefore completely consistent with an origin in the PWN (see also, e.g., Tanaka & Takahara 2011; Torres et al. 2014). Yet, given the uncertainties on extension it is not possible to exclude a contribution from γ-rays produced by particles accelerated at the SNR shock, in particular from collisions of hadrons with ambient and swept-up matter at the shock, or even a contribution of escaping particles with the molecular shell revealed by Su et al. (2009).

5.6.14. HESS J1848−018

For the new source HESS J1848−018 (Fig. 31) preliminary H.E.S.S. source properties were previously shown (Chaves et al. 2008b). These properties are compatible with the HGPS results except for the source size and flux; these were overestimated because the earlier analysis did not include a model for the diffuse emission (see Sect. 4.6), which is particularly bright in this region.

The origin of the VHE γ-ray emission of HESS J1848−018 is not yet firmly identified. No SNR or energetic pulsar is currently detected in the proximity, although we have associated the VHE source with 3FGL J1848.4−0141 (Acero et al. 2015). This unidentified HE γ-ray point source is significantly offset from the VHE γ-ray centroid (by ∼0.2°) but well within the VHE emission region. Studies attempting to relate the HE with the (preliminary) VHE morphology and spectra remained inconclusive (Tam et al. 2010; Acero et al. 2013). A potential PSR and PWN scenario cannot be confirmed due to the lack of a detected pulsar (at any wavelength), although the HE spectrum does exhibit curvature typical of pulsars (Acero et al. 2015). Furthermore, there is no known PWN nearby, although one study has shown marginal statistical evidence for an extension of the HE source (Lemoine-Goumard et al. 2011), which is expected if the HE emission is from a PWN or the combination of a pulsar and PWN.

An extensive search for other MWL counterparts found the VHE γ-ray emission to be in the direction of the massive star-forming region W 43, a very active mini-starburst

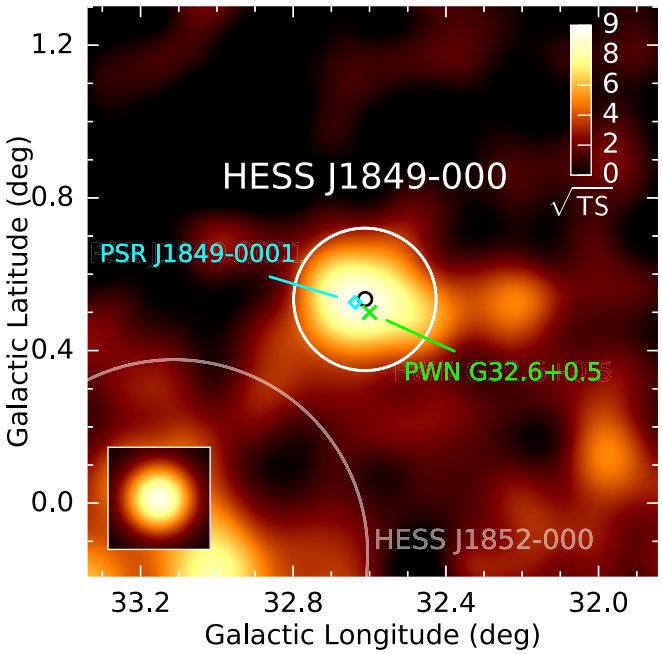

Fig. 32. VHE γ-ray image: HESS J1849−000. See Fig. 18 for a general description. Additionally, the position of the pulsar is indicated by a cyan diamond and the PWN by a green cross. The FoV is 1.5° × 1.5°.

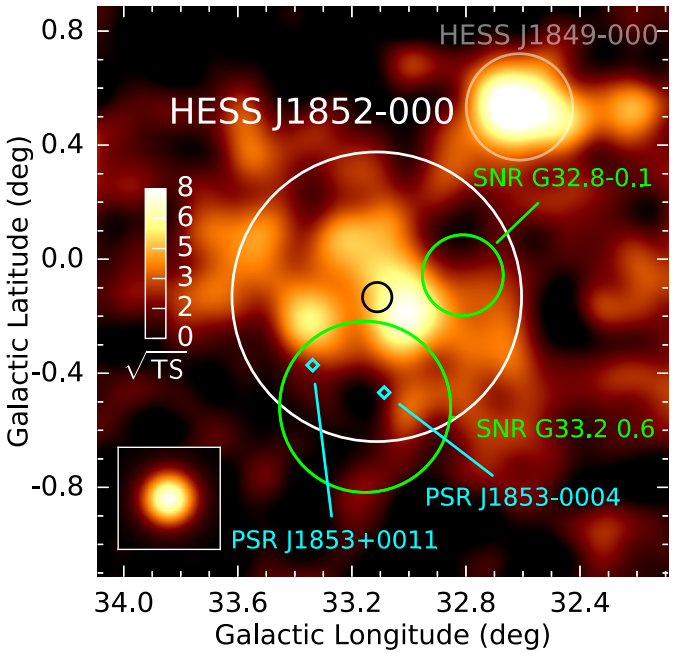

Fig. 33. VHE γ-ray image: HESS J1852−000. See Fig. 18 for a general description. Additionally, the position of the pulsars are indicated by cyan diamonds, and the SNR is shown by plotting a green circle approximating the radio shell. The FoV is 2.0° × 2.0°.

located at a distance of 6.2 ± 0.6 kpc (Russeil 2003). It is one of the closest and most luminous star-forming regions in the Galaxy (Motte et al. 2003), hosting a giant H II region (G30.8−0.2), a giant molecular cloud, and the Wolf-Rayet binary star system WR 121a in the central stellar cluster together with O-type stars. The massive stars in the dense central cluster exhibit strong stellar winds with extreme mass loss rates, in particular the WN7-subtype WR 121a (Blum et al. 1999).

This unique MWL environment is of interest because the central cluster of W 43 could be the site of efficient particle acceleration in various plausible hadronic scenarios involving the high-velocity (up to 2000 km s^{-1}) stellar winds (e.g., Reimer et al. 2006; Romero 2010). Furthermore, the very large amount of molecular gas present in W 43 (~7×10^6 $M_\odot$; Nguyen Luong et al. 2011) provides a natural target for accelerated cosmic rays (regardless of their potential acceleration site), which would lead to γ-ray production via hadronic p-p collisions (e.g., Aharonian 1991).

It is not yet possible to confirm the W 43 hadronic scenario for the origin of the VHE emission, in part because of the very complex morphologies present and the challenges in correlating features observed in radio and infrared observations at arcsecond scales with the ~5′ resolution in VHE. The VHE centroid, in particular, is significantly offset from the central cluster by ~0.2°, although the extended VHE emission is generally coincident with the W 43 complex. This scenario remains under investigation, especially in light of the recent detection of the superbubble 30 Dor C in the LMC (H.E.S.S. Collaboration 2015e), which suggests that particle acceleration occurring in the collective winds of massive stars can indeed produce VHE emission.

5.6.15. HESS J1849−000

The faint, slightly extended source HESS J1849−000 (see Fig. 32) was first reported by Terrier et al. (2008b). It was found to be spatially coincident with the hard X-ray source IGR J18490−0000 (Krivonos et al. 2012). *XMM-Newton* observations revealed a nonthermal, point-like, X-ray source surrounded by a nebula, making this object a solid PWN candidate. Follow-up observations of the hard X-ray source with *RXTE* have confirmed this hypothesis with the discovery of a 38.5 ms periodicity of the X-ray signal (Gotthelf et al. 2011). The associated pulsar, PSR J1849−0001, was found to have a spin-down luminosity $\dot{E} = 9.8 \times 10^{36}$ erg s^{-1} and a characteristic age $\tau_c = 42.9$ kyr.

The HGPS analysis confirms the existence of a source coincident with PSR J1849−0001. The best-fit position of HESS J1849−000 is located less than 0.03° from the X-ray pulsar position (cyan diamond on Fig. 32), well within statistical uncertainties in both source localizations. The best-fit size of the VHE emission is 0.09°, which is about a factor of two larger than that of the extended X-ray component (Gotthelf et al. 2011; Kuiper & Hermsen 2015).

The source has an energy flux ~2.1×10^{-12} erg cm^{-2} s^{-1}, in the range 1–10 TeV, a factor of ~2 above the X-ray nebula energy flux in the range 2–10 keV (Kuiper & Hermsen 2015). This confirms the likely nature of HESS J1849−000 as a PWN in transition between a young, synchrotron-dominated phase and an evolved, IC-dominated phase.

5.6.16. HESS J1852−000

The new source of VHE γ-ray emission HESS J1852−000 (Fig. 33) is currently unidentified due to multiple source counterpart confusion. It is spatially associated with the partial shell-type SNR G32.8−0.1 (also known as Kes 78; Kesteven 1968; Velusamy & Kundu 1974), the incomplete shell-type SNR G33.2−0.6 (Reich 1982), and two energetic pulsars, PSR J1853−0004 and PSR J1853+0011 (Hobbs et al. 2004a). Preliminary H.E.S.S. source properties were previously shown (Kosack et al. 2011) and are compatible with the HGPS

results. As mentioned in Sect. 5.5, the spectral properties of HESS J1852−000 are affected by systematic uncertainties larger than nominal.

The VHE emission is located along the eastern edge of SNR Kes 78 but extends well beyond the SNR. The SNR itself is characterized by an elongated and partial nonthermal shell seen in radio and X-rays (Zhou & Chen 2011; Bamba et al. 2016). It is interacting with adjacent molecular clouds, evidenced by the detection of a shock-excited OH(1720 MHz) maser on the shell (Koralesky et al. 1998) and studies of the CO molecular environment (Zhou & Chen 2011). The distance of the SNR is estimated to be ∼5 kpc (Koralesky et al. 1998; Zhou & Chen 2011), although ∼8.8 kpc has also been suggested (e.g., Xu & Zhang 2009). A hadronic origin of the VHE emission has been briefly discussed (Kosack et al. 2011), involving escaped cosmic rays from Kes 78 (e.g., Aharonian 1991; Gabici et al. 2007). However, the scenario remains unconfirmed in the absence of a more detailed study of the gas environment and its potential correlation with the complex VHE morphology.

The presence of two radio pulsars, PSR J1853−0004 and PSR J1853+0011, within the VHE emission region also suggests that the VHE γ-rays could originate in one of the PWN or could even be a result of superimposed emission from two PWNe. Although there are currently no known PWNe at other energies, the pulsars' spin-down luminosities $\dot{E} = 2.1 \times 10^{35}$ erg s^{-1} and 2.1×10^{34} erg s^{-1}, respectively, and distances $d = 6.6$ kpc and 7.5 kpc, are reasonable in the context of other pulsars thought to be powering VHE PWNe (H.E.S.S. Collaboration 2018e). The pulsars have so far only been detected in radio, although PSR J1853−0004 has been associated with the HE γ-ray source 3FGL J1853.2+0006, which is itself a source whose existence and properties are currently uncertain (subject to analysis Flags 3 and 4 in Acero et al. 2015).

In conclusion, it is not yet clear whether the VHE emission originates from a hadronic SNR and molecular cloud interaction, previously undetected PWNe associated with one or both of the spatially coincident pulsars, or some other yet unknown source.

5.6.17. Source candidates

Three VHE γ-ray source candidates (hotspots) were found above the TS = 30 detection threshold in one HGPS analysis (primary or cross-check), but these candidates had TS < 30 in the other analysis. These should be considered unconfirmed, or candidate, VHE sources to be confirmed by deeper VHE observations.

HOTS J1111−611. The VHE emission from the source candidate HOTS J1111−611 has a significance of TS = 22 (cross-check TS = 41). It is located at $(\ell,\ b) = (291.18° \pm 0.03°,\ -0.54° \pm 0.03°)$, has a measured integral flux $F(E > 1\ \mathrm{TeV}) = 3.8 \times 10^{-13}$ cm^{-2} s^{-1}, and a size $0.09° \pm 0.03°$. It is located near (∼0.1°) the very energetic $\tau_c = 32.7$ kyr pulsar PSR J1112−6103 (Manchester et al. 2001) emitting in radio and HE γ-rays (3FGL J1111.9−6058, Abdo et al. 2013). The pulsar has a high spin-down luminosity $\dot{E} = 4.5 \times 10^{36}$ erg s^{-1} and a distance of 12.2 kpc (Cordes & Lazio 2002). Moreover, a significant HE γ-ray source (2FHL J1112.1−6101e, Ackermann et al. 2016) above 50 GeV has been reported at 0.04° from the pulsar, which makes this HE source likely to be a PWN. The characteristics of this pulsar, the apparent efficiency $\epsilon_{E>1\ \mathrm{TeV}} \sim 1\%$, and the presence of a HE component in its vicinity suggests that it could plausibly power a VHE PWN.

HESS J1831−098. The source candidate HESS J1831−098 is found to have TS = 59 in the main HGPS analysis but only TS = 17 in the cross-check analysis and is therefore considered a source candidate. HESS J1831−098 is located in a complex region with nearby diffuse components, which might explain the discrepancy observed for this source candidate. Preliminary VHE morphological and spectral properties on HESS J1831−098 were announced by Sheidaei (2011). This source candidate is coincident with the energetic pulsar PSR J1831−0952, which exhibits a spin-down luminosity of 1.1×10^{36} erg s^{-1} and a characteristic age of 128 kyr. According to Sheidaei (2011), a $\epsilon_{1-20\ \mathrm{TeV}} \sim 1\%$ conversion efficiency from rotational energy to γ-rays would be required to power a PWN; this is similar to values observed in other VHE PWN.

HOTS J1907+091. The VHE emission from source candidate HOTS J1907+091 has a significance of only TS = 18 (cross-check TS = 43). It is located at $(\ell,\ b) = (42.88° \pm 0.08°,\ 0.69° \pm 0.08°)$, has a measured integral flux $F(E > 1\ \mathrm{TeV}) = 4.3 \times 10^{-13}$ cm^{-2} s^{-1}, and an extension of $0.17° \pm 0.04°$. Two potential counterparts are found to be spatially coincident with this source candidate: the magnetar SGR 1900+14 (Mazets et al. 1979) and the SNR G42.8+0.6 (Fuerst et al. 1987). The former has an age $\tau_c = 0.90$ kyr and a spin-down luminosity $\dot{E} = 2.6 \times 10^{34}$ erg s^{-1}. It is assumed to be at a distance 12.5 ± 1.7 kpc (Davies et al. 2009) based on an association of the magnetar with a massive star cluster (Wachter et al. 2008). SGR 1900+14 has similar properties to those of another magnetar, SGR 1806−20, that is associated with the VHE source HESS J1808−204 (H.E.S.S. Collaboration 2018a). It underwent a major burst of soft γ-ray emission in 1998 (Hurley et al. 1999; Frail et al. 1999) and, similar to SGR 1806−20, it might also be emitting VHE γ-rays. Little is known about SNR G42.8+0.6. The centroid of the VHE emission is marginally coincident with the magnetar, while the bulk of the emission overlaps the northeastern half of the SNR shell.

6. Summary and conclusions

The H.E.S.S. Collaboration has completed its Galactic plane survey, which is an observation and analysis program that spanned over a decade. This paper presents the final results of the survey. The four-telescope H.E.S.S. Phase I array was used for the observations, which features a 5° FoV that is well suited to scanning large regions of the sky like the Galactic plane. The Phase I array has a typical sensitivity to point-like γ-ray sources of 1% Crab Nebula integral flux ($E > 1$ TeV) in less than 25 h.

The H.E.S.S. Collaboration added a fifth, larger telescope to the array in 2012 (H.E.S.S. Phase II) to extend its sensitivity to lower energies as well as its ability to rapidly reposition to observe transient phenomena. However, it also features a smaller FoV than the four Phase I telescopes, making it much less suited for scanning large regions. In addition, the HGPS had improved the uniformity of its exposure and achieved a target sensitivity of 2% Crab flux in the inner Galaxy. Primarily for these reasons, as well as the diminishing gains stemming from source significance scaling approximately as the square root of livetime, the H.E.S.S. Collaboration in 2013 decided not to continue the HGPS observation program.

First early results from the HGPS were published in 2005 (Aharonian et al. 2005a). The observations at the time amounted to just 120 h yet led to the detection of ten VHE γ-ray sources

in the inner Galaxy, eight of which were not previously known. Further results followed in 2006 (Aharonian et al. 2006a), using 230 h of data and discovering additional four γ-ray sources. Since then, we provided the community with periodic updates, which had steadily increasing exposure and additional source discoveries, by releasing new unidentified sources (Aharonian et al. 2008a) and via published conference proceedings (Hoppe 2008b; Chaves et al. 2008a; Chaves 2009; Gast et al. 2011; Deil 2012; Carrigan et al. 2013a,b).

The HGPS data set (Sect. 2) is now over a factor of ten larger than in 2006, comprising 2673 h of observations accumulated over the period 2004 to 2013. These data come from a variety of observations: observations from the initially published surveys, targeted observations of known sources, follow-up observations of newly discovered source candidates, observations to extend the HGPS spatial coverage, and fill-up observations to achieve a more uniform sensitivity across the Galactic plane (Fig. 4). The energy threshold of the HGPS varies with the longitude observed but is typically lower than 0.8 TeV for detections and maps (0.5 TeV for spectral analyses) and as low as 0.4 TeV (0.2 TeV) in many regions, especially the innermost Galaxy (Fig. 2).

Compared to the previous publication, the HGPS was also expanded to cover a much wider range of both longitude and latitude (Fig. 1). In the first Galactic quadrant, the HGPS now extends in longitude from the Galactic center to nearly $\ell = 65°$, the northern limit of visibility from the southern-hemisphere H.E.S.S. site. In the fourth Galactic quadrant, the HGPS coverage is continuous and even extends beyond Vela to $\ell = 250°$ in the third quadrant. In latitude, the coverage varies but is generally $b = \pm 3°$ and as large as $b = \pm 5°$ in some regions to explore areas of particular interest off the plane. The point-source sensitivity is better than 2% Crab along the Galactic plane ($b = 0°$) over most of the longitudes covered by the HGPS (Figs. 4 and 11). However, the flux sensitivity varies significantly owing to the mix of observations comprising the HGPS. It is better than 1% Crab in numerous regions but at a more modest level of 2–10% Crab off-plane. The HGPS achieves the best sensitivity at the Galactic center, reaching 0.3% of the Crab flux.

To ensure robust results, the HGPS relies on results that agree between two independent software frameworks (chains; Sect. 2.3) used to calibrate raw Cherenkov data as well as reconstruct and analyze the γ-ray images and spectra. The primary software chain used the Hillas method for event reconstruction, and an event classification method using boosted decision trees. The secondary (cross-check) chain uses an alternative event reconstruction and classification based on EAS models, returning results that are in very good agreement globally although there are some variations on a source-by-source basis (discussed in Sect. 5.4). MC simulations provide the instrument response functions that describe the performance of the instrument. The mean angular resolution of H.E.S.S. (68% containment radius of the PSF) is ~0.08° and varies by approximately 10% across the survey region.

We have generated a number of sky maps (images; Sect. 3), which are public data products[13] and also form the basis for the HGPS source catalog construction. To accumulate sufficient signal and search for γ-ray emission of different sizes, we generated three different sets of maps with events spatially correlated over radii of 0.1° (point-like), 0.2°, and 0.4°, respectively. To subtract background from hadronic CRs passing γ-ray selections in the FoV, we developed an adaptive version of the classic ring background method that is more flexible and can compensate for large exclusion regions that minimize signal contaminating background regions (Sect. 3.3). The release maps are for statistical significance, flux, flux error, upper limit and sensitivity (see Appendix A.1).

To detect and characterize the VHE γ-ray sources, we developed a semi-automatic analysis pipeline to construct a source catalog (see Sect. 4). To disentangle individual γ-ray sources in complex regions of overlapping emission, we implemented morphological modeling based on two-dimensional maximum-likelihood estimation. We fit the γ-ray excess by two-dimensional symmetric Gaussian components, keeping components with TS > 30. To arrive at the HGPS catalog, Gaussian components that that did not correspond to a clear emission peak in the main and cross-check analysis were rejected. Some components that strongly overlapped were merged into a single source for which position, extension, and flux were characterized by the moments of the multi-Gaussian emission model. In this process, it was necessary to model the underlying large-scale γ-ray emission along the Galactic plane to improve the modeling of the discrete sources (Sect. 4.6). We chose to use an empirical model derived with a sliding window method, 20° wide in longitude and Gaussian in latitude, whose Gaussian center, amplitude, and width were fit to the excess outside exclusion regions. We calculated source spectra using the reflected region background method when possible, fitting PL spectral models and determining the best-fit normalization and spectral index. Flux information is also available from the aforementioned maps albeit assuming a spectral index of $\Gamma = 2.3$.

The HGPS source catalog includes 78 sources of VHE γ-rays. Of these, 64 were detected with the HGPS pipeline analysis. For completeness, the catalog includes an additional 14 H.E.S.S. sources from regions excluded from the HGPS pipeline, for example, because of their complexity, such as the Galactic center region and sources with shell-like morphologies. H.E.S.S. has previously published the discovery of most of the HGPS sources, although in many cases the available observation time used for the HGPS analysis is considerably larger. Of the total 78 sources, 16 are new discoveries published here for the first time. Five of these new sources are firmly identified objects: HESS J1554−550 and HESS J1849−000 are PWNe (Sects. 5.6.5 and 5.6.15), and HESS J1119−614, HESS J1833−105, and HESS J1846−029 are composite SNRs (Sects. 5.6.1, 5.6.10, and 5.6.13). Three more of the new sources are spatially coincident with HE γ-ray pulsars, recently discovered in *Fermi*-LAT data, and are thus plausible PWN candidates.

The HGPS sources have diverse characteristics (Sect. 5). Apart from the shell-like sources, most source morphologies are generally well-modeled as symmetric two-dimensional Gaussians, but their sizes range from point-like ($\lesssim$0.1°) to 0.6° (Fig. 13). Their fluxes cover a wide range as well from 0.6% Crab to 103% Crab of which the majority are in the range 1–20% Crab (Fig. 13). The cumulative $\log N - \log S$ distribution above 10% Crab (containing 32 sources) is well described by a power law of slope -1.3 ± 0.2 (Fig. 15), matching the expectation of a power law of slope -1 from a population of equal-luminosity sources homogeneously distributed in the Galactic disk. Below 10% Crab, the HGPS source catalog is incomplete and can only provide a lower limit on the true number of fainter VHE sources (70 above 1% Crab). Spectral indices range from hard ($\Gamma \approx 2.0$) to very soft ($\Gamma \approx 3.0$) in an approximately normal distribution centered at 2.4 ± 0.3 (Fig. 14). The VHE sources cluster narrowly along the Galactic plane (median $b = -0.20°$, with a

[13] https://www.mpi-hd.mpg.de/hfm/HESS/hgps

spread of 0.51°), in good agreement with the distributions of SNRs, energetic pulsars, molecular gas, and HE γ-ray sources (Fig. 11). Their distribution in longitude (Fig. 12) shows a general correlation with molecular gas.

To study the origin of the VHE γ-rays, we performed a systematic search to associate the HGPS sources with known or suspected VHE source classes, based largely on spatial compatibility with objects in the SNR and PWN catalog SNRcat, the ATNF pulsar catalog, and the *Fermi*-LAT 3FGL and 2FHL catalogs (Sect. 5.1). By comparing the HGPS catalog to plausible MWL counterpart catalogs, we come to one of the main conclusions of the HGPS program: the majority (67, or 86%) of the HGPS sources are associated with at least one astronomical object that could potentially account for the production of γ-rays at TeV energies. The unassociated sources (11, 14%) are not necessarily dark, i.e., emitting exclusively in the VHE domain; it is also possible that their counterparts were missed by our association procedure. In short, most HGPS sources have either firm associations, plausible or potential counterparts in other wavelength regimes. Whether there remains a population of truly dark VHE sources in the HGPS can only be figured out with deeper MWL studies.

We then used additional, stricter criteria, such as shell-like morphology or variability, to establish firm identifications for 31 sources (Fig. 10). We found the largest identified VHE source class to be PWNe (12 sources, or 39% of identified sources), followed by shell-type SNRs (8, 26%); composite SNRs (8, 26%), where both the interior PWN and SNR shell may contribute to the emission; and high-energy binary systems (3, 10%). At present, only 40% of the HGPS sources can be firmly identified. This is typically due to difficulties resolving ambiguity among competing scenarios involving multiple associated objects in large part because of the large intrinsic sizes of VHE γ-ray sources.

The HGPS data set allows for population studies of sources. An early study of 15 globular clusters was published before the HGPS was completed (H.E.S.S. Collaboration 2013). Two further such studies, on the primary Galactic VHE source classes of PWNe and SNRs, are published as companion articles to this paper (H.E.S.S. Collaboration 2018e,l, respectively), together with more specific studies on a number of microquasars (H.E.S.S. Collaboration 2018g) and bow shocks of runaway stars (H.E.S.S. Collaboration 2018c). With the public release of the HGPS catalog along with sky maps, more comprehensive such population studies will become possible.

Further insights into the Galactic VHE source population and diffuse emission in the coming years can be expected. H.E.S.S., *Fermi*-LAT and HAWC are surveying the Milky Way; the analysis methods for the individual gamma-ray data sets, and joint analysis methods combining multiple data sets are improving; and new surveys at lower wavelengths (especially those detecting nonthermal emission in the radio and X-ray bands) will be come available soon. The next major leap forward will be achieved by the Galactic plane survey of the Cherenkov Telescope Observatory (CTA), which will consist of two arrays in the northern and southern hemisphere (The Cherenkov Telescope Array Consortium et al. 2017). The Galactic plane survey is a key science project of CTA, and is planned to cover the whole Galactic plane, over a wider energy band and with better angular resolution and sensitivity compared to HGPS (Dubus et al. 2013; The Cherenkov Telescope Array Consortium et al. 2017).

In conclusion, the additional exposure obtained since 2006, plus significant improvements in analysis and reconstruction methods, allowed us to probe much more of the Galaxy, whether it be more distant sources, fainter nearby sources, or regions never before observed at TeV energies. The HGPS program clearly demonstrates that sources of VHE γ-ray emission are common in the Galaxy and are linked to diverse sites of high-energy particle acceleration.

Acknowledgements. This work made extensive use of gamma-cat[14], SNRcat[15] (Ferrand & Safi-Harb 2012), ATNF[16] (Manchester et al. 2005), SIMBAD[17] (Wenger et al. 2000) and NASA's Astrophysics Data System Bibliographic Services. For data analysis, we made extensive use of the Python packages Gammapy[18] (Donath et al. 2015; Deil et al. 2017), Astropy[19] (Astropy Collaboration et al. 2013) and Sherpa[20] (Freeman et al. 2001), as well as Numpy (Dubois et al. 1996), Scipy (Jones et al. 2001) and Matplotlib (Hunter 2007). The support of the Namibian authorities and the University of Namibia in facilitating the construction and operation of H.E.S.S. is gratefully acknowledged, as is the support by the German Ministry for Education and Research (BMBF), the Max Planck Society, the German Research Foundation (DFG), the French Ministry for Research, the CNRS-IN2P3 and the Astroparticle Interdisciplinary Programme of the CNRS, the U.K. Science and Technology Facilities Council (STFC), the IPNP of the Charles University, the Czech Science Foundation, the Polish Ministry of Science and Higher Education, the South African Department of Science and Technology and National Research Foundation, the University of Namibia, the Innsbruck University, the Austrian Science Fund (FWF), and the Austrian Federal Ministry for Science, Research and Economy, and by the University of Adelaide and the Australian Research Council. We appreciate the excellent work of the technical support staff in Berlin, Durham, Hamburg, Heidelberg, Palaiseau, Paris, Saclay, and in Namibia in the construction and operation of the equipment. This work benefited from services provided by the H.E.S.S. Virtual Organisation, supported by the national resource providers of the EGI Federation.

References

Abdo, A. A., Ackermann, M., Ajello, M., et al. 2009a, Science, 325, 840
Abdo, A. A., Ackermann, M., Ajello, M., et al. 2009b, ApJS, 183, 46
Abdo, A. A., Ajello, M., Allafort, A., et al. 2013, ApJS, 208, 17
Abeysekara, A. U., Albert, A., Alfaro, R., et al. 2017, ApJ, 843, 40
Abramowski, A., Acero, F., Aharonian, F., et al. 2012a, A&A, 548, A38
Abramowski, A., Acero, F., Aharonian, F., et al. 2012b, A&A, 537, A114
Abramowski, A., Aharonian, F., Ait Benkhali, F., et al. 2014a, Phys. Rev. D, 90, 122007
Abramowski, A., Aharonian, F., Ait Benkhali, F. A., et al. 2014b, MNRAS, 439, 2828
Acciari, V. A., Aliu, E., Arlen, T., et al. 2010, ApJ, 719, L69
Acero, F., Aharonian, F., Akhperjanian, A. G., et al. 2010a, A&A, 516, A62
Acero, F., Aharonian, F., Akhperjanian, A. G., et al. 2010b, MNRAS, 402, 1877
Acero, F., Djannati-Ataï, A., Förster, A., et al. 2012, ArXiv e-prints [arXiv:1201.0481]
Acero, F., Ackermann, M., Ajello, M., et al. 2013, ApJ, 773, 77
Acero, F., Ackermann, M., Ajello, M., et al. 2015, ApJS, 218, 23
Acero, F., Ackermann, M., Ajello, M., et al. 2016, ApJS, 224, 8
Ackermann, M., Ajello, M., Baldini, L., et al. 2011, ApJ, 726, 35
Ackermann, M., Ajello, M., Atwood, W. B., et al. 2016, ApJS, 222, 5
Aharonian, F. A. 1991, Ap&SS, 180, 305
Aharonian, F. A., & Atoyan, A. M. 1996, A&A, 309, 917
Aharonian, F. A., Atoyan, A. M., & Kifune, T. 1997, MNRAS, 291, 162
Aharonian, F. A., Akhperjanian, A. G., Beilicke, M., et al. 2002, A&A, 395, 803
Aharonian, F., Akhperjanian, A. G., Aye, K.-M., et al. 2004a, Astropart. Phys., 22, 109
Aharonian, F. A., Akhperjanian, A. G., Aye, K.-M., et al. 2004b, Nature, 432, 75
Aharonian, F., Akhperjanian, A. G., Aye, K.-M., et al. 2005a, Science, 307, 1938
Aharonian, F., Akhperjanian, A. G., Aye, K.-M., et al. 2005b, A&A, 432, L25
Aharonian, F., Akhperjanian, A. G., Aye, K.-M., et al. 2005c, A&A, 442, 1
Aharonian, F., Akhperjanian, A. G., Aye, K.-M., et al. 2005d, A&A, 435, L17
Aharonian, F., Akhperjanian, A. G., Bazer-Bachi, A. R., et al. 2005e, A&A, 437, L7

[14] https://github.com/gammapy/gamma-cat
[15] http://www.physics.umanitoba.ca/snr/SNRcat
[16] http://www.atnf.csiro.au/research/pulsar/psrcat
[17] http://simbad.u-strasbg.fr/simbad
[18] https://github.com/gammapy/gammapy
[19] http://www.astropy.org
[20] http://cxc.cfa.harvard.edu/sherpa

Aharonian, F., Akhperjanian, A. G., Bazer-Bachi, A. R., et al. 2006a, ApJ, 636, 777
Aharonian, F., Akhperjanian, A. G., Bazer-Bachi, A. R., et al. 2006b, A&A, 457, 899
Aharonian, F., Akhperjanian, A. G., Bazer-Bachi, A. R., et al. 2006c, A&A, 460, 743
Aharonian, F., Akhperjanian, A. G., Bazer-Bachi, A. R., et al. 2006d, A&A, 448, L43
Aharonian, F., Akhperjanian, A. G., Bazer-Bachi, A. R., et al. 2006e, A&A, 456, 245
Aharonian, F., Akhperjanian, A. G., Bazer-Bachi, A. R., et al. 2006f, A&A, 460, 365
Aharonian, F. A., Akhperjanian, A. G., Bazer-Bachi, A. R., et al. 2007, A&A, 469, L1
Aharonian, F., Akhperjanian, A. G., Barres de Almeida, U., et al. 2008a, A&A, 477, 353
Aharonian, F., Akhperjanian, A. G., Barres de Almeida, U., et al. 2008b, A&A, 490, 685
Aharonian, F., Akhperjanian, A. G., Barres de Almeida, U., et al. 2008c, A&A, 483, 509
Aharonian, F., Akhperjanian, A. G., Bazer-Bachi, A. R., et al. 2008d, A&A, 481, 401
Aharonian, F., Akhperjanian, A. G., Anton, G., et al. 2009, A&A, 499, 723
Akiyama, K., Stawarz, Ł., Tanaka, Y. T., et al. 2016, ApJ, 823, L26
Aleksić, J., Alvarez, E. A., Antonelli, L. A., et al. 2012, A&A, 541, A13
Aliu, E., Archambault, S., Aune, T., et al. 2014a, ApJ, 780, 168
Aliu, E., Archambault, S., Aune, T., et al. 2014b, ApJ, 787, 166
Angüner, E. O., Aharonian, F., Bordas, P., et al. 2017, AIP Conf. Proc., 1792, 040024
Antonopoulou, D., Vasilopoulos, G., & Espinoza, C. M. 2016, The Astronomer's Telegram, 9282
Astropy Collaboration, Robitaille, T. P., Tollerud, E. J., et al. 2013, A&A, 558, A33
Bamba, A., Yamazaki, R., Kohri, K., et al. 2009, ApJ, 691, 1854
Bamba, A., Terada, Y., Hewitt, J., et al. 2016, ApJ, 818, 63
Berge, D., Funk, S., & Hinton, J. 2007, A&A, 466, 1219
Bernlöhr, K. 2008, Astropart. Phys., 30, 149
Bietenholz, M. F., & Bartel, N. 2008, MNRAS, 386, 1411
Blum, R. D., Damineli, A., & Conti, P. S. 1999, AJ, 117, 1392
Bocchino, F., Parmar, A. N., Mereghetti, S., et al. 2001, A&A, 367, 629
Bocchino, F., van der Swaluw, E., Chevalier, R., & Bandiera, R. 2005, A&A, 442, 539
Bolz, O. 2004, PhD thesis, Ruprecht-Karls-Universität Heidelberg
Brogan, C. L., Gelfand, J. D., Gaensler, B. M., Kassim, N. E., & Lazio, T. J. W. 2006, ApJ, 639, L25
Burgay, M., Bailes, M., Bates, S. D., et al. 2013, MNRAS, 433, 259
Calabretta, M. R., & Greisen, E. W. 2002, A&A, 395, 1077
Camilo, F., Kaspi, V. M., Lyne, A. G., et al. 2000, ApJ, 541, 367
Camilo, F., Ransom, S. M., Gaensler, B. M., et al. 2006, ApJ, 637, 456
Carrigan, S., Brun, F., Chaves, R. C. G., et al. 2013a, ArXiv e-prints [arXiv:1307.4690]
Carrigan, S., Brun, F., Chaves, R. C. G., et al. 2013b, ArXiv e-prints [arXiv:1307.4868]
Cash, W. 1979, ApJ, 228, 939
Caswell, J. L., McClure-Griffiths, N. M., & Cheung, M. C. M. 2004, MNRAS, 352, 1405
Chaves, R. C. G. 2009, ArXiv e-prints [arXiv:0907.0768]
Chaves, R. C. G., de Oña Wilhemi, E., & Hoppe, S. 2008a, in AIP Conf. Ser., eds. F. A. Aharonian, W. Hofmann, & F. Rieger, 1085, 219
Chaves, R. C. G., Renaud, M., Lemoine-Goumard, M., & Goret, P. 2008b, AIP Conf. Ser., 1085, 372
Clifton, T. R., & Lyne, A. G. 1986, Nature, 320, 43
Cordes, J. M., & Lazio, T. J. W. 2002, ArXiv e-prints [arXiv:astro-ph/0207156]
Cui, Y., Pühlhofer, G., & Santangelo, A. 2016, A&A, 591, A68
Dame, T. M., Hartmann, D., & Thaddeus, P. 2001, ApJ, 547, 792
Davies, B., Figer, D. F., Kudritzki, R.-P., et al. 2009, ApJ, 707, 844
de Jager, O. C., & Djannati-Ataï, A. 2009, in Astrophysics and Space Science Library, 357, ed. W. Becker, 451
de Jager, O. C., Harding, A. K., Baring, M. G., & Mastichiadis, A. 1995, International Cosmic Ray Conference, 2, 528
de los Reyes, R., Zajczyk, A., Chaves, R. C. G., & H.E.S.S. Collaboration 2012, ArXiv e-print [arXiv:1205.0719]
de Naurois, M., & Rolland, L. 2009, Astropart. Phys., 32, 231
Deil, C. 2012, in The Spectral Energy Distribution of Galaxies - SED 2011, eds. R. J. Tuffs, & C. C. Popescu, IAU Symp., 284, 365
Deil, C., Zanin, R., Lefaucheur, J., et al. 2017, ArXiv e-prints [arXiv:1709.01751]
Djannati-Ataï, A., de Jager, O. C., Terrier, R., Gallant, Y. A., & Hoppe, S. 2008, International Cosmic Ray Conference, 2, 823
Djannati-Ataï, A., Marandon, V., Chaves, R. C. G., et al. 2009, HESS discovery of VHE gamma-ray emission of a remarkable young composite SNR, Online presentations from the Workshop on Supernova Remnants and Pulsar Wind Nebulae in the Chandra Era, http://cxc.harvard.edu/cdo/snr09/program.html
Donath, A., Deil, C., Arribas, M. P., et al. 2015, Proc. ICRC2015, 789
Drury, L. O., Aharonian, F. A., & Voelk, H. J. 1994, A&A, 287, 959
Dubner, G. M., Holdaway, M., Goss, W. M., & Mirabel, I. F. 1998, AJ, 116, 1842
Dubois, P. F., Hinsen, K., & Hugunin, J. 1996, Comput. Phys., 10
Dubus, G., Contreras, J. L., Funk, S., et al. 2013, Astropart. Phys., 43, 317
Eger, P., Rowell, G., Kawamura, A., et al. 2011, A&A, 526, A82
Ferrand, G., & Safi-Harb, S. 2012, Adv. Space Res., 49, 1313
Fiasson, A., Marandon, V., Chaves, R. C. G., Tibolla, O., & H.E.S.S. Collaboration 2009, International Cosmic Ray Conference, http://icrc2009.uni.lodz.pl/proc/pdf/icrc0889.pdf
Fomin, V. P., Stepanian, A. A., Lamb, R. C., et al. 1994, Astropart Phys., 2, 137
Frail, D. A., Cordes, J. M., Hankins, T. H., & Weisberg, J. M. 1991, ApJ, 382, 168
Frail, D. A., Kulkarni, S. R., & Bloom, J. S. 1999, Nature, 398, 127
Freeman, P., Doe, S., & Siemiginowska, A. 2001, in SPIE Conf. Ser., eds. J. -L. Starck, & F. D. Murtagh, 4477, 76
Fuerst, E., Reich, W., Reich, P., Handa, T., & Sofue, Y. 1987, A&AS, 69, 403
Funk, S., Hinton, J. A., Moriguchi, Y., et al. 2007, A&A, 470, 249
Gabici, S., & Montmerle, T. 2015, International Cosmic Ray Conference, 29
Gabici, S., Aharonian, F. A., & Blasi, P. 2007, Ap&SS, 309, 365
Gaensler, B. M., & Slane, P. O. 2006, ARA&A, 44, 17
Gaensler, B. M., Arons, J., Kaspi, V. M., et al. 2002, ApJ, 569, 878
Gast, H., Brun, F., Carrigan, S., et al. 2011, International Cosmic Ray Conference, 7, 158
Gavriil, F. P., Gonzalez, M. E., Gotthelf, E. V., et al. 2008, Science, 319, 1802
Gonzalez, M., & Safi-Harb, S. 2003, ApJ, 591, L143
Gotthelf, E. V., & Halpern, J. P. 2009, ApJ, 700, L158
Gotthelf, E. V., Halpern, J. P., Terrier, R., & Mattana, F. 2011, ApJ, 729, L16
Gotthelf, E. V., Tomsick, J. A., Halpern, J. P., et al. 2014, ApJ, 788, 155
Göğüş, E., Lin, L., Kaneko, Y., et al. 2016, ApJ, 829, L25
Green, D. A. 2014, Bull. Astron. Soc. India, 42, 47
Gupta, Y., Mitra, D., Green, D. A., & Acharyya, A. 2005, Current Science, 89, 853
Hahn, J., de los Reyes, R., Bernlöhr, K., et al. 2014, Astropart. Phys., 54, 25
Helfand, D. J., Velusamy, T., Becker, R. H., & Lockman, F. J. 1989, ApJ, 341, 151
Helfand, D. J., Becker, R. H., White, R. L., Fallon, A., & Tuttle, S. 2006, AJ, 131, 2525
H.E.S.S. Collaboration (Abramowski, A., et al.) 2011a, A&A, 531, A81
H.E.S.S. Collaboration (Abramowski, A., et al.) 2011b, A&A, 533, A103
H.E.S.S. Collaboration (Abramowski, A., et al.) 2012, A&A, 548, A46
H.E.S.S. Collaboration (Abramowski, A., et al.) 2013, A&A, 551, A26
H.E.S.S. Collaboration (Abramowski, A., et al.) 2014a, A&A, 562, L4
H.E.S.S. Collaboration (Abramowski, A., et al.) 2014b, A&A, 562, A40
H.E.S.S. Collaboration (Abramowski, A., et al.) 2015a, A&A, 574, A100
H.E.S.S. Collaboration (Abramowski, A., et al.) 2015b, A&A, 575, A81
H.E.S.S. Collaboration (Abramowski, A., et al.) 2015c, A&A, 577, A131
H.E.S.S. Collaboration (Abramowski, A., et al.) 2015d, A&A, 574, A27
H.E.S.S. Collaboration (Abramowski, A., et al.) 2015e, Science, 347, 406
H.E.S.S. Collaboration (Abramowski, A., et al.) 2016, Nature, 531, 476
H.E.S.S. Collaboration (Abdalla, H, et al.) 2018a, A&A, 612, A11 (H.E.S.S. SI)
H.E.S.S. Collaboration (Abdalla, H., et al.) 2018b, A&A, 612, A7 (H.E.S.S. SI)
H.E.S.S. Collaboration (Abdalla, H., et al.) 2018c, A&A, 612, A12 (H.E.S.S. SI)
H.E.S.S. Collaboration (Abdalla, H., et al.) 2018d, A&A, 612, A5 (H.E.S.S. SI)
H.E.S.S. Collaboration (Abdalla, H., et al.) 2018e, A&A, 612, A2 (H.E.S.S. SI)
H.E.S.S. Collaboration (Abdalla, H., et al.) 2018f, A&A, 612, A6 (H.E.S.S. SI)
H.E.S.S. Collaboration (Abdalla, H., et al.) 2018g, A&A, 612, A10 (H.E.S.S. SI)
H.E.S.S. Collaboration (Abdalla, H., et al.) 2018h, A&A, 612, A9 (H.E.S.S. SI)
H.E.S.S. Collaboration (Abramowski, A., et al.) 2018i, A&A, 612, A4 (H.E.S.S. SI)
H.E.S.S. Collaboration (Abdalla, H., et al.) 2018j, A&A, 612, A8 (H.E.S.S. SI)
H.E.S.S. Collaboration (Abdalla, H., et al.) 2018k, A&A, 612, A13 (H.E.S.S. SI)
H.E.S.S. Collaboration (Abdalla, H., et al.) 2018l, A&A, 612, A3 (H.E.S.S. SI)
H.E.S.S. Collaboration (Abdalla, H., et al.) 2018m, A&A, 612, A14 (H.E.S.S. SI)
Hinton, J. A., & Hofmann, W. 2009, ARA&A, 47, 523
Hobbs, G., Faulkner, A., Stairs, I. H., et al. 2004a, MNRAS, 352, 1439
Hobbs, G., Lyne, A. G., Kramer, M., Martin, C. E., & Jordan, C. 2004b, MNRAS, 353, 1311
Hofverberg, P., Chaves, R. C. G., Fiasson, A., et al. 2010, in 25th Texas Symposium on Relativistic Astrophysics, 196
Holder, J. 2009, ArXiv e-prints [arXiv:0907.3918]

Hoppe, S. 2008a, PhD thesis, Universität Heidelberg, Max-Planck-Institut für Kernphysik
Hoppe, S. 2008b, International Cosmic Ray Conference, 2, 579
Hunter, J. D. 2007, Comput. Sci. Eng., 9, 90
Hurley, K., Cline, T., Mazets, E., et al. 1999, Nature, 397, 41
Johanson, A. K., & Kerton, C. R. 2009, AJ, 138, 1615
Johnston, S., & Galloway, D. 1999, MNRAS, 306, L50
Jones, E., Oliphant, T., Peterson, P., et al. 2001, SciPy: Open Source Scientific Tools for Python, https://www.scipy.org
Kang, J.-H., & Koo, B.-C. 2007, ApJS, 173, 85
Kang, J.-H., Koo, B.-C., & Salter, C. 2012, AJ, 143, 75
Kargaltsev, O., & Pavlov, G. G. 2008, in 40 Years of Pulsars: Millisecond Pulsars, Magnetars and More, eds. C. Bassa, Z. Wang, A. Cumming, & V. M. Kaspi, AIP Conf. Ser., 983, 171
Kargaltsev, O., Rangelov, B., & Pavlov, G. G. 2013, ArXiv e-prints [arXiv:1305.2552]
Kesteven, M. J. L. 1968, Aust. J. Phys., 21, 369
Koo, B.-C., Lee, J.-J., Seward, F. D., & Moon, D.-S. 2005, ApJ, 633, 946
Koo, B.-C., Kang, J.-H., & Salter, C. J. 2006, ApJ, 643, L49
Koralesky, B., Frail, D. A., Goss, W. M., Claussen, M. J., & Green, A. J. 1998, AJ, 116, 1323
Kosack, K., Chaves, R. C. G., & Acero, F. 2011, International Cosmic Ray Conference, 7, 76
Krivonos, R., Tsygankov, S., Lutovinov, A., et al. 2012, A&A, 545, A27
Kuiper, L., & Hermsen, W. 2015, MNRAS, 449, 3827
Kumar, H. S., & Safi-Harb, S. 2008, ApJ, 678, L43
Kumar, H. S., Safi-Harb, S., & Gonzalez, M. E. 2012, ApJ, 754, 96
Leahy, D. A., & Tian, W. W. 2008, A&A, 480, L25
Lemoine-Goumard, M., Ferrara, E., Grondin, M.-H., Martin, P., & Renaud, M. 2011, Mem. Soc. Astron. Italiana, 82, 739
Leroy, N. 2004, PhD thesis, Ecole Polytechnique
Li, T.-P., & Ma, Y.-Q. 1983, ApJ, 272, 317
Livingstone, M. A., Kaspi, V. M., Gotthelf, E. V., & Kuiper, L. 2006, ApJ, 647, 1286
Manchester, R. N., Lyne, A. G., Camilo, F., et al. 2001, MNRAS, 328, 17
Manchester, R. N., Hobbs, G. B., Teoh, A., & Hobbs, M. 2005, AJ, 129, 1993
Marandon, V., Djannati-Atai, A., Terrier, R., et al. 2008, in AIP Conf. Ser., eds. F. A. Aharonian, W. Hofmann, & F. Rieger, 1085, 320
Marelli, M., Harding, A., Pizzocaro, D., et al. 2014, ApJ, 795, 168
Mazets, E. P., Golenetskij, S. V., & Guryan, Y. A. 1979, Sov. Astron. Lett., 5, 343
McClure-Griffiths, N. M., Dickey, J. M., Gaensler, B. M., & Green, A. J. 2002, ApJ, 578, 176
Morton, T. D., Slane, P., Borkowski, K. J., et al. 2007, ApJ, 667, 219
Motte, F., Schilke, P., & Lis, D. C. 2003, ApJ, 582, 277
Neronov, A., & Semikoz, D. V. 2010, ArXiv e-prints [arXiv:1011.0210]
Ng, C.-Y., Slane, P. O., Gaensler, B. M., & Hughes, J. P. 2008, ApJ, 686, 508
Nguyen Luong, Q., Motte, F., Schuller, F., et al. 2011, A&A, 529, A41
Ohm, S., van Eldik, C., & Egberts, K. 2009, Astropart. Phys., 31, 383
Paredes, J. M., Ishwara-Chandra, C. H., Bosch-Ramon, V., et al. 2014, A&A, 561, A56
Parent, D., Kerr, M., den Hartog, P. R., et al. 2011, ApJ, 743, 170
Pence, W. D., Chiappetti, L., Page, C. G., Shaw, R. A., & Stobie, E. 2010, A&A, 524, A42
Peter, D., Domainko, W., Sanchez, D. A., van der Wel, A., & Gässler, W. 2014, A&A, 571, A41
Piron, F., Djannati-Atai, A., Punch, M., et al. 2001, A&A, 374, 895
Planck Collaboration X. 2016, A&A, 594, A10
Ptuskin, V. S., & Zirakashvili, V. N. 2005, A&A, 429, 755
Ray, P. S., Kerr, M., Parent, D., et al. 2011, ApJS, 194, 17
Reich, W. 1982, A&A, 106, 314
Reimer, A., Pohl, M., & Reimer, O. 2006, ApJ, 644, 1118
Renaud, M., Goret, P., & Chaves, R. C. G. 2008, in AIP Conf. Ser., eds. F. A. Aharonian, W. Hofmann, & F. Rieger, 1085, 281
Roberts, M. S. E., Gotthelf, E. V., Halpern, J. P., Brogan, C. L., & Ransom, S. M. 2007, in WE-Heraeus Seminar on Neutron Stars and Pulsars 40 years after the Discovery, eds. W. Becker, & H. H. Huang, 24
Rolke, W. A., López, A. M., & Conrad, J. 2005, Nucl. Instrum. Meth. Phys. Res. A, 551, 493
Romero, G. E. 2010, Mem. Soc. Astron. It., 81, 181
Russeil, D. 2003, A&A, 397, 133
Safi-Harb, S., & Kumar, H. S. 2008, ApJ, 684, 532
Safi-Harb, S., Harrus, I. M., Petre, R., et al. 2001, ApJ, 561, 308
Shahinyan, K., & VERITAS Collaboration 2017, AIP Conf. Ser., 1792, 040036
Sheidaei, F. 2011, International Cosmic Ray Conference, 7, 244
Slane, P., Bykov, A., Ellison, D. C., Dubner, G., & Castro, D. 2015, Space Sci. Rev., 188, 187
Stewart, I. M. 2009, A&A, 495, 989
Stil, J. M., Taylor, A. R., Dickey, J. M., et al. 2006, AJ, 132, 1158
Straal, S. M., Gabányi, K. É., van Leeuwen, J., et al. 2016, ApJ, 822, 117
Stycz, K. 2016, PhD thesis, Humboldt-Universität Berlin
Su, Y., Chen, Y., Yang, J., et al. 2009, ApJ, 694, 376
Sugizaki, M., Mitsuda, K., Kaneda, H., et al. 2001, ApJS, 134, 77
Sun, M., Wang, Z.-r., & Chen, Y. 1999, ApJ, 511, 274
Tam, P. H. T., Wagner, S. J., Tibolla, O., & Chaves, R. C. G. 2010, A&A, 518, A8
Tanaka, S. J., & Takahara, F. 2011, ApJ, 741, 40
Temim, T., Slane, P., Gaensler, B. M., Hughes, J. P., & Van Der Swaluw, E. 2009, ApJ, 691, 895
Temim, T., Slane, P., Arendt, R. G., & Dwek, E. 2012, ApJ, 745, 46
Temim, T., Slane, P., Castro, D., et al. 2013, ApJ, 768, 61
Temim, T., Slane, P., Kolb, C., et al. 2015, ApJ, 808, 100
Terrier, R., Djannati-Atai, A., Hoppe, S., et al. 2008a, in AIP Conf. Ser., eds. F. A. Aharonian, W. Hofmann, & F. Rieger, 1085, 316
Terrier, R., Mattana, F., Djannati-Atai, A., et al. 2008b, in AIP Conf. Ser., eds. F. A. Aharonian, W. Hofmann, & F. Rieger, 1085, 312
The Cherenkov Telescope Array Consortium, Acharya, B. S., Agudo, I., et al. 2017, ArXiv e-prints [arXiv:1709.07997]
The Fermi-LAT Collaboration 2017, ApJS, 232, 18
Tian, W. W., & Leahy, D. A. 2008, MNRAS, 391, L54
Torres, D. F., Cillis, A., Martín, J., & de Oña Wilhelmi E. 2014, J. High Energy Astrophys., 1, 31
Ueno, M., Bamba, A., Koyama, K., & Ebisawa, K. 2003, ApJ, 588, 338
Vallée, J. P. 2014, ApJS, 215, 1
Van Etten, A., Funk, S., & Hinton, J. 2009, ApJ, 707, 1717
Vasisht, G., Gotthelf, E. V., Torii, K., & Gaensler, B. M. 2000, ApJ, 542, L49
Velusamy, T., & Kundu, M. R. 1974, A&A, 32, 375
Voisin, F., Rowell, G., Burton, M. G., et al. 2016, MNRAS, 458, 2813
Wachter, S., Ramirez-Ruiz, E., Dwarkadas, V. V., et al. 2008, Nature, 453, 626
Weinstein, A. 2009, ArXiv e-prints [arXiv:0912.4492]
Weltevrede, P., Johnston, S., & Espinoza, C. M. 2011, MNRAS, 411, 1917
Wenger, M., Ochsenbein, F., Egret, D., et al. 2000, A&AS, 143, 9
Whiteoak, J. B. Z., & Green, A. J. 1996, A&AS, 118, 329
Wilks, S. S. 1938, Ann. Math. Stat., 9, 60
Wilson, A. S., & Weiler, K. W. 1976, A&A, 53, 89
Xu, J., & Zhang, H. 2009, ArXiv e-prints [arXiv:0909.0394]
Younes, G., Archibald, R., Kouveliotou, C., et al. 2016, The Astronomer's Telegram, 9378
Zajczyk, A., Gallant, Y. A., Slane, P., et al. 2012, A&A, 542, A12
Zhou, P., & Chen, Y. 2011, ApJ, 743, 4

[1] Centre for Space Research, North-West University, Potchefstroom 2520, South Africa
[2] Universität Hamburg, Institut für Experimentalphysik, Luruper Chaussee 149, 22761 Hamburg, Germany
[3] Max-Planck-Institut für Kernphysik, PO Box 103980, 69029 Heidelberg, Germany
[4] Dublin Institute for Advanced Studies, 31 Fitzwilliam Place, Dublin 2, Ireland
[5] National Academy of Sciences of the Republic of Armenia, Marshall Baghramian Avenue, 24, 0019 Yerevan, Republic of Armenia
[6] Yerevan Physics Institute, 2 Alikhanian Brothers St., 375036 Yerevan, Armenia
[7] Institut für Physik, Humboldt-Universität zu Berlin, Newtonstr. 15, 12489 Berlin, Germany
[8] University of Namibia, Department of Physics, Private Bag 13301, Windhoek, Namibia
[9] GRAPPA, Anton Pannekoek Institute for Astronomy, University of Amsterdam, Science Park 904, 1098 XH Amsterdam, The Netherlands
[10] Department of Physics and Electrical Engineering, Linnaeus University, 351 95 Växjö, Sweden
[11] Institut für Theoretische Physik, Lehrstuhl IV: Weltraum und Astrophysik, Ruhr-Universität Bochum, 44780 Bochum, Germany
[12] GRAPPA, Anton Pannekoek Institute for Astronomy and Institute of High-Energy Physics, University of Amsterdam, Science Park 904, 1098 XH Amsterdam, The Netherlands
[13] Institut für Astro- und Teilchenphysik, Leopold-Franzens-Universität Innsbruck, 6020 Innsbruck, Austria
[14] School of Physical Sciences, University of Adelaide, Adelaide 5005, Australia

[15] LUTH, Observatoire de Paris, PSL Research University, CNRS, Université Paris Diderot, 5 Place Jules Janssen, 92190 Meudon, France
[16] Sorbonne Universités, UPMC Université Paris 06, Université Paris Diderot, Sorbonne Paris Cité, CNRS, Laboratoire de Physique Nucléaire et de Hautes Energies (LPNHE), 4 place Jussieu, 75252 Paris Cedex 5, France
[17] Laboratoire Univers et Particules de Montpellier, Université Montpellier, CNRS/IN2P3, CC 72, Place Eugène Bataillon, 34095 Montpellier Cedex 5, France
[18] IRFU, CEA, Université Paris-Saclay, 91191 Gif-sur-Yvette, France
[19] Astronomical Observatory, The University of Warsaw, Al. Ujazdowskie 4, 00-478 Warsaw, Poland
[20] Aix Marseille Université, CNRS/IN2P3, CPPM, Marseille, France
[21] Instytut Fizyki Jądrowej PAN, ul. Radzikowskiego 152, 31-342 Kraków, Poland
[22] Funded by EU FP7 Marie Curie, grant agreement No. PIEF-GA-2012-332350
[23] School of Physics, University of the Witwatersrand, 1 Jan Smuts Avenue, Braamfontein, Johannesburg 2050, South Africa
[24] Laboratoire d'Annecy-le-Vieux de Physique des Particules, Université Savoie Mont-Blanc, CNRS/IN2P3, 74941 Annecy-le-Vieux, France
[25] Landessternwarte, Universität Heidelberg, Königstuhl, 69117 Heidelberg, Germany
[26] Université Bordeaux, CNRS/IN2P3, Centre d'Études Nucléaires de Bordeaux Gradignan, 33175 Gradignan, France
[27] Oskar Klein Centre, Department of Physics, Stockholm University, Albanova University Center, 10691 Stockholm, Sweden
[28] Wallenberg Academy Fellow
[29] Institut für Astronomie und Astrophysik, Universität Tübingen, Sand 1, 72076 Tübingen, Germany
[30] Laboratoire Leprince-Ringuet, Ecole Polytechnique, CNRS/IN2P3, 91128 Palaiseau, France
[31] APC, AstroParticule et Cosmologie, Université Paris Diderot, CNRS/IN2P3, CEA/Irfu, Observatoire de Paris, Sorbonne Paris Cité, 10, rue Alice Domon et Léonie Duquet, 75205 Paris Cedex 13, France
[32] Univ. Grenoble Alpes, CNRS, IPAG, 38000 Grenoble, France
[33] Department of Physics and Astronomy, The University of Leicester, University Road, Leicester LE1 7RH, UK
[34] Nicolaus Copernicus Astronomical Center, Polish Academy of Sciences, ul. Bartycka 18, 00-716 Warsaw, Poland
[35] Institut für Physik und Astronomie, Universität Potsdam, Karl-Liebknecht-Strasse 24/25, 14476 Potsdam, Germany
[36] Friedrich-Alexander-Universität Erlangen-Nürnberg, Erlangen Centre for Astroparticle Physics, Erwin-Rommel-Str. 1, 91058 Erlangen, Germany
[37] DESY, 15738 Zeuthen, Germany
[38] Obserwatorium Astronomiczne, Uniwersytet Jagielloński, ul. Orla 171, 30-244 Kraków, Poland
[39] Centre for Astronomy, Faculty of Physics, Astronomy and Informatics, Nicolaus Copernicus University, Grudziadzka 5, 87-100 Torun, Poland
[40] Department of Physics, University of the Free State, PO Box 339, Bloemfontein 9300, South Africa
[41] Heisenberg Fellow (DFG), ITA Universität Heidelberg, Heidelberg, Germany
[42] Department of Physics, Rikkyo University, 3-34-1 Nishi-Ikebukuro, Toshima-ku, Tokyo 171-8501, Japan
[43] Japan Aerospace Exploration Agency (JAXA), Institute of Space and Astronautical Science (ISAS), 3-1-1 Yoshinodai, Chuo-ku, Sagamihara, Kanagawa 229-8510, Japan
[44] Now at The School of Physics, The University of New South Wales, Sydney 2052, Australia
[45] Now at Instituto de Física de São Carlos, Universidade de São Paulo, Av. Trabalhador São-carlense, 400 - CEP 13566-590 São Carlos SP, Brazil
[46] Now at Technische Universität Kaiserslautern, 67663 Kaiserslautern, Germany
[47] Now at I. Physikalisches Institut B, RWTH Aachen University, 52056 Aachen, Germany
[48] Department of Physics and Astronomy, University of Manitoba, Winnipeg MB R3T 2N2, Canada

Appendix A: Online material

In this section, we provide further information about the public data products released in electronic format. We also provide some guidance and caveats regarding the correct use of these products. The HGPS survey maps and source catalog presented in this paper are available for download at the CDS and at `https://www.mpi-hd.mpg.de/hfm/HESS/hgps`

In addition to the figures and tables in this paper, there are a series of HGPS maps and tables available online:

- Figure A.1: HGPS flux map;
- Figures A.2–A.5: Four-panel HGPS significance maps with all VHE sources and MWL associations labeled;
- Table A.7: HGPS catalog source morphology summary;
- Table A.8: HGPS catalog source spectrum summary;
- Table A.9: HGPS catalog source associations.

A.1. Sky maps

Description

Survey maps are released in FITS format (Pence et al. 2010), using a Cartesian (CAR) projection in Galactic coordinates (Calabretta & Greisen 2002). The maps contain the whole HGPS region ($-114° < l < 75°$ and $-5° < b < +5°$), with a binning of 0.02° per pixel corresponding to a total size of 9400×500 pixels. Maps are available for the following quantities:

- Statistical significance (described in Sect. 3.3);
- Flux (described in Sect. 3.4.2);
- 1σ flux error (described in Sect. 3.4.3);
- Flux upper limit (described in Sect. 3.4.3);
- Sensitivity (described in Sect. 3.4.4).

We provide all flux and flux-like quantities as integral photon fluxes above 1 TeV assuming a PL spectrum for the differential flux with an index $\Gamma = 2.3$. Each map is provided for two correlation radii, $R_c = 0.1°$ and 0.2°.

A total of ten files are released (five quantities, each for two R_c), with file names `hgps_map_<quantity>_<radius>deg_v1.fits.gz`, e.g., the significance map with $R_c = 0.2°$ can be found in the file `hgps_map_significance_0.2deg_v1.fits.gz`.

Usage notes and caveats

- Since none of the released flux-derived maps are computed for a point-like source hypothesis, information extracted from these maps should always be used in the context of full containment of the PSF. Otherwise, this could yield incorrect information, for example, a flux upper limit that is too low (optimistic). In particular, since the H.E.S.S. PSF has a size comparable to 0.1°, the maps computed with this correlation radius do not fully contain the PSF. In this case, one only gets roughly 80% of the flux when reading a pixel value at a given position of a point-like source. Those maps should therefore be used with care when extracting a flux value (see also below).
- The released maps are already spatially correlated (oversampled); therefore, pixel values should be read at the corresponding position of interest for a circular region of radius R_c. In the case of a region size between two of the provided R_c values, interpolation could be used as a first approximation. The oversampling also implies that maps should not be used for morphology studies (e.g., production of radial profiles or fitting).
- Some caution should be taken for values in the 0.2° correlation maps where a gradient in exposure is present, since the background is estimated at the center of the ROI and not averaged across it (see Sect. 3.2).
- The significance maps contain, at each position, the statistical significance of the γ-ray excess. This value is not corrected for trials and the large-scale emission component is not taken into account in its computation.
- We recommend assuming a systematic error of 30% on the flux values (see Sect. 4.12).

A.2. Source catalog

Description

The HGPS source catalog (construction described in Sect. 4) and a number of other tables are available as BINTABLE FITS extensions in the `hgps_catalog_v1.fits.gz` file.

An overview of the available tables (including links to the tables in this paper describing the columns in detail) is given in Table A.1. Here is some further information on the content of the tables:

- `HGPS_Sources`: The HGPS catalog, one source per row, identified via the `Source_Name` column, which is in the format `HESS JHHMM±DDd`.
- `HGPS_Gauss_Components`: The HGPS Gaussian component list, one component per row. Reference back to `HGPS_Sources` catalog via the `Source_Name` column (if the component is part of a source).
- `HGPS_Associations`: The HGPS association list, one association per row. Reference back to `HGPS_Sources` catalog via the `Source_Name` column. A given HGPS catalog source can appear zero, one, or multiple times in this table.

Usage notes and caveats

For reasons of reproducibility, we decided to release the complete emission model on which the analysis is based. This includes the full list of Gaussian components and parameters of the large-scale emission model. When working with this data, beware of following usage notes and caveats:

- Some of the components are unstable and are not confirmed by the cross-check analysis. Use the source catalog, not the component list, for studies based on the HGPS.
- For the HGPS catalog, we did not perform detailed per-source systematic error estimates. In general, when using spectra from the HGPS catalog, we recommend assuming a systematic error of 30% on the absolute flux and 0.2 on the spectral index.
- In Fig. 9, there are a few sources where the integral flux estimate differs by more than 30% when using the two methods discussed in this paper. As discussed in Sect. 4.12, the estimate of a source spectrum is affected by the assumed source morphology, diffuse gamma and atmospheric hadronic background model and uncertainties in the instrument response functions. In particular, the integral flux estimate may be uncertain by more than 30% for sources with relatively low significance that are not spatially isolated from other sources. In those cases, one can assume the difference between `Flux_Map` and `Flux_Spec_Int_1TeV` to be a lower limit on the systematic error.

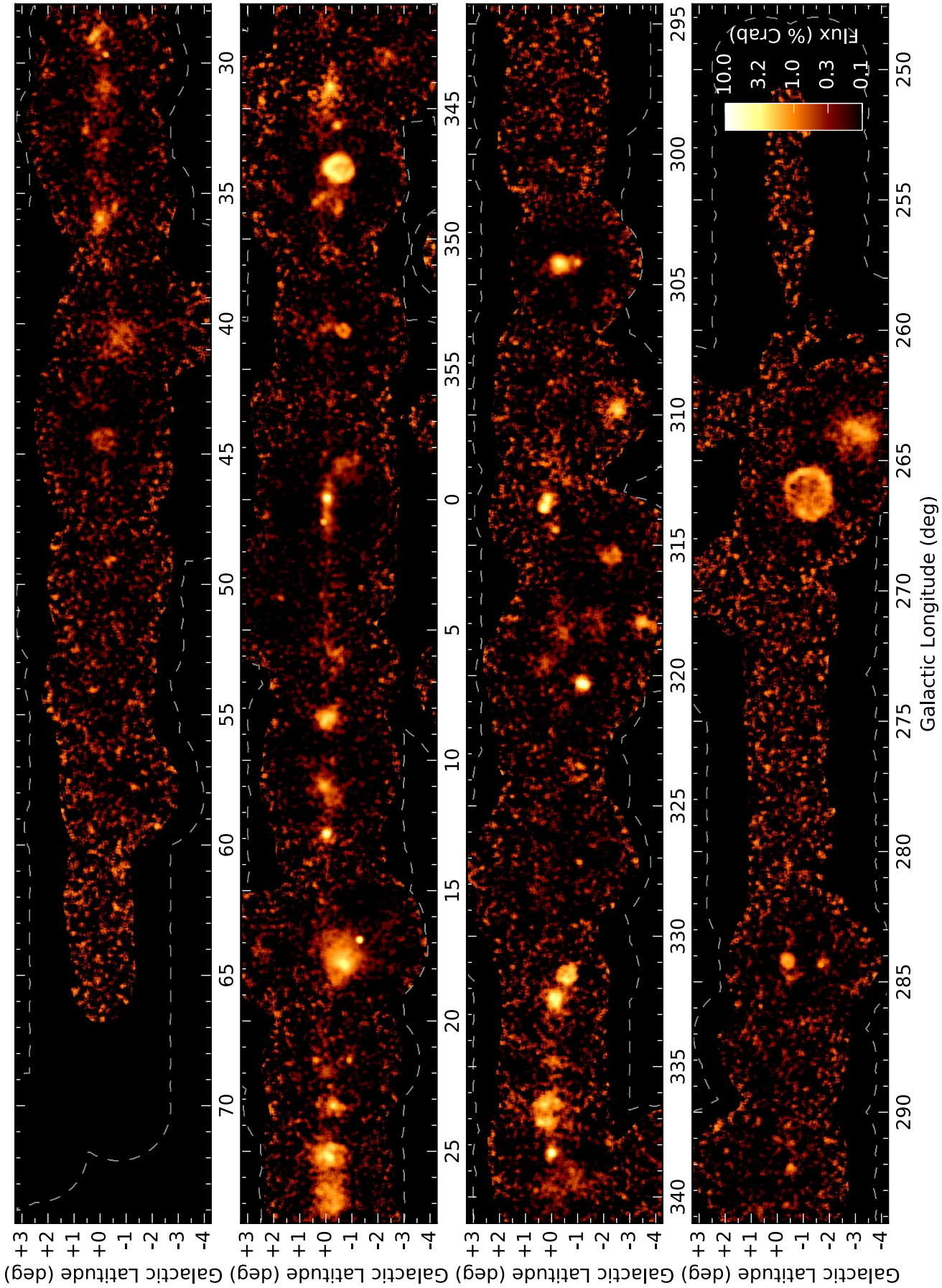

Fig. A.1. Integral flux above 1 TeV using a correlation radius $R_c = 0.1°$ and assuming spectral index $\Gamma = 2.3$, in units of % Crab. The map is only filled where the point-source sensitivity for a 5σ detection (c.f. Fig. 4) is better (lower) than 2.5% Crab.

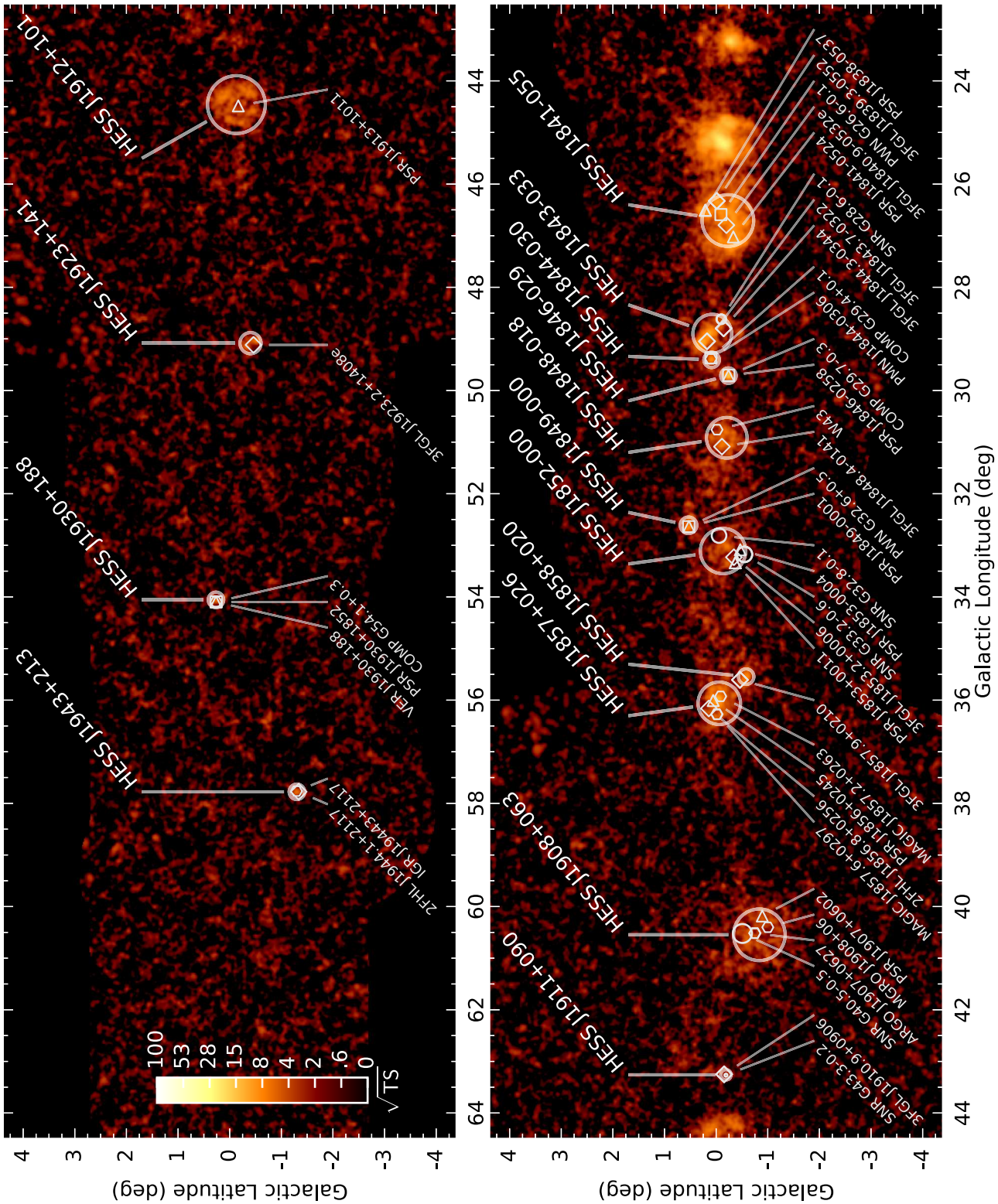

Fig. A.2. HGPS sources and associations in context (1 of 4). The background image shows $\sqrt{\mathrm{TS}}$ of the VHE γ-ray excess in the Galactic plane assuming a point source morphology. All HGPS catalog sources are shown on top with transparent circles that correspond to the measured size of the source. Source names are labeled above the Galactic plane. Associations for the sources are shown with markers in white and corresponding labels. Pulsar (PSR) associations from the ATNF catalog are shown with triangles; SNRs as white circles with the radius representing the size, PWN and Composite (COMP) associations from the SNRcat catalog are marked with squares; associations with *Fermi*-LAT 3FGL and 2FHL sources are shown with diamonds; extra associations are shown with hexagonal markers. 3FGL sources are not labeled when they are identical to the pulsar. 2FHL sources are not labeled, when they are identical to the 3FGL source. The various object categories and the association criteria applied are detailed in Sect. 5.1.

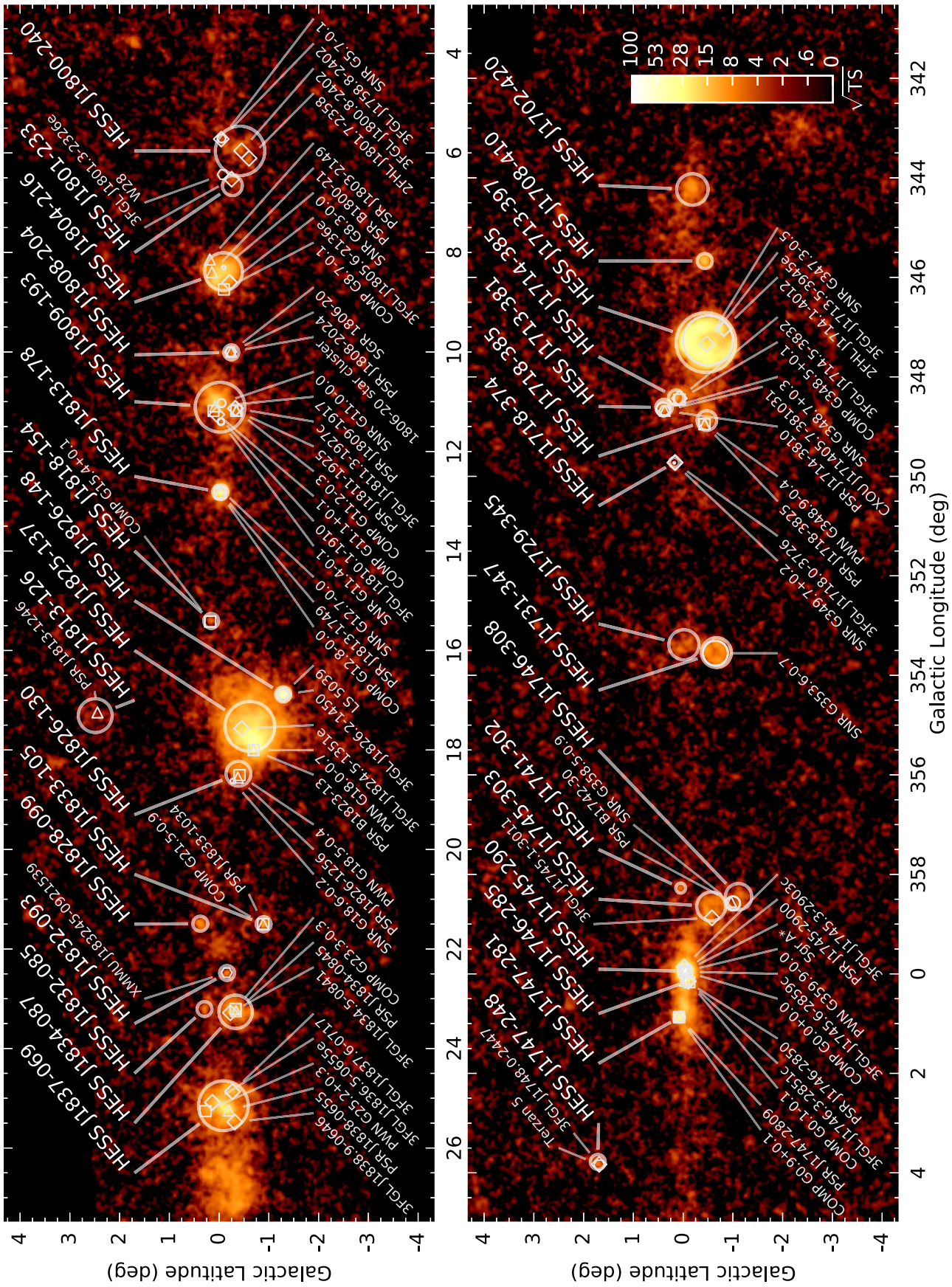

Fig. A.3. HGPS in a MWL context (2 of 4). Fig. A.2 continued.

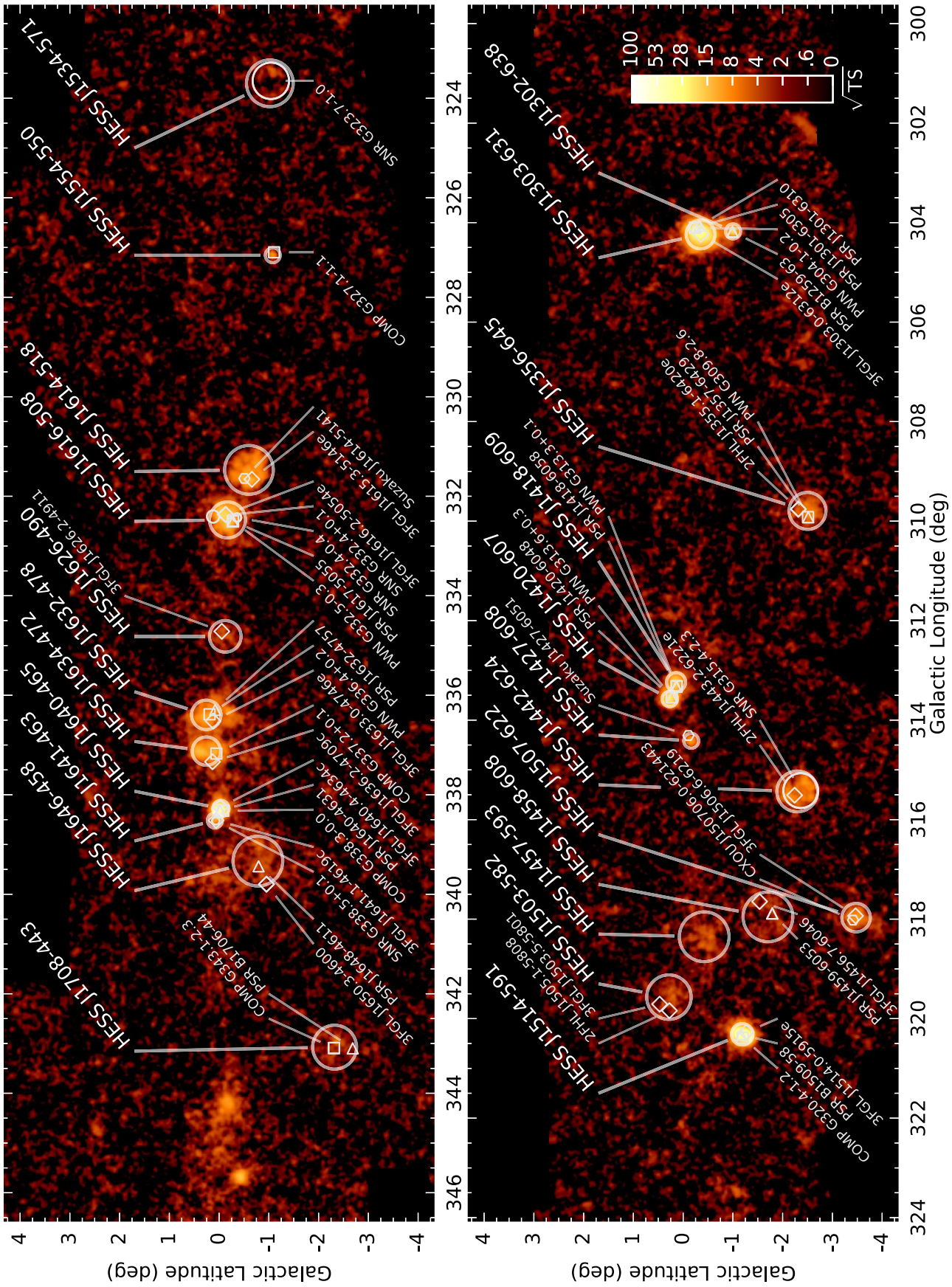

Fig. A.4. HGPS in a MWL context (3 of 4). Fig. A.2 continued.

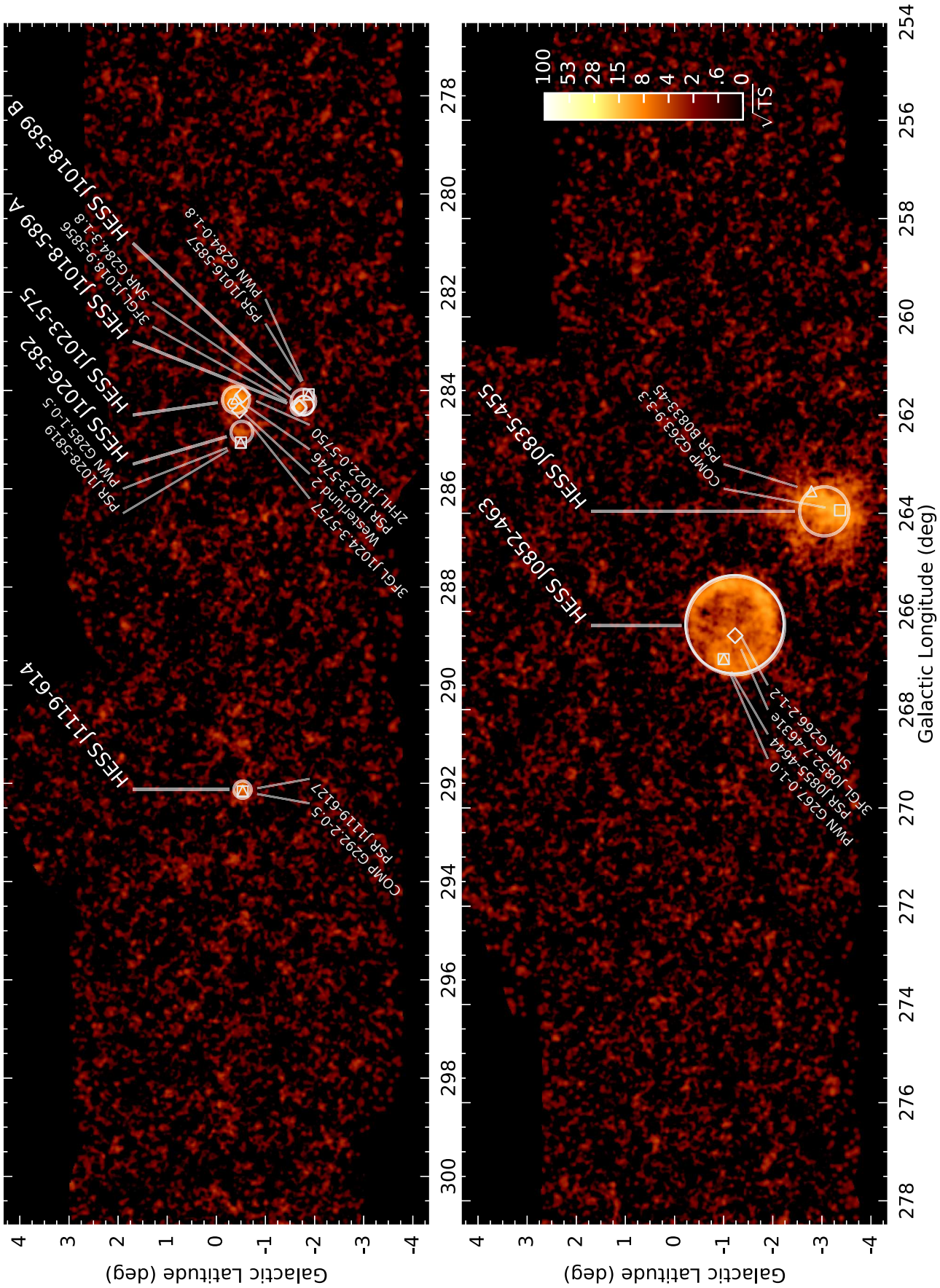

Fig. A.5. HGPS in a MWL context (4 of 4). Fig. A.2 continued.

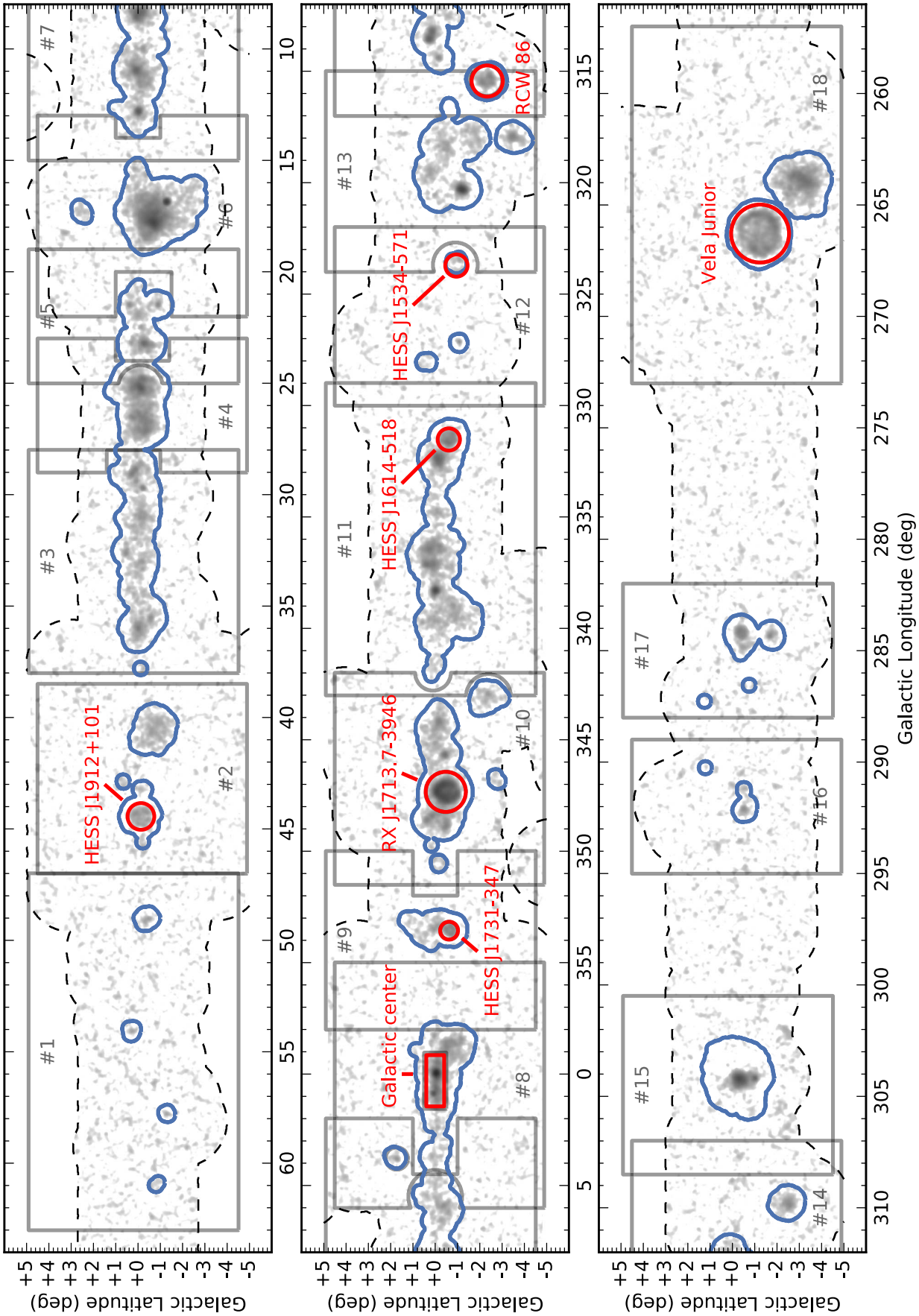

Fig. A.6. Illustration of cut-out regions (red), exclusion regions (blue) and modeling regions (ROIs; gray, numbered) in the HGPS map. The background image displays significance ($R_c = 0.1°$) in inverse grayscale.

Table A.1. HGPS catalog FITS tables. See Sect. A.2.

HDU Extension name	Description	Rows	Column description
HGPS_Sources	HGPS source catalog	78	see Table A.2
HGPS_Gauss_Components	HGPS component list	98	see Table A.3
HGPS_Associations	HGPS association list	223	see Table A.4
HGPS_Identifications	HGPS identification list	31	see Table A.5
HGPS_Large_Scale_Component	HGPS large-scale emission model parameters	50	see Table A.6
SNRcat	Bundled version of SNRcat used for associations	282	

Table A.2. HGPS FITS table columns for `HGPS_Sources`, the main source catalog.

Column	Unit	Description
Source_Name		Source name (HESS JHHmm±DDd identifier)
Analysis_Reference		Source analysis reference ("HGPS" for most sources, "EXTERN" if source in Table 1)
Source_Class		Source class (only filled for identified sources, see Table 3)
Identified_Object		Identified object (only filled for identified sources, see Table 3)
Gamma_Cat_Source_ID		Source ID in the gamma-cat open TeV catalog
RAJ2000	deg	Right Ascension (J2000)
DEJ2000	deg	Declination (J2000)
GLON	deg	Galactic longitude
GLON_Err	deg	Statistical error (1 sigma) on GLON
GLAT	deg	Galactic latitude
GLAT_Err	deg	Statistical error (1 sigma) on GLAT
Pos_Err_68	deg	Position error (68% CL, including systematics, see Eq. (19))
Pos_Err_95	deg	Position error (95% CL, including systematics, see Eq. (19))
ROI_Number		ROI number, see Fig. A.6 for details
Spatial_Model		Spatial model (one of "Gaussian", "X-Gaussian" or "Shell")
Components		List of Gaussian components the source is composed of
Sqrt_TS		Square root of the sum of the test statistics of the individual components (Eq. (11))
Size	deg	Source size (1 sigma for single-Gaussian sources, RMS equivalent for multi-Gaussian sources and outer radius for SNRs)
Size_Err	deg	Statistical error (1 sigma) on Size
Size_UL	deg	Upper limit (95% CL) on Size (Eq. (18), NULL if source is extended)
R70	deg	70% containment radius, computed on the PSF-convolved excess model image
RSpec	deg	R_{spec}, the radius of the spectral analysis circular region
Excess_Model_Total		Total excess from spatial model (this source only)
Excess_RSpec		Data excess in R_Spec (measured on maps)
Excess_RSpec_Model		Model excess in R_Spec (this source, other sources, large scale emission component)
Background_RSpec		Background in R_Spec
Livetime	hour	Livetime for map
Energy_Threshold	TeV	Energy threshold for map (minimum)
Flux_Map	$\mathrm{cm}^{-2}\,\mathrm{s}^{-1}$	Integral flux above 1 TeV from the morphology fit on the map (total)
Flux_Map_Err	$\mathrm{cm}^{-2}\,\mathrm{s}^{-1}$	Statistical error (1 sigma) on Flux_Model_Total
Flux_Map_RSpec_Data	$\mathrm{cm}^{-2}\,\mathrm{s}^{-1}$	Data flux in R_Spec (measured on maps)
Flux_Map_RSpec_Source	$\mathrm{cm}^{-2}\,\mathrm{s}^{-1}$	Model flux in R_Spec (this source only)
Flux_Map_RSpec_Other	$\mathrm{cm}^{-2}\,\mathrm{s}^{-1}$	Model flux in R_Spec (other sources only)
Flux_Map_RSpec_LS	$\mathrm{cm}^{-2}\,\mathrm{s}^{-1}$	Model flux in R_Spec (large scale emission component only)
Flux_Map_RSpec_Total	$\mathrm{cm}^{-2}\,\mathrm{s}^{-1}$	Model flux in R_Spec (this source, other sources, large scale emission component)
Containment_RSpec		Containment fraction (Eq. (23))
Contamination_RSpec		Contamination fraction (Eq. (22))
Flux_Correction_RSpec_To_Total		Total flux correction factor (Eq. (21))
Livetime_Spec	hour	Livetime for spectrum
Energy_Range_Spec_Min	TeV	Minimum energy of counts spectrum
Energy_Range_Spec_Max	TeV	Maximum energy of counts spectrum
Background_Spec		Background from spectral analysis
Excess_Spec		Excess from spectral analysis
Spectral_Model		Spectral model, either "PL" or "ECPL" (Eq. (24)) and (Eq. (25))
TS_ECPL_over_PL		Test statistic difference of ECPL and PL model
Flux_Spec_Int_1TeV	$\mathrm{cm}^{-2}\,\mathrm{s}^{-1}$	PL or ECPL integral flux above 1 TeV, depending on Spectral_Model
Flux_Spec_Int_1TeV_Err	$\mathrm{cm}^{-2}\,\mathrm{s}^{-1}$	Statistical error (1 sigma) on Flux_Spec_Int_1TeV

Notes. The column descriptions link back to sections and equations in the main text where needed.

Table A.2. continued.

Column	Unit	Description
Flux_Spec_Energy_1_10_TeV	erg cm^{-2} s^{-1}	PL or ECPL energy flux in the 1–10 TeV range, depending on Spectral_Model
Flux_Spec_Energy_1_10_TeV_Err	erg cm^{-2} s^{-1}	Statistical error (1 sigma) on Flux_Spec_Energy_1_10_TeV
Energy_Spec_PL_Pivot	TeV	Reference energy E_0, see Eq. (24)
Flux_Spec_PL_Diff_Pivot	cm^{-2} s^{-1} TeV^{-1}	Differential flux at pivot energy
Flux_Spec_PL_Diff_Pivot_Err	cm^{-2} s^{-1} TeV^{-1}	Statistical error (1 sigma) on Flux_Spec_PL_Diff_Pivot
Flux_Spec_PL_Diff_1TeV	cm^{-2} s^{-1} TeV^{-1}	Differential flux at 1 TeV
Flux_Spec_PL_Diff_1TeV_Err	cm^{-2} s^{-1} TeV^{-1}	Statistical error (1 sigma) on Flux_Spec_PL_Diff_1TeV
Index_Spec_PL		Spectral index
Index_Spec_PL_Err		Statistical error (1 sigma) on Index_Spec_PL
Energy_Spec_ECPL_Pivot	TeV	Reference energy E_0 (Eq. (25))
Flux_Spec_ECPL_Diff_Pivot	cm^{-2} s^{-1} TeV^{-1}	Differential flux at pivot energy
Flux_Spec_ECPL_Diff_Pivot_Err	cm^{-2} s^{-1} TeV^{-1}	Statistical error (1 sigma) on Flux_Spec_ECPL_Diff_Pivot
Flux_Spec_ECPL_Diff_1TeV	cm^{-2} s^{-1} TeV^{-1}	Differential flux at 1 TeV
Flux_Spec_ECPL_Diff_1TeV_Err	cm^{-2} s^{-1} TeV^{-1}	Statistical error (1 sigma) on Flux_Spec_ECPL_Diff_1TeV
Index_Spec_ECPL		Spectral index
Index_Spec_ECPL_Err		Statistical error (1 sigma) on Index_Spec_ECPL
Lambda_Spec_ECPL	TeV^{-1}	Spectral cutoff fit parameter (inverse cutoff energy)
Lambda_Spec_ECPL_Err	TeV^{-1}	Statistical error (1 sigma) on Lambda_Spec_ECPL
Flux_Spec_PL_Int_1TeV	cm^{-2} s^{-1}	Integral flux above 1 TeV
Flux_Spec_PL_Int_1TeV_Err	cm^{-2} s^{-1}	Statistical error (1 sigma) on Flux_Spec_PL_Int_1TeV
Flux_Spec_ECPL_Int_1TeV	cm^{-2} s^{-1}	Integral flux above 1 TeV
Flux_Spec_ECPL_Int_1TeV_Err	cm^{-2} s^{-1}	Statistical error (1 sigma) on Flux_Spec_ECPL_Int_1TeV
N_Flux_Points		Number of flux points
Flux_Points_Energy	TeV	Energy value
Flux_Points_Energy_Min	TeV	Lower bound of energy bin
Flux_Points_Energy_Max	TeV	Upper bound of energy bin
Flux_Points_Flux	cm^{-2} s^{-1} TeV^{-1}	Differential flux at given energy
Flux_Points_Flux_Err_Lo	cm^{-2} s^{-1} TeV^{-1}	Lower error on Flux_Points_Flux
Flux_Points_Flux_Err_Hi	cm^{-2} s^{-1} TeV^{-1}	Upper error on Flux_Points_Flux
Flux_Points_Flux_UL	cm^{-2} s^{-1} TeV^{-1}	Upper limit on Flux_Points_Flux
Flux_Points_Flux_Is_UL		Boolean flag when to use Flux_Points_Flux_UL

Table A.3. HGPS FITS table columns for `HGPS_Gauss_Components`.

Column	Unit	Description
Component_ID		Gauss component identifier (HGPSC NNN)
Source_Name		Source name (HESS JHHmm±DDd identifier) the component belongs to
Component_Class		Component class (see Sect. 4.9)
GLON	deg	Galactic longitude
GLON_Err	deg	Statistical error (1 sigma) on GLON
GLAT	deg	Galactic latitude
GLAT_Err	deg	Statistical error (1 sigma) on GLAT
Sqrt_TS		Square root of the the test statistics of the component (see Eq. (11))
Size	deg	Component size (1 σ Gaussian width)
Size_Err	deg	Statistical error (1 sigma) on Size
Flux_Map	cm^{-2} s^{-1}	Integral flux above 1 TeV from the morphology fit on the map (total)
Flux_Map_Err	cm^{-2} s^{-1}	Statistical error (1 sigma) on Flux_Map
Excess		Total model excess contained in the component

Notes. See Sects. 4.8 and 4.10.

Table A.4. HGPS FITS table columns for `HGPS_Associations`.

Column	Unit	Description
Source_Name		Source name (HESS JHHmm±DDd identifier)
Association_Catalog		Association catalog name (see Table 2)
Association_Name		Association source name
Separation	deg	Angular separation to HGPS source position

Notes. See Sect. 5.1.

Table A.5. HGPS FITS table columns for `HGPS_Identifications`.

Column	Unit	Description
Source_Name		Source name (HESS JHHmm±DDd identifier)
Identified_Object		Identified object name
Class		Class of the identified object
Evidence		Evidence for the identification
Reference		Reference for the identification
Distance_Reference		Reference for the distance estimate
Distance	kpc	Distance of the identified object
Distance_Min	kpc	Minimum distance of the identified object
Distance_Max	kpc	Maximum distance of the identified object

Notes. See Sect. 5.1.3.

Table A.6. HGPS FITS table columns for `HGPS_Large_Scale_Component`.

Column	Unit	Description
GLON	deg	Galactic longitude of window center
GLAT	deg	Peak latitude
GLAT_Err	deg	Statistical error (1 sigma) on peak latitude
Surface_Brightness	$cm^{-2}\ s^{-1}\ sr^{-1}$	Peak brightness
Surface_Brightness_Err	$cm^{-2}\ s^{-1}\ sr^{-1}$	Statistical error (1 sigma) on peak surface brightness
Width	deg	Gaussian width
Width_Err	deg	Statistical error (1 sigma) on Gaussian width

Notes. See Sect. 4.6.

Table A.7. HGPS source catalog – summary of map-based measurements.

Name	Spatial model	GLON	GLAT	R_{95}	Size	$F(>1\,\mathrm{TeV})$	$F(>1\,\mathrm{TeV})$	$\sqrt{\mathrm{TS}}$
		deg	deg	deg	deg	$10^{-12}\mathrm{cm}^{-2}\mathrm{s}^{-1}$	% Crab	
HESS J0835−455	3-Gaussian	263.96	−3.05	0.09	0.58 ± 0.052	15.36 ± 0.53	67.7 ± 2.4	39.4
HESS J0852−463*	Shell	266.29	−1.24	–	1.00	23.39 ± 2.35	103.2 ± 10.3	–
HESS J1018−589 A	Gaussian	284.35	−1.67	0.03	0.00 ± 0.012	0.30 ± 0.05	1.3 ± 0.2	8.7
HESS J1018−589 B	Gaussian	284.22	−1.77	0.12	0.15 ± 0.026	0.83 ± 0.17	3.7 ± 0.8	7.6
HESS J1023−575	Gaussian	284.19	−0.40	0.05	0.17 ± 0.009	2.56 ± 0.17	11.3 ± 0.8	21.4
HESS J1026−582	Gaussian	284.85	−0.52	0.12	0.13 ± 0.039	0.69 ± 0.19	3.0 ± 0.9	7.3
HESS J1119−614	Gaussian	292.13	−0.53	0.06	0.10 ± 0.014	0.87 ± 0.13	3.8 ± 0.6	10.2
HESS J1302−638	Gaussian	304.18	−1.00	0.02	0.01 ± 0.009	0.40 ± 0.05	1.7 ± 0.2	16.6
HESS J1303−631	2-Gaussian	304.24	−0.35	0.04	0.18 ± 0.015	5.26 ± 0.27	23.2 ± 1.2	54.5
HESS J1356−645	Gaussian	309.79	−2.50	0.08	0.23 ± 0.020	5.53 ± 0.53	24.4 ± 2.3	17.3
HESS J1418−609	Gaussian	313.24	0.14	0.04	0.11 ± 0.011	3.01 ± 0.31	13.3 ± 1.4	21.9
HESS J1420−607	Gaussian	313.58	0.27	0.03	0.08 ± 0.006	3.28 ± 0.24	14.5 ± 1.1	27.6
HESS J1427−608	Gaussian	314.42	−0.16	0.04	0.05 ± 0.009	0.74 ± 0.10	3.3 ± 0.5	10.5
HESS J1442−624*	Shell	315.43	−2.29	–	0.30 ± 0.020	2.44 ± 0.67	10.8 ± 3.0	–
HESS J1457−593	Gaussian	318.35	−0.42	0.15	0.33 ± 0.045	2.50 ± 0.40	11.0 ± 1.8	12.5
HESS J1458−608	Gaussian	317.95	−1.70	0.17	0.37 ± 0.031	2.44 ± 0.30	10.8 ± 1.3	11.5
HESS J1503−582	Gaussian	319.57	0.29	0.14	0.28 ± 0.033	1.89 ± 0.28	8.3 ± 1.2	10.8
HESS J1507−622	Gaussian	317.97	−3.48	0.06	0.18 ± 0.017	2.99 ± 0.31	13.2 ± 1.4	17.0
HESS J1514−591	3-Gaussian	320.32	−1.19	0.03	0.14 ± 0.026	6.43 ± 0.21	28.4 ± 0.9	42.0
HESS J1534−571*	Shell	323.70	−1.02	–	0.40 ± 0.040	1.98 ± 0.23	8.7 ± 1.0	–
HESS J1554−550	Gaussian	327.16	−1.08	0.03	0.02 ± 0.009	0.36 ± 0.06	1.6 ± 0.3	9.1
HESS J1614−518*	Shell	331.47	−0.60	–	0.42 ± 0.010	5.87 ± 0.42	25.9 ± 1.9	–
HESS J1616−508	2-Gaussian	332.48	−0.17	0.12	0.23 ± 0.035	8.48 ± 0.44	37.4 ± 1.9	34.3
HESS J1626−490	Gaussian	334.82	−0.12	0.14	0.20 ± 0.035	1.65 ± 0.33	7.3 ± 1.5	8.4
HESS J1632−478	Gaussian	336.39	0.26	0.08	0.18 ± 0.020	2.93 ± 0.51	12.9 ± 2.3	14.8
HESS J1634−472	Gaussian	337.12	0.26	0.06	0.17 ± 0.013	2.90 ± 0.37	12.8 ± 1.6	17.8
HESS J1640−465	2-Gaussian	338.28	−0.04	0.05	0.11 ± 0.034	3.33 ± 0.19	14.7 ± 0.8	41.1
HESS J1641−463	Gaussian	338.52	0.08	0.05	0.04 ± 0.013	0.27 ± 0.06	1.2 ± 0.3	6.9
HESS J1646−458	Gaussian	339.33	−0.78	0.15	0.50 ± 0.030	5.48 ± 0.46	24.2 ± 2.0	18.6
HESS J1702−420	Gaussian	344.23	−0.19	0.08	0.20 ± 0.025	3.91 ± 0.65	17.3 ± 2.9	15.0
HESS J1708−410	Gaussian	345.67	−0.44	0.03	0.06 ± 0.006	0.88 ± 0.09	3.9 ± 0.4	17.0
HESS J1708−443	Gaussian	343.07	−2.32	0.14	0.28 ± 0.031	2.28 ± 0.32	10.1 ± 1.4	11.0
HESS J1713−381	Gaussian	348.62	0.38	0.05	0.09 ± 0.017	0.65 ± 0.13	2.9 ± 0.6	11.6
HESS J1713−397*	Shell	347.31	−0.46	–	0.50	16.88 ± 0.82	74.4 ± 3.6	–
HESS J1714−385	Gaussian	348.42	0.14	0.04	0.03 ± 0.011	0.25 ± 0.05	1.1 ± 0.2	8.6
HESS J1718−374*	Point-Like	349.72	0.17	–	–	0.12 ± 0.04	0.6 ± 0.2	–
HESS J1718−385	Gaussian	348.88	−0.48	0.06	0.12 ± 0.015	0.80 ± 0.14	3.5 ± 0.6	11.6
HESS J1729−345	Gaussian	353.39	−0.02	0.13	0.19 ± 0.031	0.86 ± 0.17	3.8 ± 0.8	8.4
HESS J1731−347*	Shell	353.54	−0.67	–	0.27 ± 0.020	2.01 ± 0.15	8.8 ± 0.6	–
HESS J1741−302*	Point-Like	358.28	0.05	–	–	0.16 ± 0.04	0.7 ± 0.2	–
HESS J1745−290*	Point-Like	359.94	−0.04	–	–	1.70 ± 0.08	7.5 ± 0.3	–
HESS J1745−303	Gaussian	358.64	−0.56	0.11	0.18 ± 0.020	0.94 ± 0.21	4.1 ± 0.9	13.7
HESS J1746−285*	Point-Like	0.14	−0.11	–	–	0.15 ± 0.05	0.7 ± 0.2	–
HESS J1746−308	Gaussian	358.45	−1.11	0.15	0.16 ± 0.036	0.68 ± 0.22	3.0 ± 1.0	8.7
HESS J1747−248	Gaussian	3.78	1.71	0.06	0.06 ± 0.012	0.29 ± 0.05	1.3 ± 0.2	8.1
HESS J1747−281*	Point-Like	0.87	0.08	–	–	0.60 ± 0.13	2.6 ± 0.6	–
HESS J1800−240	Gaussian	5.96	−0.42	0.13	0.32 ± 0.039	2.44 ± 0.35	10.8 ± 1.5	12.6
HESS J1801−233*	Gaussian	6.66	−0.27	–	0.17 ± 0.030	0.45 ± 0.10	2.0 ± 0.4	–
HESS J1804−216	2-Gaussian	8.38	−0.09	0.15	0.24 ± 0.034	5.88 ± 0.27	25.9 ± 1.2	34.2
HESS J1808−204	Gaussian	10.01	−0.24	0.07	0.06 ± 0.014	0.19 ± 0.04	0.8 ± 0.2	6.4
HESS J1809−193	3-Gaussian	11.11	−0.02	0.21	0.40 ± 0.048	5.27 ± 0.29	23.2 ± 1.3	26.6

Notes. This is a small excerpt of the information available in the FITS catalog. The data shown here correspond to the following catalog columns (described in Table A.2): `Source_Name`, `Spatial_Model`, `GLON`, `GLAT`, `Pos_Err_95`, `Size`, `Size_Err`, `Size_UL`, `Flux_Map`, `Flux_Map_Err`, and `Sqrt_TS`. The values for sources indicated with an asterisk are taken from external references; see Table 1 for details.

Table A.7. continued.

Name	Spatial model	GLON	GLAT	R_{95}	Size	$F(>1\ \mathrm{TeV})$	$F(>1\ \mathrm{TeV})$	$\sqrt{\mathrm{TS}}$
		deg	deg	deg	deg	10^{-12} cm^{-2} s^{-1}	% Crab	
HESS J1813−126	Gaussian	17.31	2.49	0.19	0.21 ± 0.032	1.08 ± 0.24	4.8 ± 1.1	6.1
HESS J1813−178	Gaussian	12.82	−0.03	0.02	0.05 ± 0.004	1.98 ± 0.15	8.7 ± 0.7	26.4
HESS J1818−154	Gaussian	15.41	0.16	0.04	0.00 ± 0.046	0.17 ± 0.04	0.7 ± 0.2	5.6
HESS J1825−137	3-Gaussian	17.53	−0.62	0.20	0.46 ± 0.032	18.41 ± 0.56	81.2 ± 2.5	76.5
HESS J1826−130	Gaussian	18.48	−0.39	0.10	0.15 ± 0.021	0.86 ± 0.17	3.8 ± 0.7	9.4
HESS J1826−148	Gaussian	16.88	−1.29	0.02	0.01 ± 0.004	1.28 ± 0.04	5.7 ± 0.2	58.1
HESS J1828−099	Gaussian	21.49	0.38	0.05	0.05 ± 0.011	0.43 ± 0.07	1.9 ± 0.3	8.9
HESS J1832−085	Gaussian	23.21	0.29	0.05	0.02 ± 0.012	0.21 ± 0.05	0.9 ± 0.2	5.9
HESS J1832−093	Gaussian	22.48	−0.16	0.03	0.00 ± 0.012	0.17 ± 0.03	0.8 ± 0.1	6.8
HESS J1833−105	Gaussian	21.50	−0.90	0.03	0.02 ± 0.017	0.39 ± 0.07	1.7 ± 0.3	11.4
HESS J1834−087	2-Gaussian	23.26	−0.33	0.06	0.21 ± 0.037	3.34 ± 0.24	14.7 ± 1.1	21.0
HESS J1837−069	3-Gaussian	25.15	−0.09	0.05	0.36 ± 0.031	12.05 ± 0.45	53.1 ± 2.0	41.5
HESS J1841−055	2-Gaussian	26.71	−0.23	0.17	0.41 ± 0.033	10.16 ± 0.42	44.8 ± 1.9	33.9
HESS J1843−033	2-Gaussian	28.90	0.07	0.20	0.24 ± 0.063	2.88 ± 0.30	12.7 ± 1.3	16.0
HESS J1844−030	Gaussian	29.41	0.09	0.04	0.02 ± 0.013	0.26 ± 0.05	1.1 ± 0.2	7.3
HESS J1846−029	Gaussian	29.71	−0.24	0.03	0.01 ± 0.013	0.45 ± 0.05	2.0 ± 0.2	13.8
HESS J1848−018	Gaussian	30.92	−0.21	0.12	0.25 ± 0.032	1.74 ± 0.35	7.7 ± 1.6	12.0
HESS J1849−000	Gaussian	32.61	0.53	0.06	0.09 ± 0.015	0.53 ± 0.09	2.3 ± 0.4	9.1
HESS J1852−000	Gaussian	33.11	−0.13	0.18	0.28 ± 0.042	1.30 ± 0.25	5.7 ± 1.1	9.0
HESS J1857+026	2-Gaussian	36.06	−0.06	0.10	0.26 ± 0.056	3.77 ± 0.40	16.6 ± 1.8	16.8
HESS J1858+020	Gaussian	35.54	−0.58	0.07	0.08 ± 0.016	0.53 ± 0.11	2.3 ± 0.5	8.4
HESS J1908+063	Gaussian	40.55	−0.84	0.13	0.49 ± 0.027	6.53 ± 0.50	28.8 ± 2.2	19.0
HESS J1911+090*	Point-Like	43.26	−0.19	–	–	0.15 ± 0.03	0.6 ± 0.1	–
HESS J1912+101*	Shell	44.46	−0.13	–	0.49 ± 0.040	2.49 ± 0.35	11.0 ± 1.5	–
HESS J1923+141	Gaussian	49.08	−0.40	0.10	0.12 ± 0.019	0.78 ± 0.15	3.5 ± 0.7	7.3
HESS J1930+188	Gaussian	54.06	0.27	0.05	0.02 ± 0.025	0.29 ± 0.09	1.3 ± 0.4	5.8
HESS J1943+213	Gaussian	57.78	−1.30	0.05	0.03 ± 0.022	0.32 ± 0.10	1.4 ± 0.4	5.9

Table A.8. HGPS source catalog – summary of spectral measurements.

Name	$R_{\rm spec}$	$E_{\rm min}$	$F(>1\ {\rm TeV})$	Γ	λ	Contain.	Contam.	CF
	deg	TeV	10^{-12} cm^{-2} s^{-1}		TeV^{-1}	%	%	
HESS J0835−455	0.50	0.3	17.43 ± 1.40	1.35 ± 0.08	0.08 ± 0.01	37	0	271.4
HESS J0852−463*	1.00	0.3	23.39 ± 2.35	1.81 ± 0.08	0.15 ± 0.03	–	–	–
HESS J1018−589 A	0.15	0.4	0.21 ± 0.03	2.24 ± 0.13	–	92	42	63.5
HESS J1018−589 B	0.25	0.5	0.70 ± 0.09	2.20 ± 0.09	–	70	32	96.8
HESS J1023−575	0.27	0.4	2.41 ± 0.13	2.36 ± 0.05	–	70	5	135.5
HESS J1026−582	0.22	0.5	0.66 ± 0.09	1.81 ± 0.10	–	70	11	126.9
HESS J1119−614	0.18	0.4	0.92 ± 0.09	2.64 ± 0.12	–	70	4	137.9
HESS J1302−638	0.15	0.4	0.39 ± 0.03	2.59 ± 0.09	–	90	40	67.4
HESS J1303−631	0.29	0.4	5.21 ± 0.35	2.04 ± 0.06	0.07 ± 0.01	70	5	136.2
HESS J1356−645	0.37	0.5	4.39 ± 0.39	2.20 ± 0.08	–	70	0	142.8
HESS J1418−609	0.19	0.4	2.69 ± 0.15	2.26 ± 0.05	–	70	6	134.7
HESS J1420−607	0.15	0.4	2.77 ± 0.15	2.20 ± 0.05	–	70	4	138.5
HESS J1427−608	0.15	0.4	0.48 ± 0.09	2.85 ± 0.22	–	84	5	113.3
HESS J1442−624*	0.41	0.4	2.44 ± 0.67	1.59 ± 0.22	0.29 ± 0.10	–	–	–
HESS J1457−593	0.50	0.5	4.31 ± 0.56	2.52 ± 0.14	–	67	10	135.1
HESS J1458−608	0.50	0.5	1.40 ± 0.35	1.81 ± 0.14	–	58	1	170.2
HESS J1503−582	0.45	0.4	3.07 ± 0.24	2.68 ± 0.08	–	70	8	131.1
HESS J1507−622	0.29	0.5	2.60 ± 0.21	2.22 ± 0.07	–	70	0	142.9
HESS J1514−591	0.22	0.4	5.72 ± 0.42	2.05 ± 0.06	0.05 ± 0.01	70	0	142.8
HESS J1534−571*	0.47	0.4	1.98 ± 0.23	2.51 ± 0.09	–	–	–	–
HESS J1554−550	0.15	0.4	0.29 ± 0.06	2.19 ± 0.17	–	92	0	108.6
HESS J1614−518*	0.49	0.3	5.87 ± 0.42	2.42 ± 0.06	–	–	–	–
HESS J1616−508	0.36	0.3	7.99 ± 0.55	2.32 ± 0.06	–	70	2	139.9
HESS J1626−490	0.32	0.3	2.13 ± 0.26	2.47 ± 0.11	–	70	11	126.9
HESS J1632−478	0.30	0.3	2.32 ± 0.16	2.52 ± 0.06	–	70	34	93.9
HESS J1634−472	0.28	0.3	2.87 ± 0.15	2.31 ± 0.05	–	70	31	98.8
HESS J1640−465	0.16	0.3	2.84 ± 0.73	2.12 ± 0.13	0.24 ± 0.09	70	4	137.6
HESS J1641−463	0.15	0.3	0.22 ± 0.03	2.47 ± 0.11	–	90	58	47.4
HESS J1646−458	0.50	0.3	5.81 ± 0.73	2.54 ± 0.13	–	39	2	254.4
HESS J1702−420	0.32	0.2	4.45 ± 0.36	2.09 ± 0.07	–	70	14	122.9
HESS J1708−410	0.15	0.2	0.65 ± 0.05	2.54 ± 0.07	–	81	9	112.8
HESS J1708−443	0.44	0.2	3.32 ± 0.37	2.17 ± 0.08	–	70	0	142.9
HESS J1713−381	0.16	0.2	0.52 ± 0.07	2.74 ± 0.12	–	70	15	121.4
HESS J1713−397*	0.60	0.2	16.88 ± 0.82	2.06 ± 0.02	0.08 ± 0.01	–	–	–
HESS J1714−385	0.15	0.2	0.21 ± 0.03	2.52 ± 0.12	–	91	47	57.9
HESS J1718−374*	0.10	0.2	0.12 ± 0.04	2.80 ± 0.27	–	–	–	–
HESS J1718−385	0.20	0.2	0.62 ± 0.14	0.98 ± 0.22	0.09 ± 0.03	70	23	110.4
HESS J1729−345	0.30	0.2	0.82 ± 0.09	2.43 ± 0.09	–	70	25	108.0
HESS J1731−347*	0.30	0.2	2.01 ± 0.15	2.32 ± 0.06	–	–	–	–
HESS J1741−302*	0.10	0.4	0.16 ± 0.04	2.30 ± 0.20	–	–	–	–
HESS J1745−290*	0.10	–	1.70 ± 0.08	2.14 ± 0.02	0.09 ± 0.02	–	–	–
HESS J1745−303	0.29	0.2	1.09 ± 0.08	2.57 ± 0.06	–	70	30	99.6
HESS J1746−285*	0.09	0.3	0.15 ± 0.05	2.17 ± 0.24	–	–	–	–
HESS J1746−308	0.26	0.2	0.30 ± 0.09	3.27 ± 0.22	–	70	23	110.2
HESS J1747−248	0.15	0.2	0.27 ± 0.04	2.36 ± 0.14	–	83	0	120.5

Notes. This is a small excerpt of the information available in the FITS catalog. The data shown here correspond to the following catalog columns (described in Table A.2): `Source_Name`, `RSpec`, `Energy_Range_Spec_Lo`, `Flux_Spec_Int_1TeV` (`Flux_Map` for extern sources), `Index_Spec_PL`, `Index_Spec_PL_Err` (for PL spectrum sources), `Index_Spec_ECPL`, `Index_Spec_ECPL_Err`, `Lambda_Spec_ECPL`, `Lambda_Spec_ECPL_Err` (for ECPL spectrum sources), `Containment_RSpec`, `Contamination_RSpec` and `Flux_Correction_RSpec_To_Total`. The values for sources indicated with an asterisk are taken from external references, see Table 1 for details.

Table A.8. continued.

Name	R_{spec}	E_{min}	$F(>1\ TeV)$	Γ	λ	Contain.	Contam.	CF
	deg	TeV	10^{-12} cm^{-2} s^{-1}		TeV^{-1}	%	%	
HESS J1747−281*	0.10	0.3	0.60 ± 0.13	2.40 ± 0.11	–	–	–	–
HESS J1800−240	0.50	0.2	2.90 ± 0.31	2.47 ± 0.09	–	70	17	118.9
HESS J1801−233*	0.20	0.3	0.45 ± 0.10	2.66 ± 0.27	–	–	–	–
HESS J1804−216	0.38	0.2	5.12 ± 0.23	2.69 ± 0.04	–	70	8	131.6
HESS J1808−204	0.15	0.2	0.19 ± 0.03	2.19 ± 0.14	–	85	27	86.1
HESS J1809−193	0.50	0.2	5.37 ± 0.45	2.38 ± 0.07	–	54	16	154.2
HESS J1813−126	0.34	0.2	1.04 ± 0.21	1.99 ± 0.14	–	70	0	143.6
HESS J1813−178	0.15	0.2	2.12 ± 0.40	1.64 ± 0.12	0.14 ± 0.04	89	14	96.6
HESS J1818−154	0.15	0.2	0.23 ± 0.05	2.21 ± 0.15	–	95	29	74.6
HESS J1825−137	0.50	0.2	19.15 ± 1.85	2.15 ± 0.06	0.07 ± 0.02	47	3	203.6
HESS J1826−130	0.25	0.2	1.14 ± 0.16	2.04 ± 0.10	–	70	41	84.4
HESS J1826−148	0.15	0.2	0.84 ± 0.08	2.32 ± 0.07	–	95	10	94.5
HESS J1828−099	0.15	0.2	0.38 ± 0.05	2.25 ± 0.12	–	89	11	100.3
HESS J1832−085	0.15	0.2	0.23 ± 0.04	2.38 ± 0.14	–	94	27	77.7
HESS J1832−093	0.15	0.2	0.16 ± 0.04	2.54 ± 0.22	–	95	25	78.9
HESS J1833−105	0.15	0.2	0.26 ± 0.06	2.42 ± 0.19	–	94	2	104.6
HESS J1834−087	0.34	0.2	2.47 ± 0.22	2.61 ± 0.07	–	70	8	131.2
HESS J1837−069	0.50	0.2	11.55 ± 0.49	2.54 ± 0.04	–	63	8	145.6
HESS J1841−055	0.50	0.2	11.58 ± 1.36	2.21 ± 0.07	0.09 ± 0.03	51	10	178.3
HESS J1843−033	0.38	0.2	3.04 ± 0.20	2.15 ± 0.05	–	70	15	121.0
HESS J1844−030	0.15	0.2	0.28 ± 0.04	2.48 ± 0.12	–	94	28	77.0
HESS J1846−029	0.15	0.2	0.48 ± 0.05	2.41 ± 0.09	–	94	10	95.8
HESS J1848−018	0.39	0.3	1.11 ± 0.15	2.57 ± 0.11	–	70	26	105.9
HESS J1849−000	0.16	0.3	0.58 ± 0.07	1.97 ± 0.09	–	70	9	129.9
HESS J1852−000	0.44	0.3	1.21 ± 0.15	2.17 ± 0.10	–	70	25	106.8
HESS J1857+026	0.41	0.3	4.00 ± 0.29	2.57 ± 0.06	–	70	11	127.6
HESS J1858+020	0.15	0.3	0.47 ± 0.06	2.39 ± 0.12	–	72	14	120.6
HESS J1908+063	0.50	0.3	8.35 ± 0.57	2.26 ± 0.06	–	41	2	240.9
HESS J1911+090*	0.10	0.3	0.15 ± 0.03	3.14 ± 0.24	–	–	–	–
HESS J1912+101*	0.56	0.7	2.49 ± 0.35	2.56 ± 0.09	–	–	–	–
HESS J1923+141	0.21	0.4	0.69 ± 0.11	2.55 ± 0.17	–	70	3	138.7
HESS J1930+188	0.15	0.5	0.32 ± 0.07	2.59 ± 0.26	–	92	8	100.3
HESS J1943+213	0.15	0.6	0.39 ± 0.08	2.83 ± 0.22	–	91	1	109.0

Table A.9. HGPS source associations (see Sect. 5.1).

H.E.S.S. source	Association
HESS J0835−455	G263.9−3.3 (COMP) 2FHL J0835.3−4511 (2FHL) 3FGL J0835.3−4510 (3FGL) B0833−45 (PSR)
HESS J0852−463	G266.2−1.2 (SNR) 2FHL J0852.8−4631e (2FHL) 3FGL J0852.7−4631e (3FGL) J0855−4644 (PSR) G267.0−1.0 (PWN)
HESS J1018−589 A	3FGL J1018.9−5856 (3FGL) G284.3−1.8 (SNR)
HESS J1018−589 B	G284.3−1.8 (SNR) 3FGL J1018.9−5856 (3FGL) J1016−5857 (PSR) G284.0−1.8 (PWN) 3FGL J1016.3−5858 (3FGL)
HESS J1023−575	3FGL J1023.1−5745 (3FGL) J1023−5746 (PSR) Westerlund 2 (EXTRA) 2FHL J1022.0−5750 (2FHL) 3FGL J1024.3−5757 (3FGL)
HESS J1026−582	G285.1−0.5 (PWN) J1028−5819 (PSR)
HESS J1119−614	3FGL J1119.1−6127 (3FGL) J1119−6127 (PSR) G292.2−0.5 (COMP)
HESS J1302−638	B1259−63 (PSR)
HESS J1303−631	2FHL J1303.4−6312e (2FHL) 3FGL J1303.0−6312e (3FGL) J1301−6305 (PSR) J1301−6310 (PSR) G304.1−0.2 (PWN)
HESS J1356−645	3FGL J1356.6−6428 (3FGL) G309.8−2.6 (PWN) J1357−6429 (PSR) 2FHL J1355.1−6420e (2FHL)
HESS J1418−609	3FGL J1418.6−6058 (3FGL) G313.3+0.1 (PWN) J1418−6058 (PSR)
HESS J1420−607	G313.6+0.3 (PWN) J1420−6048 (PSR) 3FGL J1420.0−6048 (3FGL) 2FHL J1419.3−6047e (2FHL)
HESS J1427−608	*Suzaku* J1427−6051 (EXTRA)
HESS J1442−624	G315.4−2.3 (SNR) 2FHL J1443.2−6221e (2FHL)
HESS J1457−593	–
HESS J1458−608	J1459−6053 (PSR) 3FGL J1459.4−6053 (3FGL) 3FGL J1456.7−6046 (3FGL)
HESS J1503−582	3FGL J1503.5−5801 (3FGL) 2FHL J1505.1−5808 (2FHL)
HESS J1507−622	3FGL J1506.6−6219 (3FGL) CXOU J150706.0−621443 (EXTRA) 2FHL J1507.4−6213 (2FHL)
HESS J1514−591	B1509−58 (PSR) 3FGL J1513.9−5908 (3FGL) G320.4−1.2 (COMP) 3FGL J1514.0−5915e (3FGL) 2FHL J1514.0−5915e (2FHL)
HESS J1534−571	G323.7−1.0 (SNR)
HESS J1554−550	G327.1−1.1 (COMP)
HESS J1614−518	*Suzaku* J1614−5141 (EXTRA) 2FHL J1615.3−5146e (2FHL) 3FGL J1615.3−5146e (3FGL)
HESS J1616−508	J1617−5055 (PSR) G332.5−0.3 (PWN) 2FHL J1616.2−5054e (2FHL) 3FGL J1616.2−5054e (3FGL) G332.4−0.4 (SNR) G332.4+0.1 (SNR)
HESS J1626−490	3FGL J1626.2−4911 (3FGL)
HESS J1632−478	G336.4+0.2 (PWN) 2FHL J1633.5−4746e (2FHL) 3FGL J1633.0−4746e (3FGL) J1632−4757 (PSR)
HESS J1634−472	G337.2+0.1 (COMP) 3FGL J1636.2−4709c (3FGL)
HESS J1640−465	2FHL J1640.6−4632 (2FHL) 3FGL J1640.4−4634c (3FGL) J1640−4631 (PSR) G338.3−0.0 (COMP)
HESS J1641−463	G338.5+0.1 (SNR) 3FGL J1641.1−4619c (3FGL)
HESS J1646−458	3FGL J1648.3−4611 (3FGL) J1648−4611 (PSR) 3FGL J1650.3−4600 (3FGL)
HESS J1702−420	–
HESS J1708−410	–
HESS J1708−443	G343.1−2.3 (COMP) B1706−44 (PSR) 3FGL J1709.7−4429 (3FGL)
HESS J1713−381	G348.7+0.3 (SNR) CXOU J171405.7−381031 (EXTRA) J1714−3810 (PSR)

Table A.9. continued.

Table A.9. continued.

H.E.S.S. source	Association
HESS J1713−397	2FHL J1713.5−3945e (2FHL) 3FGL J1713.5−3945e (3FGL) G347.3−0.5 (SNR) 2FHL J1714.1−4012 (2FHL)
HESS J1714−385	3FGL J1714.5−3832 (3FGL) G348.5+0.1 (COMP)
HESS J1718−374	G349.7+0.2 (SNR) 3FGL J1718.0−3726 (3FGL)
HESS J1718−385	3FGL J1718.1−3825 (3FGL) G348.9−0.4 (PWN) J1718−3825 (PSR)
HESS J1729−345	–
HESS J1731−347	G353.6−0.7 (SNR)
HESS J1741−302	–
HESS J1745−290	Sgr A* (EXTRA) J1745−2900 (PSR) G359.9−0.0 (PWN) 2FHL J1745.7−2900 (2FHL) 3FGL J1745.6−2859c (3FGL) G0.0+0.0 (COMP) 3FGL J1745.3−2903c (3FGL)
HESS J1745−303	3FGL J1745.1−3011 (3FGL) 2FHL J1745.1−3035 (2FHL)
HESS J1746−285	3FGL J1746.3−2851c (3FGL) G0.1−0.1 (COMP) J1746−2850 (PSR)
HESS J1746−308	G358.5−0.9 (SNR) B1742−30 (PSR)
HESS J1747−248	3FGL J1748.0−2447 (3FGL) Terzan 5 (EXTRA)
HESS J1747−281	J1747−2809 (PSR) G0.9+0.1 (COMP)
HESS J1800−240	3FGL J1800.8−2402 (3FGL) 2FHL J1801.7−2358 (2FHL) 3FGL J1758.8−2402 (3FGL) G5.7−0.1 (SNR)
HESS J1801−233	2FHL J1801.3−2326e (2FHL) 3FGL J1801.3−2326e (3FGL) W28 (EXTRA)
HESS J1804−216	G8.3−0.0 (SNR) B1800−21 (PSR) 3FGL J1805.6−2136e (3FGL) 2FHL J1805.6−2136e (2FHL) G8.7−0.1 (COMP) J1803−2149 (PSR) 3FGL J1803.1−2147 (3FGL)
HESS J1808−204	J1808−2024 (PSR) SGR 1806−20 (EXTRA) 1806−20 star cluster (EXTRA)

Table A.9. continued.

H.E.S.S. source	Association
HESS J1809−193	G11.0−0.0 (SNR) J1809−1917 (PSR) G11.1+0.1 (COMP) 3FGL J1810.1−1910 (3FGL) G11.4−0.1 (SNR) 3FGL J1811.3−1927c (3FGL) G11.2−0.3 (COMP) J1811−1925 (PSR)
HESS J1813−126	J1813−1246 (PSR) 3FGL J1813.4−1246 (3FGL)
HESS J1813−178	J1813−1749 (PSR) G12.8−0.0 (COMP) G12.7−0.0 (SNR)
HESS J1818−154	G15.4+0.1 (COMP)
HESS J1825−137	3FGL J1824.5−1351e (3FGL) 2FHL J1824.5−1350e (2FHL) G18.0−0.7 (PWN) B1823−13 (PSR)
HESS J1826−130	G18.5−0.4 (PWN) J1826−1256 (PSR) 3FGL J1826.1−1256 (3FGL) G18.6−0.2 (SNR)
HESS J1826−148	LS 5039 (EXTRA) 3FGL J1826.2−1450 (3FGL) 2FHL J1826.3−1450 (2FHL)
HESS J1828−099	–
HESS J1832−085	–
HESS J1832−093	XMMU J183245−0921539 (EXTRA)
HESS J1833−105	G21.5−0.9 (COMP) J1833−1034 (PSR) 3FGL J1833.5−1033 (3FGL)
HESS J1834−087	J1834−0845 (PSR) G23.3−0.3 (COMP) 2FHL J1834.5−0846e (2FHL) 3FGL J1834.5−0841 (3FGL)
HESS J1837−069	J1838−0655 (PSR) 2FHL J1836.5−0655e (2FHL) 3FGL J1836.5−0655e (3FGL) 2FHL J1837.4−0717 (2FHL) 3FGL J1837.6−0717 (3FGL) G25.2+0.3 (PWN) 3FGL J1838.9−0646 (3FGL)
HESS J1841−055	2FHL J1840.9−0532e (2FHL) 3FGL J1840.9−0532e (3FGL) G26.6−0.1 (PWN) J1841−0524 (PSR) 3FGL J1839.3−0552 (3FGL) J1838−0537 (PSR) 3FGL J1838.9−0537 (3FGL)

Table A.9. continued.

H.E.S.S. source	Association
HESS J1843−033	3FGL J1843.7−0322 (3FGL) 3FGL J1844.3−0344 (3FGL) G28.6−0.1 (SNR)
HESS J1844−030	PMN J1844−0306 (EXTRA) G29.4+0.1 (COMP)
HESS J1846−029	J1846−0258 (PSR) G29.7−0.3 (COMP)
HESS J1848−018	3FGL J1848.4−0141 (3FGL) W43 (EXTRA)
HESS J1849−000	G32.6+0.5 (PWN) J1849−0001 (PSR)
HESS J1852−000	3FGL J1853.2+0006 (3FGL) G32.8−0.1 (SNR) J1853+0011 (PSR) J1853−0004 (PSR) G33.2−0.6 (SNR)
HESS J1857+026	J1856+0245 (PSR) MAGIC J1857.2+0263 (EXTRA) MAGIC J1857.6+0297 (EXTRA) 2FHL J1856.8+0256 (2FHL)
HESS J1858+020	3FGL J1857.9+0210 (3FGL)
HESS J1908+063	ARGO J1907+0627 (EXTRA) MGRO J1908+06 (EXTRA) G40.5−0.5 (SNR) 3FGL J1907.9+0602 (3FGL) J1907+0602 (PSR)
HESS J1911+090	G43.3−0.2 (SNR) 2FHL J1911.0+0905 (2FHL) 3FGL J1910.9+0906 (3FGL)
HESS J1912+101	J1913+1011 (PSR)
HESS J1923+141	3FGL J1923.2+1408e (3FGL) 2FHL J1923.2+1408e (2FHL)
HESS J1930+188	G54.1+0.3 (COMP) J1930+1852 (PSR) VER J1930+188 (EXTRA)
HESS J1943+213	IGR J19443+2117 (EXTRA) 2FHL J1944.1+2117 (2FHL)